Towards Enhanced Rehabilitation: Modeling and Control of Lower Limb Exoskeletons for Human-Robot Cooperation and Fatigue Management

Von der Fakultät für Elektrotechnik und Informationstechnik der Rheinisch-Westfälischen Technischen Hochschule Aachen zur Erlangung des akademischen Grades eines Doktors der Ingenieurwissenschaften genehmigte Dissertation

vorgelegt von

Lukas Manuel Bergmann, M.Sc.
aus Mettingen, Deutschland

Berichter: Univ.-Prof. Dr.-Ing. Dr. med. Dr. h.c. Steffen Leonhardt
Univ.-Prof. Dr.-Ing. Dr. med. h.c. Robert Riener

Tag der mündlichen Prüfung: 31.10.2024

Acknowledgement

Die Inhalte dieser Dissertation sind während meiner Arbeit am Lehrstuhl für Medizinische Informationstechnik (MedIT) entstanden. Ein besonderer Dank gilt daher meinem Doktorvater Herrn Professor Steffen Leonhardt, der mir eine enge Verknüpfung der Projektarbeiten mit dem Dissertationsthema ermöglichte, viel Spielraum für eigene Ideen ließ und stets für inspirierende und wertvolle Diskussionen verfügbar war. Ein weiterer Dank gilt Herrn Professor Robert Riener, der mir einen lehrreichen Forschungsaufenthalt am Sensory-Motor Systems Lab an der ETH in Zürich ermöglichte und zusätzlich das Korreferat meiner Doktorarbeit übernommen hat.

Ein besonderer Dank gilt meinen beiden Arbeitsgruppenleitern Dr.-Ing. Chuong Ngo, der mich bereits seit dem Bachelor am MedIT begleitet und unterstützt hat, und Dr.-Ing. Philip von Platen, der mich ermutigt hat, die Dissertation am MedIT anzufangen und mich vor allem im letzten Jahr der Promotion unterstützt hat.

Des Weiteren bedanke ich mich bei den vielen Studentinnen und Studenten, die durch zahlreiche Bachelor-, Master-, Projekt- und Seminararbeiten einen wesentlichen Beitrag zum Vorankommen dieser Dissertation geleistet haben. Ein besonderer Dank gilt Viet Duc Phan, Oliver Lück, Philipp Buschermöhle und Lea Hansmann, die hervorragende Leistungen in ihren Abschlussarbeiten erbracht haben.

Die Zeit am MedIT habe ich vor allem wegen der Kollegen sehr wertgeschätzt und genossen. Ich möchte mich daher bei dem gesamten MedIT Team bedanken. Insbesondere möchte ich mich bei meinen Bürokollegen Carl-Friedrich Benner, Bernhard Penzlin und Dr. Markus Lüken und bei den Bewohnern der Schurzi bedanken, die immer für eine Partie am Kicker, für konstruktive und prokrastinierende Gespräche, für eine Telefonkonferenz auf der Dachterrasse oder einen geselligen Feierabend zu haben waren. Durch das MedIT-Team wird mir die Zeit meiner Promotion trotz aller Herausforderungen immer gut in Erinnerung bleiben.

Danke an Dr. Gleb Koginov, mit dem ich noch Monate nach meinem Aufenthalt in Zürich regelmäßige Videokonferenzen hatte, um unser gemeinsames Paper zu finalisieren. Die Zusammenarbeit war eine schöne Abwechslung zum Arbeitsalltag.

Zuletzt möchte ich meiner Familie danken, die mich stets unterstützt hat. Meine Mutter Gisela, meine Geschwister Felix und David und ihre Familien standen immer an meiner Seite. Ein besonderer Dank geht an meine Frau Sophie, die mich stets ermutigt hat, mir mit Rat und Tat zur Seite stand und mir ermöglichte, mich auf meine Dissertation zu konzentrieren, während unsere gemeinsame Tochter Cara mich immer wieder daran erinnerte, die kleinen

Freuden des Lebens zu schätzen und tatkräftig mit in die Tasten meines Laptops patschte.

Zum Gedenken an meinen Vater, Hubert. Auch wenn du den Abschluss dieser Arbeit nicht miterleben konntest, warst du es, der meine Leidenschaft für die Elektrotechnik entfacht hat. Dein Vertrauen und deine Unterstützung waren es, die mich bis hierher gebracht haben.

Zürich, January 6, 2025
Lukas Manuel Bergmann

Abstract

The marvel of human walking is a complex combination of intricate control strategies, but it can be disrupted by injuries and illnesses such as strokes. The prevalence of the resulting gait disorders remains an acute global health challenge affecting millions of people. Early and intensive rehabilitation is crucial for recovery. Traditional rehabilitation methods require significant financial and human resources, leading to an increased interest in rehabilitation robotics. In addition, aging demographics will increase the need for home-based care, fostering demand for rehabilitation robotics and ultimately promoting greater autonomy for individuals. For optimal rehabilitation outcomes, it is important that patients actively initiate movements themselves, as this kind of motor learning is crucial for stimulating neuroplasticity. Exoskeletons that prioritize patient-initiated actions and adapt in real-time to user intent could benefit clinical and everyday settings. The realization requires precise sensing of movement intention and utilizing advanced control strategies to support the patient's movement while prioritizing safety through hardware and software solutions.

This dissertation explores methods to design and control lower limb exoskeletons to enhance robot-assisted rehabilitation. The proposed approach designates the user as the central controller, underscoring the robot's role in responding to, rather than dictating, human movements. By estimating the user's joint torque in real-time through a coupled human-exoskeleton model for both swing and stance phases, a novel human-cooperative controller is developed to augment user movement. The control strategy has been validated on a newly designed exoskeleton with variable stiffness actuators for hip and knee actuation. Additionally, a control concept for the varying serial elasticity is proposed to combine the advantageous high bandwidth of a stiff actuator with the patient safety advantage of a compliant actuator in response to patient motion. Finally, this thesis examines the potential of exoskeletons as both a diagnostic and intervention tool for muscle fatigue – a prevalent and debilitating symptom among individuals with gait disorders. For this purpose, a fatigue model is formulated and parameterized based on a study involving healthy participants, and the feasibility of modulating the exoskeleton's assistance according to the fatigue level is investigated.

The results of this dissertation highlight novel methodologies that enhance the user-exoskeleton synergy by placing the user as the central controller of the system. The findings are expected to aid in the design and control of future exoskeletons to improve rehabilitation outcomes, reducing therapist workload and enabling home-based training and consequently improving the patient's overall quality of life.

Contents

Abbreviations and symbols

List of abbreviations

Abbrev.	Meaning
ADP	adenosine diphosphate
AP	action potential
ARE	algebraic riccati equation
ATP	adenosine triphosphate
bpm	beats per minutes
CAN	controller area network
cHMI	cognitive human-machine interface
CNS	central nervous system
DoF	degree-of-freedom
EE	energy expenditure
EEG	electroencephalography
EKF	extended Kalman filter
EMG	electromyography
FAC	functional ambulation categories
FES	functional electrical stimulation
FF	feed-forward
FG	fast glycolytic
FO	fast oxidative
FSR	force sensing resistor
FTS	force-torque sensor
GM	gluteus maximus
GRF	ground reaction force
HiL	human-in-the-loop
HR	heart rate
HS	hamstrings
IMU	inertial measurement unit
IP	iliopsoas
KF	Kalman filter
LPV	linear parameter varying
LQG	linear quadratic Gaussian
LQGI	LQG controller with integral behavior

Abbrev.	**Meaning**
LQR	linear quadratic regulator
L^2Exo-SE	lower limb exoskeleton with serial elastic actuators
MAE	mean absolute error
MeRIA	mechanical-rotary variable impedance actuator
MG	muscle group
MU	motor unit
MVC	maximum voluntary contraction
PEA	parallel elastic actuator
pHMI	physical human-machine interface
PNS	peripheral nervous system
QF	quadriceps femoris
RC	residual capacity
RMSE	root-mean-square error
RoM	range-of-motion
RPF	ratings of perceived fatigue
SCI	spinal cord injury
SD	standard deviation
SEA	serial elastic actuator
SO	slow oxidative
SoF	state of fatigue
SQP	sequential quadratic programming
SR	sarcoplasmic reticulum
SVF	state variable filter
Sit2Stand	sit-to-stand
TL	target load
TVA	torque-velocity-angle
UKF	unscented Kalman filter
VSA	variable stiffness actuator
3CC	three-compartment controller

List of Latin Symbols

The Latin and non-Latin symbols listed in the following two tables can be specified using the indices given in the table thereafter. The use of a symbol in combination with one or more indices is indicated by an asterisk $*$.

Symbol	Unit	Meaning
C		muscle activation-deactivation drive
$\mathbf{C}$	$\mathrm{N\,m\,s}$	Coriolis matrix
d_*	$\mathrm{N\,m\,s}$	damping constant
$\mathbf{D}$	$\mathrm{N\,m\,s}$	damping matrix
E_{kin}	J	kinetic energy
E_{pot}	J	potential energy
F	s^{-1}	rate of fatigue
F_*	N	force
$\mathbf{G}$	$\mathrm{N\,m}$	torque vector caused by gravity
g	$\mathrm{N\,m^2\,kg^{-2}}$	gravity constant
$\mathbf{H}$		Hessian
I_*	A	current
J_*	$\mathrm{kg\,m^2}$	motor and gear inertia
k_*		assistance factor
$\mathbf{K}$		Kalman gain
K_{emf}	$\mathrm{N\,m\,A^{-1}}$	back electromotive force constant
K_I		integral gain of controller
K_P		proportional gain of controller
l_*	m	length
$\mathcal{L}$	J	Lagrangian
L_D		development factor
L_R		relaxation factor
m_*	kg	mass
$\mathbf{M}$	$\mathrm{kg\,m^2}$	mass inertia matrix
M_A		active motor units
M_F		fatigued motor units
M_R		resting motor units
$\ddot{\mathbf{q}}$, $\dot{\mathbf{q}}$, $\mathbf{q}$		motion variables, e.g. angular acceleration, angular velocity, and angle

Symbol	Unit	Meaning
r		rest recovery factor
R_*	s^{-1}	rate of recovery
RC_*	%MVC	residual capacity
SoF_*	%	state of fatigue
TL_*	%MVC	target load
x_*	m	center of mass in x direction
y_*	m	center of mass in y direction

List of Non-Latin Symbols

Symbol	Unit	Meaning
α		duty cycle of active phase
β		duty cycle of resting phase
γ_*	-	gear transmission
σ_*	$\mathrm{N\,m\,rad}^{-1}$	actuator stiffness
$\bar{\sigma}_*$	$\mathrm{N\,m\,rad}^{-1}$	max. actuator stiffness
$\underline{\sigma}_*$	$\mathrm{N\,m\,rad}^{-1}$	min. actuator stiffness
$\mathbf{\Sigma}$		covariance
τ_*	N m	joint torque
φ_*	rad	joint angle
$\dot{\varphi}_*$	$\mathrm{rad\,s}^{-1}$	joint's angular velocity
$\ddot{\varphi}_*$	$\mathrm{rad\,s}^{-2}$	joint's angular acceleration
ω	$\mathrm{rad\,s}^{-1}$	circular frequency variable

List of Indices

Index	Referring to
a	active
blend	blending between two phases
exo	exoskeleton
F	foot
FF	feed-forward
GM	gluteus maximus
GRF	ground reaction forces
H	hip
HS	hamstrings
IP	iliopsoas
K	knee
MG	muscle group
M1	motor 1, main drive
M2	motor 2, secondary motor
p	passive
pat	patient/human
QF	quadriceps femoris
ref	reference
rr	rest recovery
S	shank
St	stance phase
Sw	swing phase
T	thigh
th	threshold
To	torso

1 Introduction

The process of walking, which many of us take for granted, is a marvel of natural control mechanisms. From infancy, we autonomously master intricate control strategies, effortlessly coordinating every muscle and joint in harmonious sequences that carry us through life. This subconscious process of human gait is a reflection of our body's resilience and adaptability. But, this sensitive balance can suddenly be disrupted by events such as strokes or injuries. The prevalence of gait disorders or disabilities of the lower extremities remains an acute global health challenge. Annually, approximately 13.7 million people experience a stroke, and there are around 80.1 million existing cases of stroke worldwide, based on 2016 data [JNR+19]. Specifically, over 80% of stroke survivors exhibit gait dysfunction [DZB+05]. In addition, patients with post-polio, multiple sclerosis, and *spinal cord injury* (SCI) suffer from impaired motor function [YF17]. For the affected people, limited mobility harms physical and mental well-being and can reduce physical and psychological strength [IW14].

Comprehensive rehabilitation is essential for the optimal recovery of the affected person. Notably, the most pronounced benefits, such as improved walking independence and speed, are observed when interventions commence promptly after a stroke [MP12]. Traditional rehabilitation methods often demand significant financial and human resources. Device-assisted therapies, such as those employing end-effector devices – guiding a patient's feet – or lower limb exoskeletons, present a promising alternative, alleviating the physical strain on therapists [Reh20].

Exoskeletons, derived from the Greek words exo ('outside') and skeletós ('dried-up body'), are wearable devices designed to enhance human joint movement, augmenting the user's strength and endurance for various tasks. They can be classified according to their mechanical structure, their support, and their application. In the private sector, for example, exoskeletons promise increased independence and a better quality of life for the elderly. In the medical sector, exoskeletons offer a promising approach for rehabilitation after a SCI or paralysis due to a stroke, by restoring limited movement function [MKQ+07, ZWZ+12, ETPS12, HSJ+20].

One of the first active exoskeletons was developed between 1965 and 1971 by the U.S. company General Electrics [Mos67]. The Hardiman provided the first significant impetus for motion tracking and thus cooperative operator support. However, the system was heavy, expensive, error-prone, and therefore unsuitable for therapeutic purposes. In recent decades, active lower limb exoskeletons have become an increasingly important tool in gait rehabilitation due to advanced processing units, power management systems, actuation concepts, and control strategies. However, patient-cooperative interaction, human-robot coupling, and

patient-centered support concepts remain major challenges in the development of these systems. Therefore, this dissertation addresses three facets that are barely addressed in existing exoskeleton designs.

The first aspect was underlined in a review by Mehrholz et al. in 2012 which states that post-stroke patients demonstrate improved walking speeds after undergoing end-effector gait training. In contrast, no such improvement was observed when these patients were directed by an exoskeletal device [MP12]. Bingham's 1988 proposition provides a potential explanation, suggesting that active motor learning, where patients initiate movements themselves, is essential for stimulating neuroplasticity [Bin88]. This highlights the significance of developing exoskeletons that are not only safe and reliable but also prioritize the enhancement of patient-initiated movements. Unlike end-effector devices that are primarily therapeutic, these patient-cooperative exoskeletons could be beneficial both in clinical settings and everyday life. Facilitating home-based training can maximize functional performance and increase safety, thereby enhancing the overall life quality and mobility of patients while reducing caregiver's responsibilities [GLG93]. Patient cooperation relies on the ability to accurately sense the intent behind a patient's movement. To be widely adopted in daily activities, motion detection and assistance must be simple, immediate, seamless, and error-free. While effective in ideal settings, *electromyography* (EMG) based methods require laborious electrode placement and carry risks associated with inconsistent conductivity [HK07, KH12]. In contrast, model-based techniques for online prediction of movement intention are unaffected by these limitations. However, so far, their use has mostly been limited to isolated movements such as the swing motion or *sit-to-stand* (Sit2Stand) task [LLNM20, LHP+20] or to the upper body [LHA+17, ZKF+20], thus missing continuous changes in the environment, such as during the swing and stance phases of walking.

The second fundamental aspect in the design of an exoskeleton is intrinsic safety, which can be achieved through compliant elements in the actuation [XQ13, SVGVT+19]. Typically, exoskeletons are designed with rigid elements connected through joints. However, when looking at nature's blueprint, it tends to use softer, more adaptable materials that can still function effectively under the most challenging conditions. For example, although bones are hard structures, they are surrounded by flexible tissues such as muscles and tendons. While such rigid components provide increased precision and superior load bearing and force transmission, compliant or elastic structures allow passive adaptation to the environment, protecting the system from mechanical damage and, more importantly, the user from injury. For this reason, the use of compliant elements such as *serial elastic actuators* (SEAs), *variable stiffness actuators* (VSAs) or artificial muscles in exoskeletons is steadily increasing [WWM+14, JBG+14, GRGG+17, SVGVT+19, ZWCZ22]. However, existing

solutions have neglected the potential that lies in adapting elasticity properties to the motion and environment.

The third aspect to consider when using exoskeletons in rehabilitation or everyday life is the extent to which the exoskeleton should support the user. Typically, the therapist or user needs to manually set the assistance factor based on the patient's mobility and perceived fatigue. Fatigue is a common experience in our daily activities, but a debilitating symptom for individuals with hemiparesis who have compromised muscle function. Research shows that up to 72% of stroke survivors experience fatigue, and 46% consider it their most impairing symptom [KRG12]. In addition, patients with incomplete SCI experience increased muscle fatigue during prolonged walking [DNG+20]. This finding suggests that fatigue management should be considered in their rehabilitation process. Recognizing fatigue in daily life and during rehabilitation can minimize the risk of falls, as fatigue can affect gait parameters and increase the likelihood of falls [PL08, DNG+20]. However, fatigue management in purely mechanical (non-*functional electrical stimulation* (FES)) assistive exoskeletons has never been considered in the literature.

Aim of the Thesis

The primary goal of this thesis is to provide new methods for designing and controlling lower limb exoskeletons to advance robotic-assisted rehabilitation therapy in the future. This work emphasizes an approach where the user is not only the recipient of robotic assistance but rather the central controller of the exoskeleton. For this reason, the thesis focuses on the development, modeling, and control of lower limb exoskeletons to improve human-robot interaction. This is further clarified by exploring the following research questions:

1. What are the necessary actuator specifications for an exoskeleton to accommodate dynamic adjustments of serial elasticity throughout various phases of a gait cycle?

2. How viable is the real-time estimation of the torque produced by the user in exoskeletons equipped with variable serial elasticities?

3. To what extent can the torque estimation strategy be utilized to formulate individualized assistance control in exoskeletons?

4. How effective is the modulation of serial stiffness in an exoskeleton for enhancing user safety?

5. Can muscle fatigue be diagnosed and quantified during the use of exoskeletons?

6. Is it feasible to manage the user's muscle fatigue levels by adjusting the level of exoskeleton support?

Structure of the Thesis

This thesis is organized into six chapters, where chapters 3, 4, and 5 address the main research contributions of this work. In detail, the remaining five chapters are structured as follows:

Chapter 2: This chapter provides an introduction to the physiological and technical background relevant to this book. The physiology and biomechanics section includes a brief introduction to the anatomy of the lower extremities, the physiology and mechanics behind motion and gait, simulations of both forward and inverse dynamics, an introduction to gait disorders, and fatigue – a debilitating symptom among patients with gait disorders. Then, a brief overview of current concepts in lower limb rehabilitation robotics, focusing on sensors, actuators, and control methodologies is presented. The chapter concludes with the basic principles of systems theory by covering system identification, parameter estimation, and state estimation.

Chapter 3: The design of a new lower limb exoskeleton featuring VSAs for hip and knee assistance is presented in this chapter. Furthermore, a detailed model and parameter identification process of the coupled exoskeleton-patient system is derived. Lastly, a non-linear human joint torque estimation based on an *unscented Kalman filter* (UKF) and a static model are presented for the swing phase and stance phase, respectively.

Chapter 4: The design of a human-cooperative control strategy relying on the previously derived human torque estimation is presented. The control strategy assists the subject during all phases of the gait based on their intention to move. Additionally, an automated stiffness selection for the VSAs dependent on the human's movement and the environment is presented. Furthermore, possible safety mechanisms for lower limb exoskeletons are explored. Finally, the developed control strategy is validated and discussed.

Chapter 5: The chapter starts with the design of a model to describe human muscle fatigue during exoskeleton walking. The model is parameterized by conducting a study on healthy subjects. Subsequently, a controller that automatically sets the exoskeleton's assistance to manage muscle fatigue is described. Finally, the results of the parameter identification study and controller validation are shown and discussed.

Chapter 6: This chapter concludes the dissertation by summarizing the most important findings with respect to the formulated research questions and outlining further research opportunities.

2 Background

The interdisciplinary nature of this work requires certain background knowledge of the physiological aspects of human motion generation and gait, the state of the art in rehabilitation therapy, and some technical fundamentals. This chapter begins with an introduction to biomechanics and gait physiology. This includes a brief introduction to the anatomy of the lower extremities, the mechanics behind motion and gait, simulations of both forward and backward dynamics, and gait disorders, with a special emphasis on fatigue. Following this, a brief overview of current concepts in lower extremity rehabilitation robotics, focusing on sensors, actuators, and control methodologies is given. The chapter concludes with the principles of systems theory by covering system identification, parameter estimation, and state estimation.

2.1 Biomechanics and Human Locomotion

Biomechanics is the interdisciplinary study of the mechanical principles underlying the structure and movement of living organisms. It integrates principles from physics and engineering to analyze how biological systems respond to external forces and how they generate internal forces themselves. The fundamentals of biomechanics are essential for understanding and developing the interaction between humans and robots. For this reason, the basics of biomechanics with regard to human locomotion are explained in the following chapter.

2.1.1 Anatomy of the Lower Limbs

The musculoskeletal system is essential to provide stability for the upright stand and allow gait movements. It consists of the skeletal system, which includes the bones, joints, and supporting structures, as well as the muscular system consisting of the muscles and tendons.

Joints

The human skeleton has over 200 bones, supported by cartilage, ligaments, tendons, and muscles. Bones can be grouped into two types: axial bones in the body's center, and appendicular bones in the limbs and hips. The connection between bones are joints. Joints allow various movements and can be sorted into three types: fibrous, cartilaginous, and synovial. Synovial joints are the most common and provide free movement due to the connecting joint cavity. They can be classified into uniaxial, biaxial, and multiaxial joints depending on their ability to move in one, two, or multiple directions [NGY21].

Body movements are often described in relation to the neutral anatomical position: standing upright with arms by the sides and palms facing forward. To categorize movements, three primary planes can be defined. The sagittal plane divides the body into left and right halves, the coronal plane into front and back, and the transverse plane into top and bottom. Key movements of the knee and hip include flexion, extension, abduction, and adduction as visualized in Fig. 2.1. The first two describe movements in the sagittal plane, where flexion reduces the angle between two bones, while extension increases it. The hip joint can also perform abduction and adduction which are movements in the coronal plane. Additional movements encompass external and internal rotations, tilting, and complex motions involving several joints [DBJ+13].

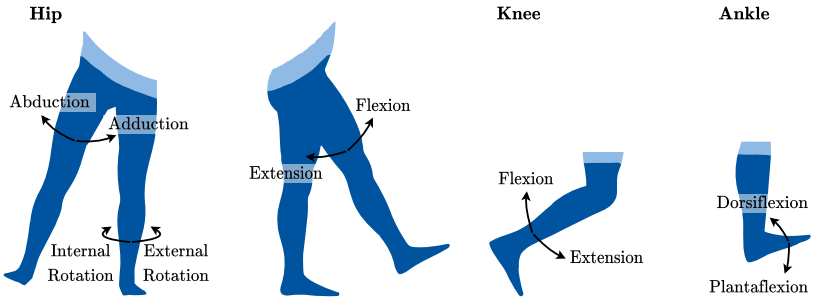

Figure 2.1: Main movements of the hip, knee, and ankle joint.

The hip joint, a synovial joint, links the top of the femur to the hip bone. Functioning as a multiaxial ball-and-socket joint, it permits movements like flexion, extension, abduction, adduction, and both external and internal rotation (see Fig. 2.1). Essential for bearing the body's weight, the hip joint plays a crucial role in stabilizing the human body when standing and walking [DBJ+13].

The knee joint is the body's largest joint and links the bottom of the femur, the top of the tibia, and the patella. Classified as a synovial joint, it functions primarily as a hinge joint enabling flexion and extension through a combination of rolling and gliding movements between the femur and tibia. Additionally, the knee can undergo minor rotations under specific conditions [DBJ+13].

Muscular System

The muscular system in humans encompasses three primary muscle types: the cardiac, smooth, and skeletal muscles. Voluntary control is possible with skeletal muscles, driven by the somatic division of the nervous system. However, reflexes might cause them to contract involuntarily. On the other hand, the autonomic nervous system regulates both cardiac and smooth muscles, making their actions involuntary. The fundamental roles of muscles include generating force, maintaining posture, stabilizing joints, and producing heat [MHH13, NGY21].

Muscles associated with the hip are categorized into specific groups as visualized in Fig. 2.2. The primary hip flexor is the *iliopsoas* (IP), formed by the psoas major and iliacus muscles. The *gluteus maximus* (GM), vital for activities like stair-climbing and stabilizing the trunk during walking, serves as the primary hip extensor. Along with the gluteus medius and gluteus minimus, responsible for abduction, they constitute the gluteus group [DBJ+13].

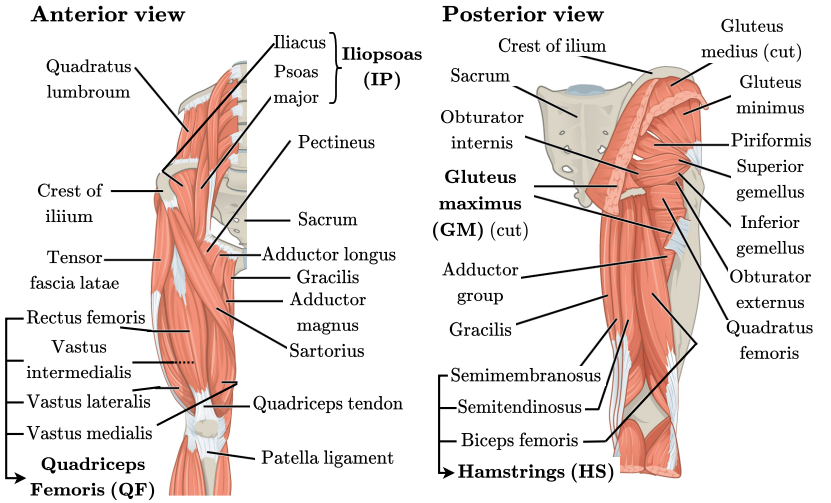

Figure 2.2: Important muscles of the thigh and the hip. Modified from [DBJ+13].

Thigh muscles are segregated into extensors, adductors, and flexors. The *quadriceps femoris* (QF), encompassing the rectus femoris, vastus medialis, vastus intermedius, and vastus lateralis, predominantly facilitates knee extension.

The adductor group, which includes the adductor longus, adductor brevis, and adductor magnus, aids in thigh rotation. Knee flexion is primarily controlled by the *hamstrings* (HS), composed of the biceps femoris, semitendinosus, and semimembranosus. It is noteworthy that since the quadriceps femoris and hamstrings span both the hip and knee joints, their effects are interconnected. For instance, the quadriceps femoris can function as a hip flexor to a degree, while the hamstrings can act as hip extensors.

2.1.2 Physiology of Movement Generation

The intention to move has its origin in the *central nervous system* (CNS). The CNS is composed of the brain and the spinal cord, whereas the *peripheral nervous system* (PNS) consists of the nerves connecting different body parts with the CNS. The primary motor cortex is located in the frontal lobe of the brain and initiates the command for the intended movement. Motor neurons transmit electrical impulses from the motor cortex along the spinal cord and the peripheral nerves to the muscle. The connection of a motor neuron and all innervated muscle fibers is called a motor unit [DBJ+13].

Force Generation

Muscle force is generated by contracting muscle fibers. The contraction results from the interaction between actin and myosin proteins within the muscle fiber's sarcomere. This interaction is initiated by an electrical impulse, an *action potential* (AP), which leads to a chain of events: neuron depolarization due to ion transfer of K^+ and Na^+, Ca^{2+} release through channels in the *sarcoplasmic reticulum* (SR), and the formation of cross-bridges between proteins. Subsequently, a power stroke occurs while the myosin head pulls the actin towards the center of the sarcomere. During that process, *adenosine diphosphate* (ADP) and inorganic phosphate are released. The detachment of the myosin head occurs while the *adenosine triphosphate* (ATP) bonds to the myosin. By hydrolyzing ATP to ADP, the myosin head transforms to its initial position allowing a new cross-bridge-cycle [MHH13].

The process of cross-bridge-cycling evokes muscle contraction resulting in a force, also called muscle tension. Muscle contraction can be isometric (tension without changing length) or isotonic (constant tension with changing length). In isotonic contractions, the muscle can either shorten (concentric) or lengthen (eccentric[1]), producing positive or negative power, respectively [Win09, MHH13].

[1] In eccentric movements, the muscle lengthens passively due to a counteracting force, as observed when lowering a weight.

Motor Unit (MU)

The motor unit (MU) represents the muscle's most basic controllable component. It's comprised of a motor neuron, its interconnected muscle fibers, and their neuromuscular junctions - where the neuron's axon terminals meet the muscle fibers.

Each muscle consists of a finite number of MUs ranging from a few to several hundred. The size of MUs depends on the task the muscle controls. For intricate tasks, like finger or eye movements, smaller MUs are utilized. Whereas, muscles responsible for bearing weight, such as those in the hip, are made up of larger MUs. The process of MU recruitment adheres to the size principle. MUs with thinner muscle fibers, which have a lower activation threshold, are called upon first when less force is demanded. These smaller, slow-twitch MUs are labeled as type I MUs. They offer low force output and slower contraction rates but they are highly resistant to fatigue. Additionally, they produce ATP aerobically, leading to the term *slow oxidative* (SO) muscle fibers. Due to their attributes, Type I MUs are engaged during prolonged activities and posture maintenance. On the other end, there are fast-twitch MUs, or type II MUs. This type of MUs is less readily activated but delivers more substantial forces and quicker contractions. Type II MUs are further categorized by their ATP production methods into *fast oxidative* (FO) and *fast glycolytic* (FG) fibers. fast oxidative fibers produce ATP in an oxygen-rich environment and resist fatigue to a moderate extent. In contrast, fast glycolytic fibers rely on anaerobic glycolysis for ATP and tire quickly. High-intensity, short-duration activities call upon fast glycolytic MUs, while tasks of medium intensity, like walking or sprinting, utilize fast oxidative units [MHH13].

In essence, a muscle's force output is the collective force produced by all its activated MUs. For peak force production, all MUs are engaged at once. But for less force, MUs tend to activate in a staggered manner, allowing periods of rest for some, which in turn postpones the onset of muscle fatigue [Win09, MHH13].

Movement Generation

Skeletal muscles are connected to the bone by tendons allowing muscles to exert force in a lever system where bones act as rigid levers. The joint torque results from combining the moments of all muscles spanning the joint with those from passive structures. The primary muscle driving a movement is termed the agonist or prime mover, while its opposing muscle is the antagonist. Movements arise from the interplay of these muscles. A simultaneous contraction of both muscles is called co-contraction and occurs during the stabilization of a joint. More importantly, it is the main cause of inefficient movement generation in

specific pathologies, such as hemiplegia. For certain movement patterns, the collaboration of multiple joints, called motor synergy, is needed. One example is the generation of the human gait. In this case, the support moment, which is the integrated activity of the lower limb muscles, overcomes gravity and moves the human body forward [Win09].

2.1.3 Human Gait

Human gait refers to the coordinated movement of the body while maintaining balance, achieved through repetitive motions of the lower limbs. This movement can be described as a stretch-shortening cycle, given the muscles' continuous cycle of expansion and contraction [BMA15]. Achieving this intricate motion requires synergy among the skeletal, muscular, and neurological systems [BMA15]. A single gait cycle is marked by two repeated events, typically starting with the moment the foot makes initial contact with the ground as visualized in Fig. 2.3.

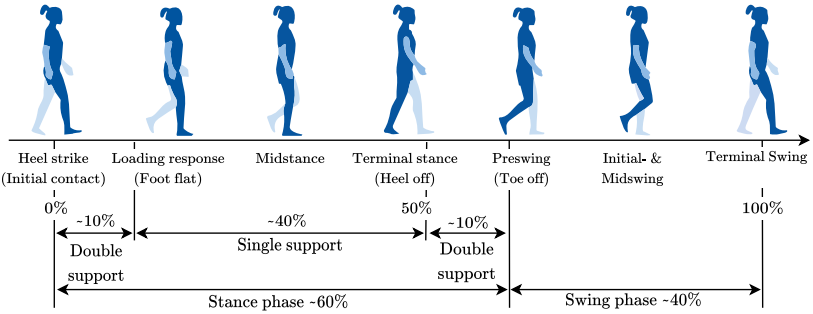

Figure 2.3: The human gait cycle. Modified from [UD21].

The gait cycle is segmented into the stance and the swing phases. The stance phase accounts for 60% of the cycle, signifying the duration the foot remains grounded. Conversely, the swing phase represents the remaining 40% when the foot is elevated. The gait phases can be categorized as single or double support, depending on whether one foot or both feet are on the ground. For a more detailed understanding, the gait cycle can be further categorized into subphases. During the stance phase, these include initial contact, loading response, mid-stance, terminal stance, and pre-swing; the swing phase is divided into the initial, mid, and terminal swing.

The joint angles of the lower body throughout this cycle, depicted for three distinct gait velocities, can be seen in Fig. 2.4.

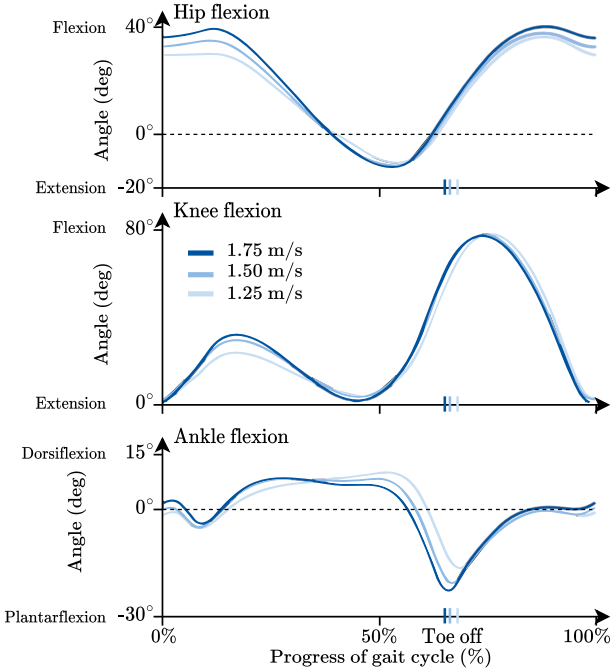

Figure 2.4: Joint angles during one gait cycle. Data from [AHS+13], Fig. redrawn from [UD21].

2.1.4 Dynamics

When evaluating human gait, both kinematics and kinetics are crucial. Kinematics deals with body movements without accounting for the forces involved, encompassing the position, velocity, and acceleration of body parts and joints. On the other hand, kinetics examines the forces and torques that drive these motions. Computer simulations facilitate the estimation of unmeasurable parameters and enable predicting movements in theoretical situations.

Forward Dynamic Simulation

The forward dynamic simulation depicted in Fig. 2.5 operates on the premise of neural activation in one or multiple muscle groups, mirroring real movement generation. Leveraging a musculoskeletal model, this simulation can forecast muscle forces, joint torques, and the resulting movement. Experimental data aids in validating the foundational mathematical models [UD21].

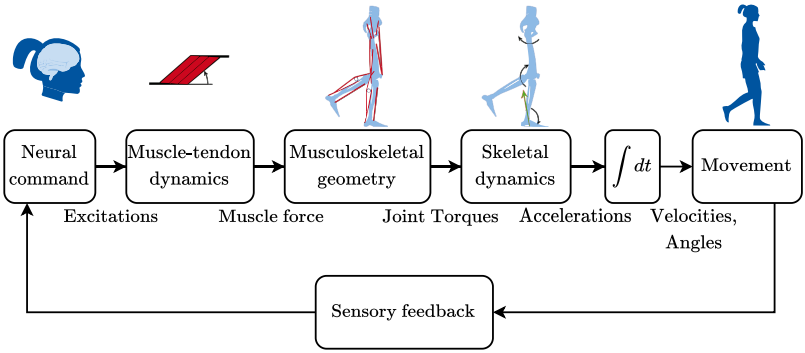

Figure 2.5: Concept of forward dynamic simulation. Fig. redrawn from [UD21].

Inverse Dynamic Simulation

Inverse dynamic simulation, on the other hand, utilizes body motion measurements to determine joint torques or even muscle forces as visualized in Fig. 2.6. The motion of the body segments can be captured by motion-capturing systems, for example. Through inverse kinematics, joint movements can be derived, followed by their corresponding angular velocities and accelerations. The joint torques result from the sum of the external forces, e.g. the *ground reaction forces* (GRFs) and gravitational forces, as well as internal forces produced by muscle tension. The GRFs act during the stance phase opposite to the body weight and must be measured to perform the inverse dynamic procedure. Typical GRFs throughout a gait cycle are depicted in the appendix in Fig. A.1.

The estimated joint torques correspond to the muscular tension, composed of the contraction force and the passive tension of the ligaments. Typical joint torques during gait estimated by inverse dynamics are visualized in Fig. 2.7. The muscle force leading to the observed motion can be assessed either by measuring the muscular activation using electromyography or by solving an optimization problem based on the calculated joint torques [Win09].

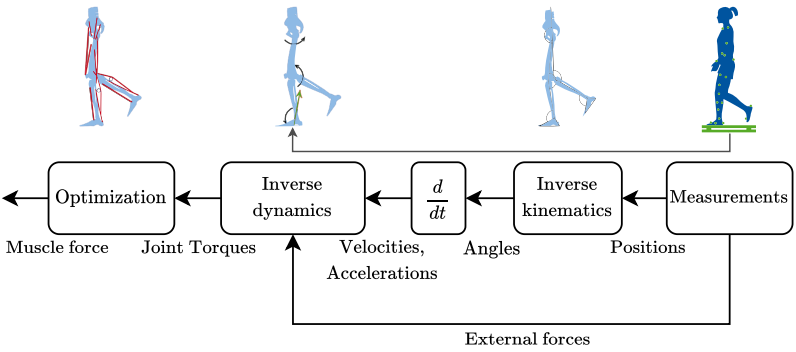

Figure 2.6: Concept of inverse dynamic calculation. Fig. redrawn from [UD21].

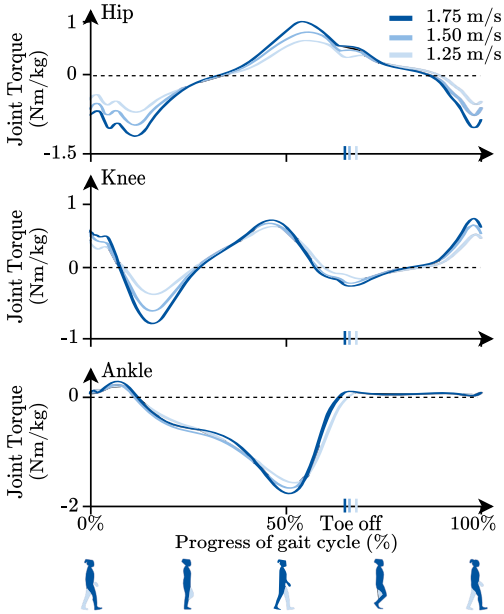

Figure 2.7: Joint torques during one gait cycle. Fig. redrawn from [UD21].

2.1.5 Gait Disorders

Gait disorders refer to any deviations from the standard walking pattern. Various factors can contribute to these irregularities, ranging from neurological conditions and musculoskeletal problems to age-related changes and physical injuries. Each cause can lead to distinctive changes in gait.

For the purpose of this thesis, a particular emphasis is placed on gait disorders resulting from neurological issues, especially those occurring post-stroke. This focus is motivated by the statistic that every year, approximately 13.7 million strokes occur worldwide [JNR+19]. The most frequent side effect of brain damage, such as a stroke, is paralysis and paresis (incomplete paralysis) [Nel08]. Specifically, post-stroke leg paresis is prevalent, affecting 72.4% of stroke survivors [LCD+01].

Such post-stroke paresis often manifests as a hemiplegic gait. Here, one side of the body is weakened or entirely paralyzed, resulting in noticeable limb dragging or circumduction. While strokes are a major contributor to these gait abnormalities, other conditions like post-polio syndrome, multiple sclerosis, and *spinal cord injury* (SCI) can also result in compromised walking abilities and even paralysis.

Over time, paresis can lead to disuse or incorrect usage of the affected limb. This neglect can induce structural changes in the muscles and joints. More critically, it may also lead to chronic changes within the CNS. These structural alterations can, in turn, exacerbate the paresis, forming a detrimental feedback loop. The use and targeted training of the compromised limb is of high importance to break this vicious circle. To address these challenges and offer potential solutions, both classical and device-assisted rehabilitation therapies will be further explored in Sec. 2.2.1.

The *functional ambulation categories* (FAC) allows classification of the severity of the gait disorder [Mar14]. The scale divides the ability to walk into 6 levels:

0. Patient is unable to walk or requires the assistance of two or more therapists.

1. The patient is dependent on the permanent assistance of a person who helps to carry the weight and to maintain the balance.

2. The patient is dependent on continuous or intermittent assistance from a person to ensure balance and coordination.

3. The patient is dependent on verbal support or accompaniment of a person but not on physical help.

4. The patient walks independently on flat ground and only requires assistance, for example, when climbing stairs or on difficult surfaces.

5. The patient is able to walk independently in all respects.

2.1.6 Fatigue

Fatigue is a common symptom associated not only with post-stroke patients but also with disorders like autoimmune conditions including multiple sclerosis, cancer, and infectious disorders [Kru03]. Fatigue is commonly experienced as a feeling of exhaustion, tiredness, and lack of energy. It leads to the reduction of physical and physiological performance and is associated with many clinical health issues. During daily activities, fatigue can lead to increased response times, reduced awareness, diminished coordination, and a lack of attention [Bab19]. If fatigue is not resolved, it can lead to severe health disorders like *chronic fatigue syndrome*, which is characterized by cognitive impairment and physical exhaustion resulting in the inability to perform daily tasks. Fatigue can be classified as mental and physical fatigue. Mental fatigue is related to cognitive and perceptual aspects and can be characterized as reduced cognitive performance. Physical fatigue manifests as a decline in the performance of the motor system.

Although Enoka et al. [ED16] suggested not to classify fatigue into muscle fatigue and physical fatigue, many research groups continue to use this term to describe the impairment of physical activity or force generation [Vøl97, ED08, CMTO09].

Definition of Muscle Fatigue

Muscle fatigue can be defined as "any exercise-induced reduction in maximal capacity to generate force or power output" [Vøl97]. It is often described as the decline of *maximum voluntary contraction* (MVC), which is a measure of the force generated by an individual believing to perform with maximal effort. The reduction of strength depends on the type of contraction. Sustained maximal contraction evokes an immediate onset of fatigue and a strict decline in force output. In contrast, during repeated sub-maximal contractions, force can be maintained for a longer time until the target force cannot be generated anymore. This inability to generate the force output required to perform a specific task is called exhaustion. Several mathematical fatigue models have been developed to describe the strength reduction caused by muscle fatigue [Vøl97].

Physiological Mechanism of Fatigue

Fatigue, as classified by Enoka et al., comprises performance and perceived fatigability, influenced by factors like homeostasis, psychological state, muscle function, and activation [ED16]. Modulating physiological factors, like blood glucose, arousal, calcium kinetics, and voluntary activation contribute to fatigue but also interact with each other. Central fatigue is caused by factors within the CNS, affecting signal generation and transmission in the motor cortex [Vøl97]. Peripheral fatigue relates to factors at or distal to the neuromuscular junction [WQW+17].

Muscle fatigue is caused by several ionic imbalances [MHH13]. During the process of force generation (see Sec. 2.1.2), an imbalance of Na^+ and K^+ disturbs the membrane potential and causes an impaired Ca^{2+} release [MHH13]. Moreover, an increased amount of Mg^{2+} due to a lack of ATP also inhibits Ca^{2+} release [WQW+17]. A reduced number of calcium ions results in less cross-bridge cycling and consequently a lower force generation.

Muscle contraction needs ATP as a source of energy. The supply may be maintained through anaerobic and aerobic metabolic pathways, depending on the intensity of the task. During prolonged low-intensity tasks, ATP is generated through aerobic respiration. Aerobic metabolism takes place in the presence of oxygen, which is delivered via blood flow to the muscle. During contraction, the arterial blood pressure increases, leading to a reduced net blood flow to the muscle. Lower blood flow results in decreased removal of metabolic by-products and inhibited O_2 delivery to the working muscle [WQW+17]. Additionally, fatigue during endurance tasks can develop due to damage of the sarcoplasmic reticulum interfering with Ca^{2+} release [MHH13]. Aerobic generation is slow and produces a large amount of ATP. Thus, healthy trained individuals are able to maintain prolonged low-intensity tasks for many hours [MHH13]. Under these conditions, fatigue develops slowly but recovery requires several hours.

During high-intensity work, ATP supply is maintained through anaerobic metabolism, which is limited by the amount of glycogen. The glycogen content is closely related to exercise endurance [WQW+17]. Moreover, anaerobic metabolic by-products like lactate and inorganic phosphate contribute to changes in cross-bridge activity and thus a decrease of force output [WQW+17]. Especially the accumulation of lactate acids contributes to muscle aches and seems to be important in provoking central fatigue [MHH13]. Intense exercises of short duration provoke fatigue rapidly, which is followed by a rapid recovery. The variations of fatigue development during high-intensity tasks and endurance tasks underline the task-dependency of fatigue.

2.2 Rehabilitation Robotics - Lower Limb Exoskeletons

Rehabilitation therapy is crucial for individuals with impaired muscle activation, as it aids in restoring movement and daily functionality. Without timely physiotherapy, these impairments can worsen, leading to increased disability. Through consistent sessions, physiotherapy not only improves mobility but also prevents further deterioration.

2.2.1 Rehabilitation Therapy

When the gait apparatus is compromised, for instance following a stroke, rehabilitation treatment becomes essential to restore walking ability. Achieving the ability to walk independently (FAC rating 4 or 5, see Sec. 2.1.5) can be measured and improved through therapy [HSMW13]. This includes enhancing gait distance, speed, leg strength, functional mobility, velocity, and balance. Neuroplasticity and motor learning facilitate the enhancement of these gait characteristics [Bin88]. Central to this recovery is the repetition of walking movements, which can be facilitated through physiotherapy or specialized equipment.

Classical Therapy Approaches

Traditional gait training involves working closely with one or more physiotherapists, incorporating a range of strengthening exercises and gymnastics. This is followed by hands-on gait training, where physiotherapists use orthoses for passive support and stabilization. During the late 90s, treadmill training, supplemented with partial body weight support, remained the benchmark technique, exhibiting notable success in improving gait for chronically immobilized individuals post-stroke or SCI [Reh20]. Despite its effectiveness, this traditional approach demands multiple sessions weekly and places significant physical strain on the therapist, requiring extensive time and effort.

End-effector Assisted Therapy

Device-based training, using the end-effector principle, offers a solution to alleviate some of these demands. End-effector devices, as shown in Fig. 2.8a, come with adjustable foot plates where the patient's feet are secured. These plates follow a natural path, mimicking the stance and swing phases of walking. The gait trainer GT1 and GT2 (Reha-Stim, Schlieren, Switzerland) are two examples of such end-effector-based systems [HUO00, Reh20]. Additionally, these systems reduce cardiac and metabolic requests by supporting a portion of their body weight with a belt system and thus increase walking time duration

(a) Gait trainer GT1 [DMS17].

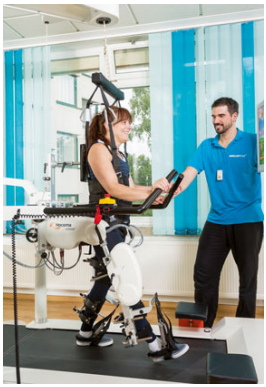

(b) Lokomat [Rie16].

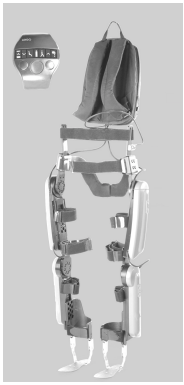

(c) ReWalk [TEB13].

Figure 2.8: Robotic rehabilitation devices.

during rehabilitation therapy of hemiplegic patients [MP12]. The body weight support also enables the utilization of end-effector devices for patients as early as FAC 0, for example, in the early rehabilitation phase after a stroke. The support continues to be beneficial until the patient can walk with assistance such as mild traumatic brain injury patients [Reh20].

While both conventional and device-assisted methods have proven effective, device-based therapies offer advantages in efficiency and reduced demands on personnel. Additionally, end-effector devices can increase the steps per training session by up to ten times [SWB+07]. Consequently, contemporary guidelines often favor device-assisted therapy over traditional methods [Nel08].

Exoskeleton Therapy Method

Exoskeletons are wearable devices designed to enhance human joint movement, augmenting the user's strength and endurance for various tasks. They can be classified according to their mechanical structure, their support, and their application. While rigid exoskeletons use stiff materials like metals or plastics, soft exoskeletons typically employ textiles and flexible components [TA20, XAG+21]. Both mechanical structures have advantages, including the increased comfort and lighter weight of soft exoskeletons and a higher actuation level of rigid exoskeletons. Additionally, exoskeletons can be classified as active, with powered mechanisms, or passive, offering only stability through their structural design. The application area of exoskeletons includes military, industrial, civilian,

and clinical purposes. For military and industrial purposes, exoskeletons assist healthy people during demanding tasks such as carrying heavy objects or performing specialized motions. The augmentation of strength and endurance time leads to reduced burden and minimized risk of musculoskeletal disorders. Using exoskeletons for civilians, particularly the elderly, exoskeletons promise enhanced independence and a better quality of life, easing pressures on care and healthcare systems. In the medical field, they play a pivotal role in rehabilitating patients with spinal cord injury (SCI) or post-stroke conditions, assisting those with compromised muscle functions [BSA+17].

One of the first exoskeletons for rehabilitation therapy was the Lokomat (Hocoma, Zurich, Switzerland) which is shown in Fig. 2.8b. Similar to end-effector-based therapy, the patient exercises on a treadmill while being held by a belt system. In addition, the patient experiences motorized support of the hip and knee joints. The support is provided utilizing gait trajectories, and an impedance controller [JCK+03]. The general effectiveness of this exoskeleton training could already be proven in 2007 by a study with 16 stroke patients [MKQ+07]. However, in a later study from 2019, worse effectiveness was achieved in comparison with conventional treadmill training [HNP+09]. The authors considered the cause to be the greater variety of the movement sequence in treadmill training.

Another popular exoskeleton design is the ReWalk (see Fig. 2.8c) [ETPS12]. It is used both in rehabilitation and as a gait aid for patients with FAC 0 and FAC 1 or paraplegia. The ReWalk is a bilateral exoskeleton and consists of motorized hip and knee joint support and passive support for the ankle joint. The real-time computer and battery for power are stored in a backpack. Crutches are part of the system as an additional gait aid and for balancing the body. The exoskeleton is controlled by selected gait trajectories depending on the current operating mode. The available movement patterns are: Walking, standing up, sitting down, and climbing stairs [ZWZ+12]. The first two subject studies with the ReWalk were published in 2012. The ReWalk was used by 6 and 12 patients who suffered from a SCI. The aim of each of the studies was to investigate the safety and usability of the exoskeleton which could be confirmed [ZWZ+12, ETPS12]. In a more recent study from 2020, the effectiveness of the exoskeleton was investigated in comparison with a gait aid and passive orthosis [HSJ+20]. The oxygen consumption of the test subjects was measured as a criterion for the effect of the support. It was found that training with the exoskeleton is less strenuous. However, in terms of ease of use and general patient satisfaction, the orthosis was preferred to the exoskeleton.

In addition to developing exoskeletons with a fixed external structure, the interest in so-called soft-robotic devices is growing. The joints of soft-robotic devices are usually actuated through motor-driven construction hoists. The

flexible structure of the devices allows higher mobility for the patient. However, this is at the expense of greater stability, which is why the systems are particularly suitable for FAC 3 or FAC 4 patients or the elderly.

Furthermore, numerous commercial and research exoskeletons utilize diverse actuation methods, sensing mechanisms, and control algorithms as visualized in Fig. 2.9. An overview of these foundational principles is provided in the subsequent sections.

2.2.2 Actuation Principles

Many different approaches exist in the literature to provide actuation of active lower limb exoskeletons. The choice of actuation is pivotal in determining the efficiency, safety, and performance of these wearable devices. The most common principles using electrical motors are introduced in the following.

Stiff Actuators

Stiff actuators refer to a direct, stiff coupling between the exoskeleton's frame and the human joint as depicted in Fig. 2.10 a). Due to their rigidity, they can provide high precision and force. However, this rigidity might compromise user

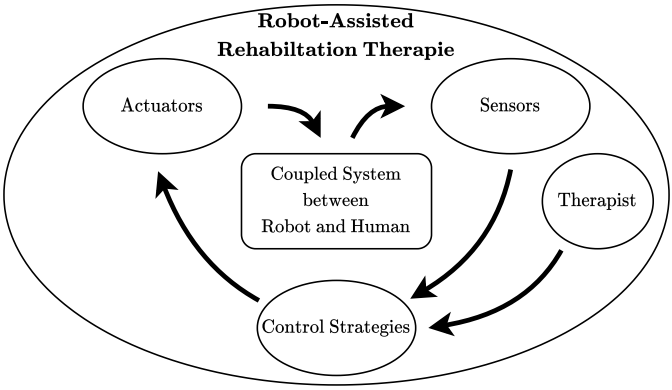

Figure 2.9: In a robot-assisted rehabilitation therapy sensors measure the pose and movement of the coupled human-robot system. Control concepts derive the required motor commands to assist the human in their movement based on the sensor signals. The therapist monitors this process and changes the control settings according to the user's needs.

comfort, and there is a potential risk of exerting unwanted forces on the user, especially if there is a misalignment between the human and exoskeleton joint.

Parallel Elastic Actuators (PEAs)

PEAs, as the name suggests, integrate an elastic component in parallel with the actuator (see Fig. 2.10, b)). This arrangement can reduce the energy consumption of the system, especially in tasks that require the maintenance of a position or posture. The inherent stiffness from the elastic element can support the load, allowing the actuator to operate in a more energy-efficient manner [PBL+21].

Serial Elastic Actuators (SEAs)

As visualized in Fig. 2.10 c) (in black) SEAs incorporate an elastic element in series with the actuator. This design offers advantages like energy storage and shock absorption. The elasticity provides compliant behavior, making interactions with the user more safe and natural. It allows for better force control and can protect the actuator as well as the user by absorbing mechanical shocks [DSDB08].

Variable Stiffness Actuators (VSAs)

VSAs belong to the category of SEAs, but additionally they can adaptively change their stiffness based on the requirements of a task or environment. Various designs for stiffness adaptation exist including changing the effective length of springs with a secondary motor (see Fig. 2.10 c), green part) [LKLM15], changing the spring's preload, e.g. using antagonistic springs with independent

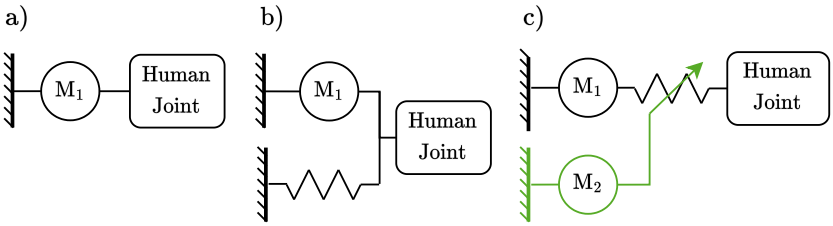

Figure 2.10: Actuator principles. a) Stiff coupling between motor and human joint b) Elasticity in parallel to motor c) Serial elasticity between motor and human joint and variable elasticity using a second motor (green).

motors, or by changing the physical properties of the elastic element, such as pneumatic artificial muscles [VASB+13, HMT+21]. By adjusting the stiffness, these actuators can optimize their performance for various conditions. For instance, they can provide rigidity when high precision is required or become compliant during interactions with dynamic environments. This adaptability enhances energy efficiency, safety, and the ability to absorb external shocks. Furthermore, VSAs can allow exoskeletons to adapt to different users or different stages of rehabilitation, offering a personalized user experience.

Tendon Driven Systems

These systems mimic the human musculoskeletal design by using artificial tendons. The tendons, driven by actuators located distant from the joints, e.g. in a backpack, can produce joint motion [XAG+21]. This decentralized approach reduces the weight on the limbs, enhancing wearability. The flexibility of the tendons offers a more natural and compliant interaction, but the existence and routing of the tendons induce non-linearities, high friction, and backlashes, thus, making the control of these systems challenging and often imprecise. Additionally, many designs, e.g. the Myosuit (MyoSwiss AG, Zurich, Switzerland) only provide assistance in a bi-articular manner, that is the actuation of two joints with one tendon [SDG+17]. For the Myosuit only the extension of the hip and knee joint at the same time is actuated to provide assistance during the stance phase.

2.2.3 Sensor Systems

Sensors play an integral role in the functionality of lower limb exoskeletons. They are the "eyes and ears" of the system, enabling the exoskeleton to perceive, interact with, and respond to its environment, including the person wearing it. Various types of sensors can be integrated into a lower limb exoskeleton. A comprehensive review of the usage of these sensors in exoskeletons was provided by Tiboni et al. [TBV+22]. The information from the sensors introduced in the following is fed into the exoskeleton's control system, which processes the data and adjusts the device's movements in real-time, ensuring synchronized, safe, and effective operation.

Encoders

Typically installed in the joints of the exoskeleton, encoders measure the position, displacement, and rotation of the exoskeleton's parts. This information is essential for controlling the motion and ensuring the alignment with the user's movement.

Force, Torque, and Pressure Sensors

These sensors detect forces applied by or to the user. For example, they can determine the interaction force between the user and the robot. This information can be vital in adjusting the support given by the exoskeleton during walking.

Inertial Measurement Unit (IMU)

IMUs consist of accelerometers, gyroscopes, and optionally of magnetometers. They can determine the orientation, acceleration, and angular velocity of the exoskeleton parts. These measures are essential for the knowledge of the posture and for motion tracking.

Electromyography (EMG) Sensors

EMG measures muscle activity. By detecting which muscles are activated and how intensely they are being used, the exoskeleton can assist the user's movement.

Electroencephalography (EEG) Sensors

While more common in brain-machine interface systems, EEG measures brain activity. When integrated into an exoskeleton, they can help discern the wearer's intention to move or stop, thereby making the system more intuitive.

2.2.4 Control Strategies

The application areas of medical exoskeletons can be divided into two categories depending on the type and severity of the patient's paralysis. In the case of hemi- or paraplegia (complete lateral or transverse paralysis), so-called walkers are used, where the user "is being walked". In the case of hemi- or paraparesis (partial lateral or transverse paralysis), the exoskeletons used are called assist devices, which allow an interaction between user and robot. Both application areas place different requirements on the human-machine interaction, the user interface, and the control strategy of the exoskeleton.

From a technical point of view, the patient and the exoskeleton can be regarded as interconnected subsystems, linked either through a *cognitive human-machine interface* (cHMI) or a *physical human-machine interface* (pHMI) [Pon08]. The cHMI receives the patient's movement intention by measuring electrical body signals almost instantaneously. These intentions can then translate into movement instructions through auditory, visual, or tactile feedback. On the other hand, the pHMI establishes a bidirectional interaction by physically connecting

the patient and the device, enabling the transmission of forces and moments. In specific scenarios, this mechanical connection can also help deduce a patient's intentions.

To determine a patient's walking intention through a cHMI, it is possible to measure brain activity using EEG or assess muscular activity with EMG. For example, Kwak et al. demonstrated that an exoskeleton could be controlled by interpreting a patient's EEG signals [KML15]. In their experiment, five LEDs, each flashing at distinct frequencies, were positioned in front of the participant. By focusing on a specific LED, the EEG signals' amplitude corresponding to that frequency amplified, which was then translated into a movement command for the exoskeleton. Healthy participants quickly adapted to this control method in a few minutes. However, separating between interference and control signals poses a technical difficulty making daily use of EEG-based control a challenging proposition. Furthermore, the positioning of EEG sensors proves to be exceedingly time-intensive, posing an additional barrier to their practical application in everyday scenarios.

The Hybrid Assistive Limb (HAL, Cyberdyne Inc., Tsukuba, Präfektur Ibaraki, Japan) exoskeleton employs EMG-based control and is currently in practical use [HKS05]. Electrodes placed on the skin's surface detect the electrical signals from the extensor and flexor muscles. However, challenges with this approach are that the relationship between electrical muscle activity and muscle force is non-linear and that the measurement signal varies greatly with skin and tissue conductivity.

Model-based control concepts use the interaction forces and moments of the pHMI to infer the patient's intention to move. The majority of the control concepts is based on a model of the overall system (exoskeleton + patient) given by a second-order differential equation as follows [YGZG17]:

$$\mathbf{M}(\mathbf{q})\ddot{\mathbf{q}} + \mathbf{C}(\mathbf{q}, \dot{\mathbf{q}})\dot{\mathbf{q}} + \mathbf{D}\dot{\mathbf{q}} + \mathbf{g}(\mathbf{q}) = \boldsymbol{\tau}_{\text{exo}} + \boldsymbol{\tau}_{\text{pat}} \tag{2.1}$$

The patient's joint torque vector $\boldsymbol{\tau}_{\text{pat}}$ and the exoskeleton's joint torque vector $\boldsymbol{\tau}_{\text{exo}}$, e.g., in the hip and knee joint, are the input variables of the system, and the motion variable vectors $\ddot{\mathbf{q}}, \dot{\mathbf{q}}, \mathbf{q}$ denote the system's outputs. The matrices $\mathbf{M}, \mathbf{C}, \mathbf{D}$ convey the inertial, Coriolis term, and damping torques. The vector $\mathbf{g}$ contains the weight torques caused by gravity. It should be noted that the model in eq. (2.1) neglects the human's joint elasticity. Therefore, the patient input vector comprises active as well as passive (elastic) joint torques. A more detailed deviation of the model in eq. (2.1) is given Sec. 3.3. The most common model-based control strategies are exploited in the following.

Position Control

PID controllers are widely used across different applications and industries due to their easy-to-interpret adjustability and highly achievable control quality. This form of feedback control is also used in exoskeletons, especially in position tracking. The goal is to trace a fixed defined angular trajectory to enable the leg's locomotion.

A cascaded control loop consisting of two controllers for each joint actuator is often implemented to realize position tracking as visualized in Fig. 2.11. The inner control loop consists of a PI controller, which allows to set a target velocity $\dot{\mathbf{q}}_{\mathrm{ref}}(s)$ of the respective joint:

$$\boldsymbol{\tau}_{\mathrm{exo}}(s) = \left(\mathbf{K}_{\mathrm{v,P}} + \mathbf{K}_{\mathrm{v,I}}\frac{1}{s}\right) \cdot \underbrace{\left(\dot{\mathbf{q}}_{\mathrm{ref}}(s) - \dot{\mathbf{q}}(s)\right)}_{\text{Velocity Error}} \tag{2.2}$$

The outer loop provides the velocity reference to follow the target position. A PD structure is usually applied for this purpose. The integral component is often neglected in order to avoid an impermissible increase in force with respect to the patient as a result of a prolonged position deviation.

$$\dot{\mathbf{q}}_{\mathrm{ref}}(s) = \left(\mathbf{K}_{\mathrm{p,P}} + \mathbf{K}_{\mathrm{p,D}} \cdot s\right) \cdot \underbrace{\left(\mathbf{q}_{\mathrm{ref}}(s) - \mathbf{q}(s)\right)}_{\text{Position Error}} \tag{2.3}$$

The cascaded structure has the advantage that the inner control can compensate for friction effects and may thus be neglected in the outer loop.

Position control in exoskeletons allows for navigating the user's legs according to a specific trajectory without deviations. Conversely, this means that the user's own movements are neither detected nor supported. An integral component in the controller can also lead to very high torques in the joints, which can either cause injury to the user or damage to the hardware. Furthermore, pre-recorded, standardized trajectories that do not correspond to the subject's individual gait are usually used as a reference.

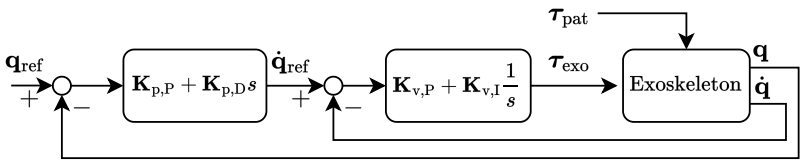

Figure 2.11: Cascaded position control strategy consisting of a PI velocity and a PD position controller.

Impedance Control

Impedance control provides a solution for taking patient movement into account and avoiding very high joint torques in the presence of trajectory deviations. Formally, impedance control considers a physical system acting on the surrounding environment with a required behavior. According to [Hog84] [AOCPG07], mechanical impedance describes the transfer behavior $G_{\mathrm{imp}}(s)$ of the physical system with the motion as input and the torque as output variable:

$$G_{\mathrm{imp}}(s) = \frac{\tau(s)}{\dot{q}(s)}. \tag{2.4}$$

In the following, impedance control for an exoskeleton is provided according to [AOCPG07]. The input variable of the equation of the total system in eq. (2.1) is the total driving torque $\boldsymbol{\tau}$ consisting of the exoskeleton torque $\boldsymbol{\tau}_{\mathrm{exo}}$ and the patient torque $\boldsymbol{\tau}_{\mathrm{pat}}$:

$$\boldsymbol{\tau} = \boldsymbol{\tau}_{\mathrm{exo}} + \boldsymbol{\tau}_{\mathrm{pat}}. \tag{2.5}$$

The patient torque $\boldsymbol{\tau}_{\mathrm{pat}}$ is sometimes a response to the impressed motion of the exoskeleton and should be described and constrained as an impedance. Here, $\mathbf{M}_{\mathrm{d}}$, $\mathbf{D}_{\mathrm{d}}$, and $\mathbf{K}_{\mathrm{d}}$ are the matrices of the desired inertia, damping, and stiffness, respectively.

$$\boldsymbol{\tau}_{\mathrm{pat}} = \mathbf{M}_{\mathrm{d}}\ddot{\mathbf{q}} + \mathbf{D}_{\mathrm{d}} \cdot (\dot{\mathbf{q}}_{\mathrm{ref}} - \dot{\mathbf{q}}) + \mathbf{K}_{\mathrm{d}} \cdot (\mathbf{q}_{\mathrm{ref}} - \mathbf{q}). \tag{2.6}$$

Eq. (2.6) is solved for $\ddot{\mathbf{q}}$ and substituted into the equation of the total system given by eq. (2.1). From this, the exoskeleton torque is derived as follows:

$$\boldsymbol{\tau}_{\mathrm{exo}} = \mathbf{M}\mathbf{M}_{\mathrm{d}}^{-1}(\boldsymbol{\tau}_{\mathrm{pat}} - \mathbf{D}_{\mathrm{d}} \cdot (\dot{\mathbf{q}}_{\mathrm{ref}} - \dot{\mathbf{q}}) - \mathbf{K}_{\mathrm{d}} \cdot (\mathbf{q}_{\mathrm{ref}} - \mathbf{q})) + \mathbf{C}(\mathbf{q}, \dot{\mathbf{q}})\dot{\mathbf{q}} + \mathbf{D}\dot{\mathbf{q}} + \mathbf{g} - \boldsymbol{\tau}_{\mathrm{pat}}. \tag{2.7}$$

This equation provides the primary form of most impedance controls in exoskeletons [IS15] and it is visualized in Fig. 2.12 The matrices of damping $\mathbf{D}_{\mathrm{d}}$ and stiffness $\mathbf{K}_{\mathrm{d}}$ are usually set empirically within the determined stability bounds [GZG18].

A special variant of impedance control may be obtained by inserting $\mathbf{M} \stackrel{!}{=} \mathbf{M}_{\mathrm{d}}$ in eq. (2.7). This simplification removes the human torque $\boldsymbol{\tau}_{\mathrm{pat}}$ compensation and makes the impedance control similar to the PD control approach presented in the previous paragraph, which is why the PD control is also called the natural impedance control:

$$\boldsymbol{\tau}_{\mathrm{exo}} = -\mathbf{D}_{\mathrm{d}} \cdot (\dot{\mathbf{q}}_{\mathrm{ref}} - \dot{\mathbf{q}}) - \mathbf{K}_{\mathrm{d}} \cdot (\mathbf{q}_{\mathrm{ref}} - \mathbf{q}) + \mathbf{C}(\mathbf{q}, \dot{\mathbf{q}})\dot{\mathbf{q}} + \mathbf{D}\dot{\mathbf{q}} + \mathbf{g}. \tag{2.8}$$

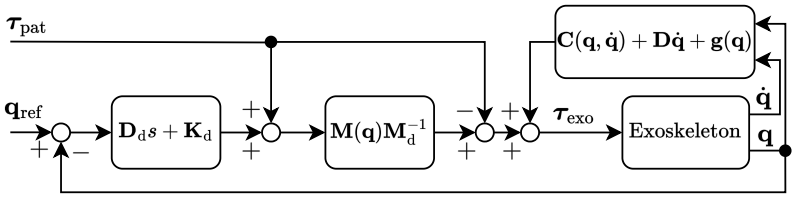

Figure 2.12: Common impedance control strategy. The human torque compensation can be removed by setting $\mathbf{M} \stackrel{!}{=} \mathbf{M}_{\text{d}}$. Modified from [IS15].

Force/Torque Feedback Control

Force/Torque feedback control provides the patient with the highest cooperation among model-based control strategies. Measuring the interaction forces between the exoskeletal structure and the human body provides information that can be used to estimate the patient's intention to move in terms of the torque applied by the patient $\boldsymbol{\tau}_{\text{pat}}$. These control strategies require additional sensors, such as *force-torque sensor* (FTS) as, for example, used in the HIT-LEX exoskeleton [ZZL+16].

In turn, the measured interaction torque can be used to support the patient in the moving direction. One possible control procedure is shown in Fig. 2.13; the control approach is denoted by the blocks on the left of the dashed line.

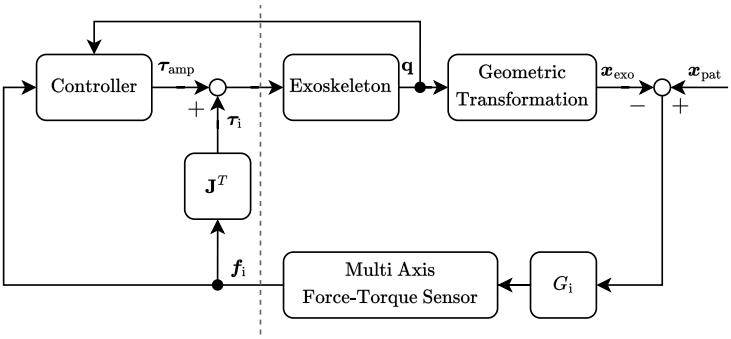

Figure 2.13: Force/torque feedback control. Figure modified from [GZG18].

A movement initiated by the patient leads to a displacement between the exoskeleton's position $\boldsymbol{x}_{\text{exo}}$ and the human body $\boldsymbol{x}_{\text{pat}}$, e.g. through compliance in the system. The displacement is converted into interaction forces $\mathbf{f}_i$ via a human-robot interaction model $\mathbf{G}_i$, which can be measured, e.g., through FTS. The human-robot interaction model can typically be described by a simple spring or spring-damper model [GZG18]. The interaction forces $\boldsymbol{f}_i$ measured with the FTS are transformed to the joint interaction torques $\boldsymbol{\tau}_i$ via the Jacobian matrix of the exoskeleton $\mathbf{J}^T$ to assist in the direction of the interaction torques (see Fig. 2.13). In addition to this term of assistance, a second assistance term can be added by the control law given as follows:

$$\boldsymbol{\tau}_{\text{amp}} = \mathbf{J}^T \mathbf{K} \mathbf{f}_i - \mathbf{K}_{\text{d}} \dot{\mathbf{q}} + \mathbf{g} \tag{2.9}$$

Here, the interaction forces $\boldsymbol{f}_i$ are amplified by the gain $\mathbf{K}$, which is also projected onto the joints using $\mathbf{J}^T$. With the quantity $\mathbf{K}_{\text{d}}$, the desired damping is set, and with the gravity matrix $\mathbf{g}$, the weight of the exoskeleton is compensated.

The control law in eq. (2.9) and the interaction torque $\boldsymbol{\tau}_i = \mathbf{J}^T \mathbf{f}_i$ form the desired assistance torque $\boldsymbol{\tau}_{\text{exo}} = \boldsymbol{\tau}_{\text{amp}} + \boldsymbol{\tau}_{\text{i}}$. This torque is induced to the equation of the total exoskeleton system in eq. (2.1) as shown in Fig. 2.13:

$$\mathbf{M}\ddot{\mathbf{q}} + \mathbf{C}\dot{\mathbf{q}} + (\mathbf{D} + \mathbf{K}_d)\dot{\mathbf{q}} = \mathbf{J}^T(\mathbf{K}\boldsymbol{f}_i + \boldsymbol{f}_i) \tag{2.10}$$

Thus, the weight compensation and the gain factor $\mathbf{K}$ are introduced into the overall controlled system. Additionally, the exoskeleton follows the interaction forces originating from the patient's motion in a reinforcing manner.

2.3 System Theoretical Fundamentals

System theoretical concepts are applied in all parts of this thesis. The most important principles, in particular of system identification and state estimation, are presented in the following. The control of dynamic processes also belongs to the field of systems theory. However, an overview of the most common control concepts for lower limb exoskeletons has already been given in the previous section and is therefore not discussed in more detail in this section.

2.3.1 System Identification

System identification plays a crucial role in the design and validation of technical systems. This domain involves the design and choice of model, identification of model parameters, design of experiments, selection of inputs, and the application

of optimization techniques. For a more detailed explanation of these aspects, refer to the books by Nelles [NEL20] and Isermann [IM11].

A model $f(u, \theta)$ is a mathematical representation of its physical process and it is typically characterized by its input u, parameters θ, and output $\hat{y}$. The main goal in the design of a model is its capability to produce an output that closely mirrors the output of the actual physical process when the same input is applied, thus minimizing the error between the process and model output $e = y - \hat{y}$ as depicted in Fig. 2.14. It should be noted that a perfect match between the model and process is almost impossible as the process is usually affected by noise n. When designing the model, the inputs, model complexity, order, and linearity need to be considered. A guiding principle during this design phase is the mantra: *As simple as possible, as complex as necessary.* This principle underscores the need for a balance between simplicity for usability and complexity for accuracy.

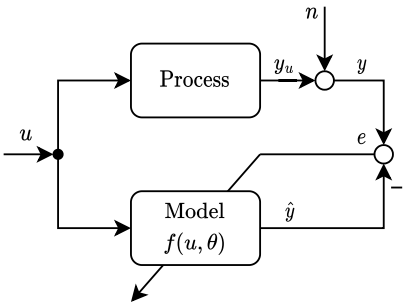

Figure 2.14: Components of system identification for static processes using the output error. The objective is to configure a model that minimizes the discrepancy between the actual process output and the predicted model output. Modified from [NEL20].

Once the basic structure of the model is specified, the model parameters need to be specified. This can be approached in three different ways: black box, white box, and grey box modeling. In white box modeling, the model parameters are directly extracted from measurable physical quantities and properties. It is an approach rooted in known physical laws and principles. Black box modeling, on the other hand, is more empirical. Here, the model parameters are derived by solving an optimization problem, the objective of which is to minimize the discrepancy or error between the model's output and the actual process output. Grey box modeling acts as a bridge between the white and black box methods

by integrating the known physical parameters directly into the model, while optimization techniques are employed to determine the unknown ones. One notable optimization technique for linear systems is the well-known least squares estimation, which is explained in more detail in the subsequent section.

2.3.2 Parameter Estimation

The model parameters can be estimated by solving an optimization problem. In the choice of the optimization problem, it should be differentiated between linear and non-linear optimization problems as well as parameter constraints.

Least Squares Estimation

When the error between the process and model output is linearly dependent on the parameters, and the squared sum of errors is used as a loss function, the optimization problem becomes linear as is the case in static processes or finite impulse response filters. Furthermore, even if the error stems from a nonlinear function of the parameters, a linear optimization problem can be formulated by selecting the loss function as a sum of the inverse non-linearities associated with the errors [NEL20]. In these cases, the least squares method can be used to quantify the system's parameters. The objective is to determine a model output $\hat{y}$ that closely mirrors the actual process output y, aiming for the smallest value of the sum of squared error loss function [NEL20].

The input $\mathbf{u} = \begin{bmatrix} u(1) & \dots & u(N) \end{bmatrix}^T$ and output $\mathbf{y} = \begin{bmatrix} y(1) & \dots & y(N) \end{bmatrix}^T$ vectors can be defined assuming the input $u(i)$ and $y(i)$ have been recorded for $i = 1, \dots, N$ data samples [NEL20]. Note that the model output $\mathbf{y}$ is being subject to process noise n as depicted in Fig. 2.14. In combination with the assumption of n model parameters $\boldsymbol{\theta} = \begin{bmatrix} \theta_1 & \dots & \theta_n \end{bmatrix}^T$ the regressor $\mathbf{X}$ can be formulated as:

$$\mathbf{X} = \begin{bmatrix} x_1(1) & x_2(1) & \dots & x_n(1) \\ x_1(2) & x_2(2) & \dots & x_n(2) \\ \vdots & \vdots & & \vdots \\ x_1(N) & x_2(N) & \dots & x_n(N) \end{bmatrix} = \begin{bmatrix} \mathbf{x}_1 & \mathbf{x}_2 & \dots & \mathbf{x}_n \end{bmatrix}, \tag{2.11}$$

where x_i are functions of the input u. Please refer to [NEL20] for examples of how to choose the regressor for different problems.

The model output $\hat{\mathbf{y}} = \begin{bmatrix} \hat{y}(1) & \dots & \hat{y}(N) \end{bmatrix}^T$ can then be written as

$$\hat{\mathbf{y}} = \mathbf{X}\boldsymbol{\theta} \tag{2.12}$$

and the cost function J to be minimized can be formulated as

$$J = \frac{1}{2}\mathbf{e}^T\mathbf{e} \qquad \text{with} \qquad \mathbf{e} = \mathbf{y} - \hat{\mathbf{y}} = \mathbf{y} - \mathbf{X}\boldsymbol{\theta}, \tag{2.13}$$

where $\mathbf{e}$ is the error vector between process and model [NEL20]. The cost function is parabolic in the parameter vector θ

$$J(\theta) = \frac{1}{2}\boldsymbol{\theta}^T\mathbf{H}\boldsymbol{\theta} + \mathbf{h}^T\boldsymbol{\theta} + \frac{1}{2}h_0 \tag{2.14}$$

with

$$\mathbf{H} = \mathbf{X}^T\mathbf{X}, \tag{2.15}$$

$$\mathbf{h} = -\mathbf{X}^T\mathbf{y}, \tag{2.16}$$

$$h_0 = \mathbf{y}^T\mathbf{y} \tag{2.17}$$

being the Hessian, a linear term, and a constant term, respectively [NEL20]. For the optimum of the minimization problem, it holds that the error $\mathbf{e}$ is orthogonal to all regressor vectors $\mathbf{x}_i$ leading to the least squares estimate of the parameters:

$$\hat{\boldsymbol{\theta}} = (\mathbf{X}^T\mathbf{X})^{-1}\mathbf{X}^T\mathbf{y}. \tag{2.18}$$

One special but important case is the least squares estimation for general dynamic models of the form

$$G(z^{-1}) = \frac{y(z)}{u(z)} = \frac{b_0 + b_1 z^{-1} + \ldots + b_m z^{-m}}{1 + a_1 z^{-1} + \ldots + a_m z^{-m}} = \frac{B(z^{-1})}{A(z^{-}1)} \tag{2.19}$$

We note that, for this kind of process the assumption that the output is only linearly dependent on the input u does not hold anymore. For this reason, the *generalized equation error* is introduced by using the measured values $y(k)$ instead of the true output $y_u(k)$ and the estimated parameters $\hat{a}_i$ and $\hat{b}_i$ instead of the true parameters [IM11]:

$$\begin{aligned} e(k) = y(k) + \hat{a_1}(k-1)y(k-1) + \ldots + \hat{a}_m(k-1)y(k-m) \\ - \hat{b}_1(k-1)u(k-1) - \ldots - \hat{b}_m(k-1)u(k-m) \end{aligned} \tag{2.20}$$

The generalized equation error for the parameter estimation of dynamic systems is visualized in Fig. 2.15. The regression matrix $\mathbf{X}$ for N measurements and the parameter vector $\boldsymbol{\theta}$ become in this case:

$$\mathbf{X} = \begin{bmatrix} u(m) & \ldots & u(1) & -y(m) & \ldots & -y(1) \\ u(m+1) & \ldots & u(2) & -y(m+1) & \ldots & -y(2) \\ \vdots & & \vdots & \vdots & & \vdots \\ u(N-1) & \ldots & u(N-m) & -y(N-1) & \ldots & -y(N-m) \end{bmatrix} \tag{2.21}$$

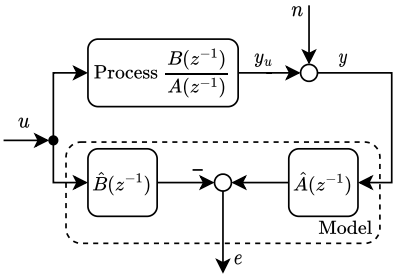

Figure 2.15: Components of system identification for discrete-time linear processes using the generalized error. The objective is to configure a model that minimizes the discrepancy between the actual process output and the predicted model output. Modified from [NEL20].

$$\boldsymbol{\theta} = \begin{bmatrix} \hat{b}_1 & \dots & \hat{b}_m & \hat{a}_1 & \dots & \hat{a}_m \end{bmatrix}^T \tag{2.22}$$

Note, that at least $N = 2m$ equations are required to determine the $2m$ parameters. In practice, typically $N \gg 2m$ is chosen to suppress the influence of the disturbance in the measurements [IM11].

For more information, the reader is referred to [NEL20] and [IM11].

Parameter Estimation for Non-linear Systems

There exist several possibilities to optimize parameters when the optimization problem is non-linear including batch and sample adaptation, direct search algorithms and gradient-based algorithms such as Newton's method. In general, these approaches do not impose any requirements on the cost function except for its smoothness [NEL20]. However, the most common cost function is a weighted quadratic cost function:

$$J(\theta) = \sum_{i=1}^{N} f^2(i, \theta) \tag{2.23}$$

The function f usually refers to the residual (error). If f is a nonlinear function, the optimization problem is a nonlinear least squares problem. The two most popular algorithms to solve such a problem are the gradient-based methods of Gauss-Newton and Levenberg-Marquardt. Both methods are iterative optimization techniques that linearize the model by approximating the cost function as a first-order Taylor series expansion. Secondly, the parameter estimation

is iteratively refined until convergence is achieved. The Levenberg-Marquard method additionally introduces a regularization term to better handle situations where the linearization may not be accurate or when the problem is ill-conditioned, thus, making it more robust compared to the Gauss-Newton method. For further detail, refer to [NEL20].

These two methods are not well suited when equality constraints h or inequality constraints g on the parameters need to be introduced. In this case, the optimization problem can be formulated as

$$J() \rightarrow \min_{\boldsymbol{\theta}} \tag{2.24}$$

subject to

$$g_i(\boldsymbol{\theta}) \leq 0 \qquad i = 1, \ldots, m, \tag{2.25}$$

$$h_j(\boldsymbol{\theta}) = 0 \qquad j = 1, \ldots, l. \tag{2.26}$$

Parameter constraints are especially useful for grey box modeling, for example, to retain the physical meaning of specific parameters. The Gauss-Newton method and Levenberg-Marquardt method can only incorporate parameter constraints by introducing penalty or barrier functions in the cost function that penalize violations of the constraints. A more powerful way to handle parameter constraints in non-linear systems is to use *sequential quadratic programming* (SQP). At each iteration, SQP constructs a quadratic approximation of the objective function and a linear approximation of the constraints. The resulting quadratic program is then solved to obtain a search direction. A line search is then performed along this direction to determine the step size. For further information, it is referred to [Van84].

2.3.3 State Estimation

State estimation refers to the process of estimating the internal states of a dynamic system based on available measurements, typically when not all states are directly measurable. Accurate knowledge of the system's internal states is pivotal for more effective control and decision-making.

One of the most famous filter methods for state estimation is the *Kalman filter* (KF). This filter was designed to reduce errors in measurements and to provide estimations for non-measurable state variables. The original KF is rooted in the state-space formulation of linear dynamic systems [Hay04] and was presented by R. Kalman in 1960 [Kal60]. The idea of a KF is to use the state information $\boldsymbol{x}_{k-1}$ of a system at discrete time $k-1$ in combination with a linear system model and its inputs $\boldsymbol{u}_k$ to predict the current state of the system at time k. In a second step, measured system variables $\boldsymbol{z}_k$ at the

current time k are used to correct and improve this prediction. Both, measured values and model-predicted state values, are expected to be subjected to zero mean multivariate Gaussian noise. Therefore, the KF utilizes the mean and the covariance in its update rules as a state representation [JU04]. The weighting between the measured and the predicted value used for the update of the state estimation is defined by the so-called Kalman gain. The disadvantage of the KF is its consideration of only linear systems. This requires significant simplifications for many systems which leads to errors in the estimation.

A further development of the linear KF is the *extended Kalman filter* (EKF). The EKF is able to estimate states of nonlinear systems of the form

$$\boldsymbol{x_k} = \boldsymbol{f}(\boldsymbol{x}_{k-1}, \boldsymbol{u}_k) + \boldsymbol{w}_k \tag{2.27}$$

$$\boldsymbol{z_k} = \boldsymbol{h}(\boldsymbol{x}_k) + \boldsymbol{v}_k, \tag{2.28}$$

where $\boldsymbol{x}_k$, $\boldsymbol{u}_k$ and $\boldsymbol{z_k}$ denote the state, input and measurement vectors at discrete time k, respectively. The idea is the same as for the KF but the prediction of the new states is conducted by calculating the partial derivatives of $\boldsymbol{f}(\boldsymbol{x}_{k-1}, \boldsymbol{u}_k)$ (Jacobian matrix) in order to linearize the model in every step. The same has to be done for $h(\boldsymbol{x}_k)$ when the predicted states are updated by the new measurements. The EKF has become a standard approach in state estimation of nonlinear systems and is probably the most widely used algorithm in this area [JU04]. EKFs are used in the evaluation of radar signals, in positioning and localization problems, including space travel applications, but also in electrical feedback controllers and communication systems. However, the EKF has some drawbacks that are not negligible. First, the EKF is difficult to implement and to tune. Additionally, it is only reliable for systems that are almost linear [JU04]. These drawbacks come from the linearization which is done in every prediction and update step. Furthermore, this linearization requires the computation of two Jacobians in every update step which can be difficult, computationally intensive, and error-prone [JU04]. These drawbacks motivated Julier and Uhlmann in 1997 to design a filter that can be applied to nonlinear systems without the linearization steps required by the EKF, called the *unscented Kalman filter* (UKF) [JU97].

Unscented Kalman Filter (UKF)

In order to apply the KF to nonlinear systems and omit the linearization step in between, an approximation for an arbitrary nonlinear function of transformation is needed. The UKF, on the other hand, does not try to approximate this nonlinear function of transformation. Instead, it approximates a probability distribution from a given set of points which is easier than approximating

an arbitrary nonlinear function of transformation [Uhl94]. To perform this approximation, the UKF uses a set of points (sigma points) with a certain mean $\bar{\boldsymbol{x}}$ and covariance $\boldsymbol{\Sigma}_x$ [JU04]. The nonlinear function is then applied to each of these points. Afterwards, a probability distribution of the transformed points is calculated which represents an estimate of the mean and covariance obtained by the nonlinearly transformed sigma points [JU04]. This principle is visualized in Fig. 2.16.

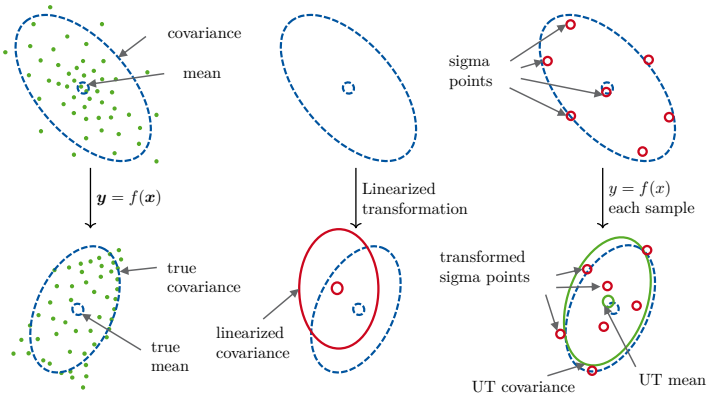

Figure 2.16: Nonlinear, linearized and unscented transformation. Modified from [WV00].

Mathematically, this idea is described in [WV00]. In the first step, the sigma points $\mathcal{X}_i$, with $i \in 0 \ldots 2N$, where N is the dimension of the system, are generated as follows [WV00]:

$$\boldsymbol{\mathcal{X}}_{0,k-1} = \bar{\boldsymbol{x}}_{k-1}, \tag{2.29}$$

$$\boldsymbol{\mathcal{X}}_{i,k-1} = \bar{\boldsymbol{x}}_{k-1} + \left(\sqrt{(n+\lambda)\boldsymbol{\Sigma}_{x,k-1}}\right)_i \quad \text{, for } i = 1 \ldots N, \tag{2.30}$$

$$\boldsymbol{\mathcal{X}}_{i,k-1} = \bar{\boldsymbol{x}}_{k-1} + \left(\sqrt{(n+\lambda)\boldsymbol{\Sigma}_{x,k-1}}\right)_{i-n} \text{, for } i = N+1 \ldots 2N, \tag{2.31}$$

where $\bar{\boldsymbol{x}}_{i,k-1}$ and $\boldsymbol{\Sigma}_{x,k-1}$ are the mean and the covariance of the Gaussian distribution at time $k-1$. How far the sigma points should be chosen from the mean is denoted by the scaling factor $\lambda = \alpha^2(N+\kappa) - N$. The parameter α is usually set to a small positive value denoting the spread of the sigma points around $\bar{\boldsymbol{x}}$. The parameter β is equal to two for Gaussian distributions and $\kappa = 0$,

which is a second scaling parameter [WV00]. To recalculate the distribution after the nonlinear transformation, each sigma point obtains a weighting

$$W_0^m = \frac{\lambda}{N+\lambda}, \tag{2.32}$$

$$W_0^c = \frac{\lambda}{N+\lambda} + (1 - \alpha^2 + \beta), \tag{2.33}$$

$$W_i^m = W_i^c = \frac{1}{2(N+\lambda)} \qquad \text{, for } i = 1 \dots 2N. \tag{2.34}$$

The second step is to transform the set of the given sigma points by instantiating each point through the system model [JU97]

$$\boldsymbol{\mathcal{X}}_{i,k|k-1} = \boldsymbol{f}\left(\boldsymbol{\mathcal{X}}_{i,k-1}, \boldsymbol{u}_k\right) \coloneqq \boldsymbol{f}\left(\boldsymbol{\mathcal{X}}_i\right) \text{ for } i = 1 \dots 2N. \tag{2.35}$$

The new predicted mean and covariance can then be calculated by using the weightings in eqs. (2.32) to (2.34) and the nonlinearly transformed set of sigma points

$$\bar{\boldsymbol{x}}_k^- = \sum_{i=0}^{2N} W_i^m \boldsymbol{\mathcal{X}}_{i,k|k-1}, \tag{2.36}$$

$$\boldsymbol{\Sigma}_{x,k}^- = \sum_{i=0}^{2N} W_i^c \left(\boldsymbol{\mathcal{X}}_{i,k|k-1} - \bar{\boldsymbol{x}}_k^-\right)\left(\boldsymbol{\mathcal{X}}_{i,k|k-1} - \bar{\boldsymbol{x}}_k^-\right)^T. \tag{2.37}$$

Subsequently, the difference between the predicted values and the values given by measurements is computed. To do so, the predicted states are transformed into the measurement space and their mean and covariance are calculated

$$\boldsymbol{\mathcal{Z}}_{i,k|k-1} = \boldsymbol{h}\left(\boldsymbol{\mathcal{X}}_{i,k-1}\right), \tag{2.38}$$

$$\bar{\boldsymbol{z}}_k^- = \sum_{i=0}^{2N} W_i^m \boldsymbol{\mathcal{Z}}_{i,k|k-1}, \tag{2.39}$$

$$\boldsymbol{\Sigma}_{z,k} = \sum_{i=0}^{2N} W_i^c \left(\boldsymbol{\mathcal{Z}}_{i,k|k-1} - \bar{\boldsymbol{z}}_k^-\right)\left(\boldsymbol{\mathcal{Z}}_{i,k|k-1} - \bar{\boldsymbol{z}}_k^-\right)^T. \tag{2.40}$$

At this point, in a normal KF or the EKF, the Kalman gain needs to be calculated to estimate the error in the prediction process. Instead, for the UKF, the cross-correlation between the sigma points in state space and the sigma points in measurement space $\boldsymbol{\Sigma}_{xz}$ needs to be calculated

$$\boldsymbol{\Sigma}_{xz,k} = \sum_{i=0}^{2N} W_i^c \left(\boldsymbol{\mathcal{X}}_{i,k|k-1} - \bar{\boldsymbol{x}}_k^-\right)\left(\boldsymbol{\mathcal{Z}}_{i,k|k-1} - \bar{\boldsymbol{z}}_k^-\right)^T. \tag{2.41}$$

Thus, the Kalman gain for the UKF can be calculated by

$$\boldsymbol{\mathcal{K}} = \boldsymbol{\Sigma}_{xz,k}\boldsymbol{\Sigma}_{z,k}^{-1}. \tag{2.42}$$

This gain is used to update the predicted mean and covariance with the measurements

$$\bar{\boldsymbol{x}}_k = \bar{\boldsymbol{x}}_k^- + \boldsymbol{\mathcal{K}}\left(\boldsymbol{z}_k - \bar{\boldsymbol{z}}_k^-\right), \tag{2.43}$$

$$\boldsymbol{\Sigma}_{x,k} = \boldsymbol{\Sigma}_{x,k}^- - \boldsymbol{\mathcal{K}}\boldsymbol{\Sigma}_{z,k}\boldsymbol{\mathcal{K}}^T. \tag{2.44}$$

The eqs. (2.43) and (2.44) provide an estimation of the states at time k represented by their mean and covariance. If the previous procedure is repeated for every discrete time step, a state estimation of a nonlinear system is obtained.

3 Design, Modeling and Human Torque Estimation

Reliable, safe hardware is the core component in rehabilitation robotics. In addition, a detailed model and the estimation of the patient's movement intention are essential for human-cooperative control of the hardware. Therefore, this chapter presents the development of a lower limb exoskeleton with variable stiffness actuators. Subsequently, a system identification of the human-robot system and an estimation method for the human joint torque are presented. The main content of this chapter has been published in the peer-reviewed journal article [BLV+22] (© 2022 IEEE) while the stance phase model presented in this chapter has been published in [BVLN23] (© 2023 IEEE).

3.1 Motivation

Especially in the rehabilitation therapy of patients with residual function, e.g., after a stroke, exoskeletons can bring great benefit for therapists and people with paresis as described in Sec. 2.2.1. However, one of the challenges in developing these systems is patient integration and human-robot coupling. As described in Sec. 2.2.2, current research focuses on introducing soft or compliant coupling between actuator systems and the patient to ensure safe *physical human-machine interface* (pHMI) while taking the unknown and changeable environment under consideration [DSDB08].

As described in Sec. 2.2.2, exoskeletons with compliant actuators such as *serial elastic actuators* (SEAs) or *variable stiffness actuators* (VSAs) [WWM+14, JBG+14, GRGG+17, SVGVT+19, ZWCZ22] are characterized by higher mass and lower flexibility than soft robotic devices. However, they benefit from lower friction, and more efficient actuation [VKH+07, WWM+14]. Additionally, the fixed external structure of the exoskeleton offers a significant advantage in that the position and movement of the subject can be determined more precisely.

Tab. 3.1 lists recent lower limb exoskeletons for rehabilitation therapy and their specifications. Most of the actuators used in current exoskeletons are either stiff or compliant with a fixed serial elasticity [WWM+14, BVZ+15, LFR20]. However, variable compliance allows changing the coupling behavior during the gait phases. For example, a high torque control bandwidth and stiff coupling can be provided for the stance phase, while high compliance can reduce resistance during the swing phase [ZWCZ22]. Those exoskeletons in Tab. 3.1 which provide a varying stiffness are either manually changeable or automatically adjustable at a very low speed and, thus, cannot adjust the stiffness during one gait cycle [JBG+14, GRGG+17]. For this reason, the VSA-EXO provides a high rate of stiffness change, but only in the knee joint [ZWCZ22]. However, coupling multiple VSAs imposes new requirements on state estimations and

Table 3.1: Specifications of different lower limb exoskeletons. (© 2022 IEEE)

Exoskeleton	Year	Joints	Compliance			Nom.	Weight	
			Type	Stiffness	Mech-	Torque	Total	Joint
		H/K/A		[Nm/rad]	anism	[Nm]	[kg]	[kg]
MindWalker [WWM+14]	2014	a/a/a	SEA	800	fix	100	28	2.9
MIRAD [JBG+14]	2014	a/a/a	VSA	[60, 150]	manual	15	13	1.4
H2 [BVZ+15]	2015	a/a/a	None	-	-	35	12	N/S
ALTACRO [GRGG+17]	2017	a/a/a	VSA	[5, 110]	auto.	40	N/S	2.4
VSA-EXO [ZWCZ22]	2022	p/a/p	VSA	[60, 150]	auto.	N/S	7.6	N/S

H/K/A: Hip/Knee/Ankle; a/p: active/passive;
Nom.: Nominal; auto.: automatic; N/S: not specified

control approaches due to high nonlinearities.

Another key challenge that multi *degree-of-freedom* (DoF) exoskeletons face is estimating the torque the participant is actively applying to the system in different joints, corresponding to the patient's motion intention. This knowledge is essential, e.g., for patient cooperative control strategies or patient condition quantification. Several approaches in the literature address the human joint torque estimation, e.g., using inverse dynamics [LDZ+18, QGCC21] (see Sec. 2.1.4) or by learning the patient's movements [QGCC21].

The model-based approach using inverse-dynamics has the advantage that no additional electrodes are necessary, as is the case for *electromyography* (EMG) based approaches. However, inverse dynamics requires an accurate model of the considered system; in particular, the test subject's mass, mass distribution, inertia, and friction parameters are required. Another challenge in the calculation of inverse dynamics is the calculation of the angular velocities and accelerations of the joints by means of discrete derivatives of the encoder signals in combination with low-pass filters [TM01]. This derivation leads to either a high noise or a high time delay, which critically affects the subsequent control. The goal for the design of the torque estimation is to cover the dynamic range of human joints, which are 4 Hz and 5 Hz for the hip and knee, respectively [Smi08].

Since the motion of the overall system results from a superposition of motor and human joint torque, another requirement in the inverse dynamic approach is

the determination of the interaction torque between the motor and the subject. This requires additional *force-torque sensor* (FTS) (see Sec. 2.2.4) or complex estimation algorithms since a high gear ratio in the actuator system often leads to poor back-drivability of the actuation system [SLC19]. Hwang et al., for example, used an additional torque sensor at the output shaft of a rigid actuator [HJ15]. Based on this, they applied the inverse dynamics approach to derive the active human joint torques during the swing phase. SEAs or VSAs can offer another solution to this challenge. The serial elasticity between the gear and the human joint not only provides soft coupling but it can also be used as a torque sensor. For example, Huo et al. utilized a SEA to measure and estimate the interaction and human joint torque during the sit-to-stand task [HMAK16].

In summary, to the best of the author's knowledge, there are no VSA-based exoskeletons capable of adapting both hip and knee stiffness during a gait cycle to date. Moreover, new VSA-based methods for estimating patient motion intention with low delay should be investigated in more detail. For this reason, this chapter aims, first, to develop a *lower limb exoskeleton with serial elastic actuators* (L^2Exo-SE) and, second, to detect the subject's movement intention without equipping the human with additional sensors. The main contributions of this chapter include:

1. the mechanical design and sensor setup of the L^2Exo-SE based on the *mechanical-rotary variable impedance actuator* (MeRIA) proposed in [LLM16, LLNM20]. The compliant actuator is integrated for hip and knee actuation and provides online stiffness adjustment during one gait cycle (see Sec. 3.2). Furthermore, the effectiveness of the *linear quadratic Gaussian* (LQG) torque controller proposed in [LLNM20] is verified in the case of exoskeleton-assisted walking.

2. a new identification routine to quantify individual model parameters of the exoskeleton's wearer (see Sec. 3.3).

3. a new model-based, non-linear approach to estimate the joint torques the user applies to the system. For this, the serial elasticity and an *unscented Kalman filter* (UKF) are utilized during the swing phase and a static model is used for the stance phase. The estimation method is applicable over the entire stiffness range of the actuator and thus transferable to other SEA and VSA designs.

3.2 Lower Limb Exoskeleton - Serial Elasticity

In the following, the actuator, the structural design of the exoskeleton, including the sensor system, and a model and low-level control of the individual joint motors is presented.

3.2.1 Mechanical Design

The developed exoskeleton was designed to support patients with hemiplegia, e.g., for rehabilitation after a stroke. For this purpose, it was equipped with six DoF to allow for flexion and extension of both legs' ankle, knee, and hip joint in the sagittal plane as shown in Fig. 3.1. Active support is provided unilaterally in the knee and hip joint. Passive support is provided for the ankle joints through springs. Hard plastic shells achieve the fixation between the exoskeleton and the human subject on the hip, thigh, and lower leg. The weight is grounded via carbon footrests in the shoes allowing partial rolling of the foot. Telescopic rails in the frame enable the exoskeleton to be adapted for subjects with a leg length (from ground to the hip joint) between 82.8 cm and 101 cm. These lengths correspond to an approximated body height between

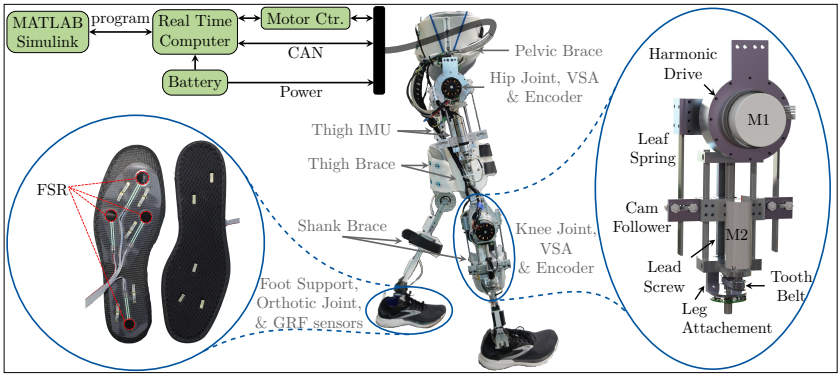

Figure 3.1: Lower Limb Exoskeleton with VSAs in hip and knee joint. The control is performed by a real-time computer and two motor controllers for the hip and knee VSAs. The encoder, IMU, and FSR data are transmitted to the computer via CAN bus. Motor 1 (M1) provides the assistance torque for the respective joint, while Motor 2 (M2) varies the stiffness by changing the effective length of the leaf springs. (© 2023 IEEE)

158 cm and 192 cm[1]. The entire exoskeleton, including cables and shoes, weighs 14.4 kg. The power supply for the actuators and sensors is provided by a 48 V battery with 30 A h, which was placed on a separate wheeled walker for weight reduction. The walker ensures the mobility of the exoskeleton and provides additional support and safety for the subject. In addition to the battery, two motor controllers (Escon 70/10, Maxon Motor AG, Sachseln, Switzerland) have been placed on the walker for the current control of the main motors of the L^{2}Exo-SE. A detailed description of the motorized walker including a hands-free steering approach is given in [BHLN22].

3.2.2 Compliant Actuation

Actuation of the hip and knee joints is provided by the *mechanical-rotary variable impedance actuator* (MeRIA) [LLM16, LLNM20]. Fig. 3.2a depicts the design of the MeRIA for the hip/knee (H/K) joint. Each MeRIA actuator

[1]The body height was calculated using a lower limb to body height ratio of 0.525 as a reference. However, it's important to note that this ratio may vary significantly among individuals.

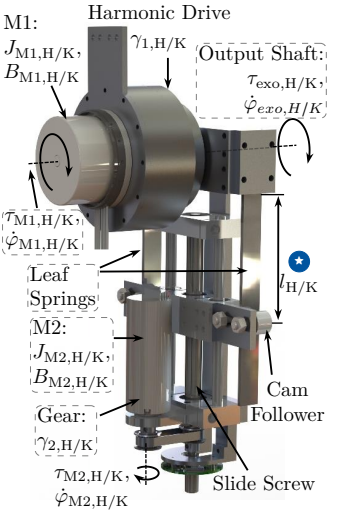

(a) Conceptual design of the MeRIA.

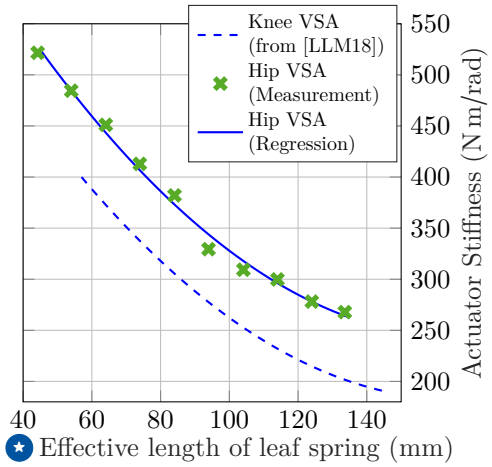

(b) Stiffness values in dependence of the effective length of the leaf spring for the hip and knee actuator.

Figure 3.2: Design and stiffness properties of the MeRIA. (© 2022 IEEE)

consists of two motors. Motor 1 (M1, EC60 Flat, 150 W, Maxon Motor AG, Sachseln, Switzerland) generates the main torque τ_{M1} for the joint actuation. The torque is transferred to the human joint via a harmonic drive (Harmonic Drive SE, Limburg a. d. Lahn, Germany) and two leaf springs (Hardened spring band EN10132-4, C85S+QT). The gear transmission $\gamma_{1,\mathrm{H/K}}$ varies between the hip (1:160) and the knee (1:100) VSAs to account for the different torque and velocity requirements during the gait. The task of the second motor (M2, BX4 Brushless DC, Faulhaber, Schönaich, Switzerland) is to adjust the effective length $l_{\mathrm{H/K}}$ of the leaf springs by moving the position of four cam followers via the rotation of the slide screw with the velocity $\dot{\varphi}_{\mathrm{M2,H/K}}$ (see Fig. 3.2a). The varying effective length results in a change of the coupling elasticity $\sigma(l)$ between M1 and the human joint. The serial elasticity is not only used for a smooth coupling between the exoskeleton and the patient, but it also functions as an integrated torque sensor (see Sec. 3.2.3).

3.2.3 Sensor System

To utilize the serial elasticity between harmonic drive and human joint as a torque sensor, each actuated joint was equipped with two high-resolution encoders. The first encoder (MILE Encoder, Maxon Motor AG, Sachseln, Switzerland) is integrated into the primary motor M1 of the hip and knee VSA $\varphi_{\mathrm{M1,H/K}}$. The second encoder (Orbis true absolute rotary encoder, RLS, Komenda, Slovenia) is placed at the output shaft of both MeRIAs $\varphi_{\mathrm{exo,H/K}}$. The interaction torque $\tau_{\mathrm{exo,H/K}}$ between the exoskeleton and the human hip or knee joint is linearly dependent on the deflection angle and the elasticity $\sigma_{\mathrm{H/K}}(l)$ of the leaf springs according to Hooke's law:

$$\begin{bmatrix} \tau_{\mathrm{exo,H}} \\ \tau_{\mathrm{exo,K}} \end{bmatrix} = \begin{bmatrix} \sigma_{\mathrm{H}}(l_{\mathrm{H}}) \cdot \left(\frac{\varphi_{\mathrm{M1,H}}}{\gamma_{1,\mathrm{H}}} - \varphi_{\mathrm{exo,H}} \right) \\ \sigma_{\mathrm{K}}(l_{\mathrm{K}}) \cdot \left(\frac{\varphi_{\mathrm{M1,K}}}{\gamma_{1,\mathrm{K}}} - \varphi_{\mathrm{exo,K}} \right) \end{bmatrix}. \tag{3.1}$$

The coupling elasticity $\sigma_{\mathrm{H/K}}$ is dependent on the effective length $l_{\mathrm{H/K}}$ of the leaf springs. The relationship between effective length and elasticity was measured in a test bench [LLM18] equipped with a torque sensor (DR-2477, Lorenz Sensors, Alfdorf, Germany). Afterwards, the relation could be approximated by a second-order regression as shown in Fig. 3.2b. The different stiffness ranges between the knee and hip actuator are due to broader leaf springs in the hip actuator to allow for higher torques for hip joint support. The exact values for the maximum and minimum elasticity of the two different VSAs are provided in Tab. 3.2. The stiffness values of the MeRIA are in the mid-range of the systems presented in Tab. 3.1.

Table 3.2: Actuator and torque measurement specifications. (© 2022 IEEE)

	Parameter	Hip	Knee	Unit
Motor Power		150	150	W
Nominal Output Torque		64.2	40.1	N m
Weight		2.2	2.1	kg
Max. Stiffness	$\bar{\sigma}$	515	408	$\frac{\text{N m}}{\text{rad}}$
Min. Stiffness	$\underline{\sigma}$	265	196	
Time from high to low Stiffness	Δt	0.8	1.75	s
Min. Resolution at max. Stiffness	$\Delta\tau(\bar{\sigma})$	0.202	0.160	N m
Min. Resolution at min. Stiffness	$\Delta\tau(\underline{\sigma})$	0.102	0.076	N m
Gear Ratio M1	γ_1	1:160	1:100	-
Back Electromotive Force Constant	$K_{\text{emf,M1}}$	0.0525	0.0525	$\frac{\text{N m}}{\text{A}}$
Motor and Gear Inertia	J_{M1}	$3.46 \cdot 10^{-4}$	$3.46 \cdot 10^{-4}$	kg m^2
Bearing Resistance	B_{M1}	0.00391	0.00391	$\frac{\text{N m s}}{\text{rad}}$
Proportional Gain Velocity Ctr.	K_P	0.81	0.81	$\frac{\text{A s}}{\text{rad}}$
Integral Gain Velocity Ctr.	K_I	17	17	$\frac{\text{A}}{\text{rad}}$

The resolution of the torque measurement based on the spring deflection can be determined by the resolution of the encoders on the input and output sides and is provided in Tab. 3.2.

Furthermore, the exoskeleton is equipped with four *force sensing resistors* (FSRs) in each sole of the shoes to estimate the *ground reaction force* (GRF), as proposed in [PLB+21]. One FSR is placed underneath the heel, and three more are placed in the front part of the foot (inside, outside, and under the big toe, see Fig. 3.1). A calibration method was developed to account for the fact that the in-sole FSR sensors cover only a fraction of the subject's foot surface. The method averages the data from the rear and the three front FSRs for 5 s and calibrates them to the subject's body weight while they stand on their rear and front foot, respectively. In addition to the FSRs and angle sensors, *inertial measurement units* (IMUs) were attached to the exoskeleton's thighs to determine the orientation of the legs in space. All sensors were sampled by an individual microcontroller and the corresponding measurement signals sent via a *controller area network* (CAN) to the real-time computer at a sample rate of 1 kHz (except for the IMU, which was updated at 100 Hz).

3.2.4 Actuation Model

Following the system description in [LLM16], the dynamical equation for M1 of the actuator is given as

$$\frac{d\dot{\varphi}_{\mathrm{M1}}}{dt} = \frac{K_{\mathrm{emf,M1}} \cdot I_{\mathrm{M1}}}{J_{\mathrm{M1}}} - \frac{B_{\mathrm{M1}} \cdot \dot{\varphi}_{\mathrm{M1}}}{J_{\mathrm{M1}}} - \frac{\sigma(l) \cdot \varphi_{\mathrm{M1}}}{J_{\mathrm{M1}} \cdot \gamma_1^2}, \tag{3.2}$$

where $K_{\mathrm{emf,M1}}$ is the back electromotive force constant of M1, B_{M1} is the bearing resistance coefficient of M1, J_{M1} is the total inertia of M1, and γ_1 is the transmission coefficient of the harmonic drive. Note that the additional index for the joints H/K in eq. (3.2) and in the following equations is omitted for readability reasons. The actuators' parameters were identified using grey box modeling. The transmission gear and back electromotive force constant were directly taken from the datasheet and the bearing resistance and inertia were derived via least squares estimation (see Sec. 2.3.2). The identified parameters are given in Tab. 3.2.

To analyze the interaction between the actuator and the exoskeleton, it was assumed that the output side of the motor is fixed implying that the joints of the exoskeleton $\varphi = \dot{\varphi} = 0$ remain in the same position and movement can only occur through the deflection of the leaf springs. In this case, the output torque (3.1) simplifies to:

$$\tau_{\mathrm{exo}} = \sigma(l) \cdot \frac{\varphi_{\mathrm{M1}}}{\gamma_1}. \tag{3.3}$$

Note that in eq. (3.3) and in the following the differentiation between hip and knee actuator is omitted for readability. Secondly, the dynamics of the MeRIA were extended with a velocity controller $K_{\mathrm{PI}}(s)$ with proportional and integral action. The control law is given as

$$I_{\mathrm{M1}} = (\dot{\varphi}_{\mathrm{M1,ref}} - \dot{\varphi}_{\mathrm{M1}}) K_{\mathrm{PI}}(s), \tag{3.4}$$

where $\varphi_{\mathrm{M1,ref}}$ is the reference velocity and

$$K_{\mathrm{PI}}(s) = K_P + \frac{K_I}{s}. \tag{3.5}$$

By substituting eq. (3.5) into eq. (3.4), the input current I_{M1} can be reformulated as:

$$I_{\mathrm{M1}} = K_P \cdot \dot{\varphi}_{\mathrm{M1,ref}} + K_I \cdot \varphi_{\mathrm{M1,ref}} - K_P \cdot \dot{\varphi}_{\mathrm{M1}} - K_I \cdot \varphi_{\mathrm{M1}} \ . \tag{3.6}$$

By substituting eq. (3.6) into eq. (3.2) and assuming the fixed output side (eq. (3.3)), the dynamic behavior of $\dot{\varphi}_{\mathrm{M1}}$ (including the PI controller) is obtained:

$$\frac{d\dot{\varphi}_{\mathrm{M1}}}{dt} = t_1 \cdot \dot{\varphi}_{\mathrm{M1,ref}} + t_2 \cdot \varphi_{\mathrm{M1,ref}} + t_3 \cdot \dot{\varphi}_{\mathrm{M1}} + t_4 \cdot \varphi_{\mathrm{M1}}, \tag{3.7}$$

where

$$\begin{aligned} t_1 &= \frac{K_P \cdot K_{\mathrm{emf,M1}}}{J_{M1}}, & t_2 &= \frac{K_I \cdot K_{\mathrm{emf,M1}}}{J_{M1}} \\ t_3 &= -\frac{K_P \cdot K_{\mathrm{emf,M1}} + B_{M1}}{J_{M1}}, & t_4(\sigma) &= -\frac{K_I \cdot K_{\mathrm{emf,M1}} \cdot \gamma_1^2 + \sigma(l)}{J_{M1} \cdot \gamma_1^2}. \end{aligned} \tag{3.8}$$

The coupled torque between the motor M1 and M2, which is caused by the change of the deflection angle when adjusting the effective length l, can be neglected, see e.g. [Jaf14]. Thus, a fully decoupled model between joint torque assistance and stiffness variation is obtained.
For this reason, the dynamic model of M2 is not considered in the following control design of the output torque. Instead, the online changeable and measurable stiffness $\sigma(t)$ is treated as an exogenous input. Consequently, the differential equations in eq. (3.7) can be rewritten as an *linear parameter varying* (LPV) model in state-space form:

$$\begin{aligned} \dot{\boldsymbol{x}} &= \boldsymbol{A}(\boldsymbol{\sigma}(t))\boldsymbol{x} + \boldsymbol{B}(\boldsymbol{\sigma}(t))u, \\ y &= \boldsymbol{C}(\boldsymbol{\sigma}(t))\boldsymbol{x} + D(\boldsymbol{\sigma}(t))u. \end{aligned} \tag{3.9}$$

Defining the output $y = \tau_{\mathrm{exo}}$ and the input $u = \dot{\varphi}_{\mathrm{M1,ref}}$, the state-space matrices of eq. (3.9) in observable canonical form are given by

$$\begin{aligned} \boldsymbol{x} &= \begin{bmatrix} t_2 \frac{\sigma}{\gamma_1} \varphi_{\mathrm{M1,ref}} \\ \dot{\tau}_{\mathrm{exo}} - t_3 \tau_{\mathrm{exo}} \\ \tau_{\mathrm{exo}} \end{bmatrix}, \quad \boldsymbol{A} = \begin{bmatrix} 0 & 0 & 0 \\ 1 & 0 & t_4(\sigma) \\ 0 & 1 & t_3 \end{bmatrix}, \\ \boldsymbol{B} &= \begin{bmatrix} t_2 \cdot \frac{\sigma}{\gamma_1} \\ t_1 \cdot \frac{\sigma}{\gamma_1} \end{bmatrix}, \qquad \boldsymbol{C} = \begin{bmatrix} 0 & 0 & 1 \end{bmatrix}, \qquad D = 0. \end{aligned} \tag{3.10}$$

The numerical values of the parameters of eq. (3.10) have been provided in Tab. 3.2.

3.2.5 Inner Loop Torque Control

The proposed control concept of the VSAs for the hip and knee joints consists of three cascaded loops as initially introduced in [LLM18]. The innermost control involves a current controller, which is calculated on the motor controller at a sampling frequency of 53.6 kHz. The dynamics of the current controller are assumed to be sufficiently fast in comparison to the dynamics of the mechanical system and are therefore neglected in the following. The second inner control regulates the velocity $\dot{\varphi}_{\mathrm{M1}}$ of M1 as described in the previous section and is updated with a sampling frequency of 1 kHz.

A third controller is required to provide the reference velocity for the PI-controller to control the interaction torque τ_{exo} between the VSA and the load.

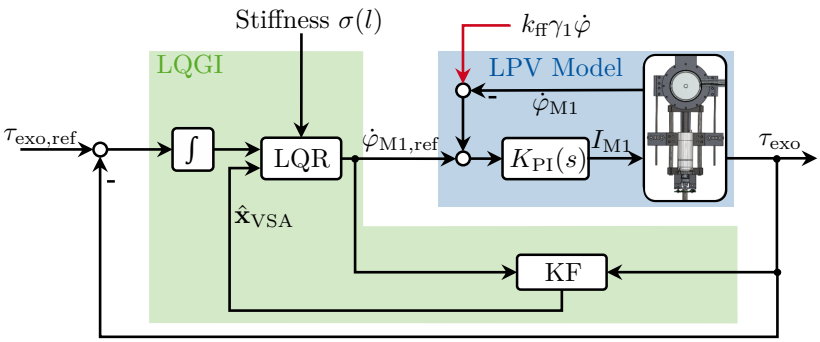

Figure 3.3: Torque control for hip and knee VSA consisting of a linear quadratic regulator with Kalman filter (KF) and integral behavior as proposed in [LLM18].

This controller was introduced in [LLM18] and is based on a *LQG controller with integral behavior* (LQGI) to prevent a steady state error (see Fig. 3.3). To design the LQGI controller, in [LLM18] the system in eq. (3.9) was first extended by an additional state containing the integral of the torque error. Then, the classical *linear quadratic regulator* (LQR) optimization problem was solved using the *algebraic riccati equation* (ARE) for the highest and lowest stiffness values of the hip and knee MeRIA. Lastly, the control parameters of the two derived controllers were interpolated based on the actuator's stiffness to obtain an optimal controller for every stiffness value. Additionally, a Kalman filter (KF) was used to estimate the inner state vector $\hat{\mathbf{x}}_{\mathrm{VSA}}$ required for the LQG controller.

One drawback of the designed LQG method is that the change in velocity is not taken into account due to the fixed load assumption in Sec. 3.2.4, which leads to performance losses when the load is movable. Therefore, in this thesis, an extension to this control scheme is introduced. It consists of an additional feed-forward (FF) term based on the angular velocity of the joint $\dot{\varphi}$, the transmission ratio of the harmonic drive γ_1, and a FF gain $k_{\mathrm{ff}} \in (0, 1)$ (see red arrow in Fig. 3.3). Notably, the proposed feed-forward term takes into account the influences of the swinging mass in the free-output case and achieves a shorter rising time of the step response resulting in a similar performance as in the fixed load case presented in [LLM18]. The entire torque control was implemented on a real-time computer with a sampling frequency of 1 kHz (MicroAutoBox II, dSpace, Paderborn, Germany).

3.2.6 Walking Trial with the Exoskeleton

Setting the reference torque $\tau_{\text{exo,ref}}$ to zero for the hip and knee joint VSA allows the exoskeleton to follow the human gait. To show this, a healthy subject (male, 27 years, 62 kg, 181 cm) walked with the exoskeleton on a treadmill at a speed of 1 km/h. The experimental protocol was reviewed by RWTH Aachen University Hospital's ethics committee (EK353-19) without concerns. The GRF measured by the four in-sole FSRs (top), the joint angles (middle), and interaction torques (bottom) are depicted in Fig. 3.4. The stance and swing phase of the gait can be differentiated using a threshold on the GRF as shown by the grey (stance) and white (swing) areas in Fig. 3.4. The sum of the GRF data during gait matches the typical GRF curve consisting of two maxima at the beginning and at the end of the single stance phase with values higher than the body weight [BMA15]. Note that the interaction torque between the subject and the exoskeleton remained in a 2 N m wide band (see Fig. 3.4). In comparison, Bortole et al. and Veneman et al. achieved maximum torques of ±4 N m and ±1 N m, respectively, for the zero torque tracking [BDR+13, VKH+07] which at that time were considered as low frictions not influencing the patient's gait.

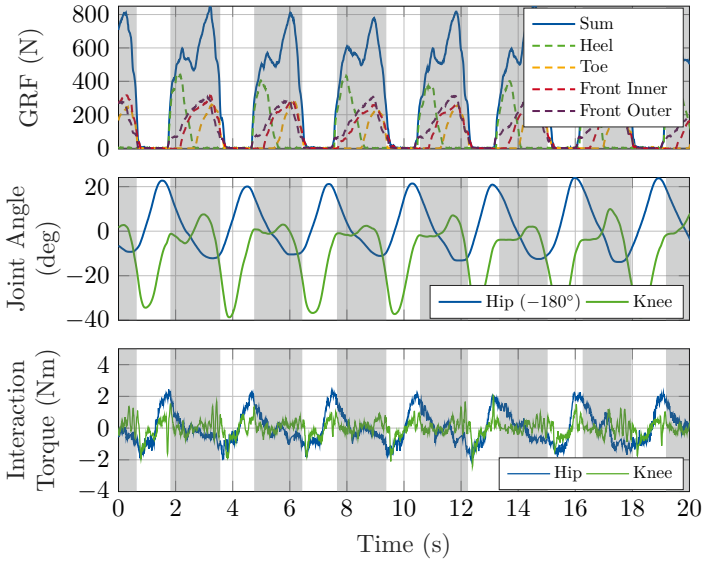

Figure 3.4: Insole FSRs measurement, angles and interaction torque of hip and knee joint during zero-torque controlled gait (1 km/h). The swing phase is highlighted in white and the stance phase in grey. (© 2022 IEEE)

The implemented torque controller enables various opportunities to provide assistance for the test subject. For example, by cascading the LQGI controller with a PD position control, an impedance controller can be realized to guide the subject within a specific gait trajectory as described in Sec. 2.2.4. In this chapter, however, the focus lies on the detection of human movement intention, which is why the torque control is mainly used for excitation trials, as shown in Sec. 3.3.

3.3 System and Subject Modeling

Within this thesis, a new approach to obtain the subject's movement intention is presented. The idea of the approach is based on estimating the direction and amplitude of the subject's joint torque. At first, the focus lies on the swing phase of the gait as it is the more challenging phase in terms of high dynamics. For this, a dynamical model is derived to describe the exoskeleton-human system. The estimation of the human joint torque in the swing phase was then conducted by applying an UKF. Secondly, a static model is presented to estimate the human torque during the gait's stance phase.

3.3.1 Exoskeleton Modeling in Swing Phase

The swing phase of the unilateral exoskeleton, the subject's leg, and the combined system were modeled using the Euler-Lagrange formalism. As a simplification, the exoskeleton and the leg of the subject were considered as driven double pendulums. These double pendulums can be described individually but also as a fixed coupled system. The coupled system is actuated by the torque provided through the actuator and the human's joint torque, which is a superposition of the active muscle torque and the passive elastic torque. In this thesis, the focus was on estimating the superimposed human's joint torque; however, the active muscle torque can be obtained by applying the double-exponential equations for estimating the passive elastic torque derived by Riener et al. [RE99]. A further simplification was made by neglecting the influence of the varying ankle angle. This simplification seems acceptable because the angle only changes slightly during the swing phase. Hence, its impact on the knee and hip is negligible. In general, the double pendulum model has been widely used in exoskeleton control and yielded good performance [GSK06].

First, the joint angles and model parameters need to be defined as shown in Fig. 3.5. In particular, for the model, the hip φ_{H} and knee φ_{K} angles are required. The resting position is achieved at $\varphi_{\mathrm{K}} = 0$, $\varphi_{\mathrm{H}} = \pi$, and an upright posture of the torso with $\varphi_{\mathrm{To}} = 0$. Additional parameters are the point mass m_{T}, location (x_{T}, y_{T}), inertia J_{T} and length l_{T} of the thigh. Parameters of the

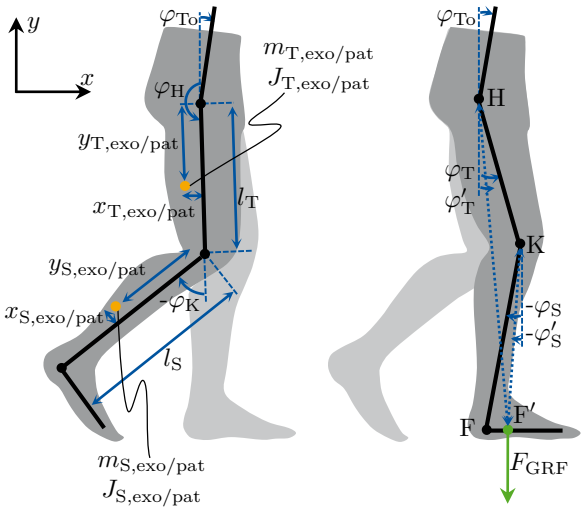

Figure 3.5: Reference frames (black), lengths and angles (blue), masses (orange), and forces (green) to describe the swing (left) and stance phase (right). (© 2023 IEEE)

shank are indicated by the index 'S' instead of 'T'. The index 'exo' in Fig. 3.5 refers to the exoskeleton while the index 'pat' refers to the pendulum of the healthy subject or the patient.

To describe the dynamical behavior based on the Euler-Lagrangian formalism, first the Lagrangian $\mathcal{L}$ is derived, which is given by the difference between the kinetic energy $E_{\mathrm{kin}} = T$ and the potential energy $E_{\mathrm{pot}} = V$ in the system:

$$\mathcal{L} = E_{\mathrm{kin}} - E_{\mathrm{pot}} = T - V. \tag{3.11}$$

The kinetic energy consists of two parts: the energy of the translational and the rotational motion. The translational velocity of the point masses for the thigh and the shank to describe the kinetic energy are represented by $\mathbf{v}_{\mathrm{T}}$ and $\mathbf{v}_{\mathrm{S}}$ in the observer reference frame:

$$\mathbf{v}_{\mathrm{T}} = \dot{\varphi}_{\mathrm{H}} \begin{bmatrix} -y_{\mathrm{T}} \cos(\varphi_{\mathrm{To}} + \varphi_{\mathrm{H}}) - x_{\mathrm{T}} \sin(\varphi_{\mathrm{To}} + \varphi_{\mathrm{H}}) \\ y_{\mathrm{T}} \sin(\varphi_{\mathrm{To}} + \varphi_{\mathrm{H}}) - x_{\mathrm{T}} \cos(\varphi_{\mathrm{To}} + \varphi_{\mathrm{H}}) \end{bmatrix} \tag{3.12}$$

$$\begin{aligned}\mathbf{v}_\mathrm{S} = \dot{\varphi}_\mathrm{H} \begin{bmatrix} -l_\mathrm{T}\cos(\varphi_\mathrm{To}+\varphi_\mathrm{H}) \\ l_\mathrm{T}\sin(\varphi_\mathrm{To}+\varphi_\mathrm{H}) \end{bmatrix} + (\dot{\varphi}_\mathrm{H}+\dot{\varphi}_\mathrm{K})\cdot \\ \begin{bmatrix} -y_\mathrm{S}\cos(\varphi_\mathrm{To}+\varphi_\mathrm{H}+\varphi_\mathrm{K}) - x_\mathrm{S}\sin(\varphi_\mathrm{To}+\varphi_\mathrm{H}+\varphi_\mathrm{K}) \\ y_\mathrm{S}\sin(\varphi_\mathrm{To}+\varphi_\mathrm{H}+\varphi_\mathrm{K}) - x_\mathrm{S}\cos(\varphi_\mathrm{To}+\varphi_\mathrm{H}+\varphi_\mathrm{K}) \end{bmatrix}\end{aligned} \tag{3.13}$$

Note that the observer reference frame is moving with the user's torso. Thus, the kinetic energy induced by the torso's movement is neglected in eqs. (3.12) and (3.13) therefore only holds for slow torso movements. Given the translational velocity of the point masses and the moments of inertia J_T and J_S for the shank and the thigh, the kinetic energy of the double pendulum can be described by:

$$\begin{aligned}E_\mathrm{kin} = T = \underbrace{\frac{1}{2} m_\mathrm{T} \mathbf{v}_\mathrm{T}^T \mathbf{v}_\mathrm{T}}_{\text{Translation Thigh}} + \underbrace{\frac{1}{2} m_\mathrm{S} \mathbf{v}_\mathrm{S}^T \mathbf{v}_\mathrm{S}}_{\text{Translation Shank}} \\ + \underbrace{\frac{1}{2} \mathbf{J}_T (\dot{\varphi}_\mathrm{H})^2}_{\text{Rotation Thigh}} + \underbrace{\frac{1}{2} \mathbf{J}_S (\dot{\varphi}_\mathrm{H}+\dot{\varphi}_\mathrm{K})^2}_{\text{Rotation Shank}}.\end{aligned} \tag{3.14}$$

The potential energy V results from gravitation and can be derived from the deviation of the pendulum from the resting position:

$$\begin{aligned}E_\mathrm{pot} = V = \underbrace{g m_\mathrm{T} y_\mathrm{T} \cos(\varphi_\mathrm{To}+\varphi_\mathrm{H})}_{\text{Thigh}} \\ + \underbrace{g m_\mathrm{S} \left(l_\mathrm{T}\cos(\varphi_\mathrm{To}+\varphi_\mathrm{H}) + y_\mathrm{S}\cos(\varphi_\mathrm{To}+\varphi_\mathrm{H}+\varphi_\mathrm{K}) \right)}_{\text{Shank}}.\end{aligned} \tag{3.15}$$

Given the Lagrangian, the Euler-Lagrange-formalism can be applied in the next step:

$$\frac{d}{dt}\frac{\partial \mathcal{L}}{\partial \dot{\mathbf{q}}} - \frac{\partial \mathcal{L}}{\partial \mathbf{q}} = \mathbf{Q_e} \tag{3.16}$$

with $\mathbf{q} = (\varphi_\mathrm{H}, \varphi_\mathrm{K})^T$ and $\mathbf{Q_e}$ being the external torques of the double pendulum's equations of motion. The external torques $\mathbf{Q}_e$ consist of the friction, the actuation, and the human's joint torques. With the joint torques τ_H and τ_K and the assumption of linear friction at the joints with the friction parameters d_H and d_K, the external torques are given by:

$$\mathbf{Q}_e = \begin{bmatrix} \tau_\mathrm{H} - d_\mathrm{H}\varphi_\mathrm{H} & \tau_\mathrm{K} - d_\mathrm{K}\varphi_\mathrm{K} \end{bmatrix}^T. \tag{3.17}$$

Solving the left side of the Euler-Lagrange-Formalism in eq. (3.16) and combining this with the external torques from eq. (3.17) results in two second-order, non-

linear system equations for the hip and the knee:

$$\begin{aligned}
&\tau_\mathrm{H} - d_\mathrm{H}\dot{\varphi}_\mathrm{H} = \ddot{\varphi}_\mathrm{H}(J_\mathrm{T} + J_\mathrm{S} + m_\mathrm{T}(x_\mathrm{T}^2 + y_\mathrm{T}^2) \\
&+ m_\mathrm{S}(x_\mathrm{S}^2 + y_\mathrm{S}^2 + l_\mathrm{T}^2 + 2l_\mathrm{T}(y_\mathrm{S}\cos(\varphi_\mathrm{K}) + x_\mathrm{S}\sin(\varphi_\mathrm{K})))) \\
&+ \ddot{\varphi}_\mathrm{K}(J_\mathrm{S} + m_\mathrm{S}(x_\mathrm{S}^2 + y_\mathrm{S}^2 + y_\mathrm{S}l_\mathrm{T}\cos(\varphi_\mathrm{K}) + x_\mathrm{S}l_\mathrm{T}\sin(\varphi_\mathrm{K}))) \\
&+ (2\dot{\varphi}_\mathrm{H}\dot{\varphi}_\mathrm{K} + \dot{\varphi}_\mathrm{K}^2)(m_\mathrm{S}l_\mathrm{T}(x_\mathrm{S}\cos(\varphi_\mathrm{K}) - y_\mathrm{S}\sin(\varphi_\mathrm{K}))) \\
&+ gm_\mathrm{T}(x_\mathrm{T}\cos(\varphi_\mathrm{To} + \varphi_\mathrm{H}) - y_\mathrm{T}\sin(\varphi_\mathrm{To} + \varphi_\mathrm{H})) \\
&+ gm_\mathrm{S}(x_\mathrm{S}\cos(\varphi_\mathrm{To} + \varphi_\mathrm{H} + \varphi_\mathrm{K}) \\
&- y_\mathrm{S}\sin(\varphi_\mathrm{To} + \varphi_\mathrm{H} + \varphi_\mathrm{K}) - l_\mathrm{T}\sin(\varphi_\mathrm{To} + \varphi_\mathrm{H}))
\end{aligned} \tag{3.18}$$

$$\begin{aligned}
&\tau_\mathrm{K} - d_\mathrm{K}\dot{\varphi}_\mathrm{K} = \ddot{\varphi}_\mathrm{K} \cdot (J_\mathrm{S} + m_\mathrm{S}(x_\mathrm{S}^2 + y_\mathrm{S}^2)) \\
&+ \ddot{\varphi}_\mathrm{H} \cdot (J_\mathrm{S} + m_\mathrm{S}(x_\mathrm{S}^2 + y_\mathrm{S}^2 + y_\mathrm{S}l_\mathrm{T}cos(\varphi_\mathrm{K}) + x_\mathrm{S}l_\mathrm{T}sin(\varphi_\mathrm{K}))) \\
&+ \dot{\varphi}_\mathrm{H}^2 m_\mathrm{S}l_\mathrm{T} \cdot (x_\mathrm{S}\cos(\varphi_\mathrm{K}) - y_\mathrm{S}\sin(\varphi_\mathrm{K})) \\
&+ gm_\mathrm{S}(\cos(\varphi_\mathrm{To} + \varphi_\mathrm{H}) \cdot (x_\mathrm{S}\cos(\varphi_\mathrm{K}) - y_\mathrm{S}\sin(\varphi_\mathrm{K})) \\
&- \sin(\varphi_\mathrm{To} + \varphi_\mathrm{H}) \cdot (y_\mathrm{S}\cos(\varphi_\mathrm{K}) + x_\mathrm{S}\sin(\varphi_\mathrm{K}))).
\end{aligned} \tag{3.19}$$

By defining an auxiliary matrix $\mathbf{A}$ and the coordinate vector $\boldsymbol{q} = \begin{bmatrix}\varphi_\mathrm{H} & \varphi_\mathrm{K}\end{bmatrix}^T$, the system equations can be written in a more compact way [YGZG17]:

$$\mathbf{A}(\dot{\mathbf{q}}, \mathbf{q}, t) = \frac{\partial E_\mathrm{kin}}{\partial \dot{\mathbf{q}}},\ \mathbf{M}(\dot{\mathbf{q}}, \mathbf{q}, t) = \frac{\partial \mathbf{A}}{\partial \dot{\mathbf{q}}}, \tag{3.20}$$

$$\mathbf{C}(\dot{\mathbf{q}}, \mathbf{q}, t) = \frac{\partial \mathbf{A}}{\partial \mathbf{q}}\frac{d\mathbf{q}}{dt} + \frac{\partial \mathbf{A}}{\partial t} - \frac{\partial E_\mathrm{kin}}{\partial \mathbf{q}}, \tag{3.21}$$

$$\mathbf{G}(\mathbf{q}) = \frac{\partial E_\mathrm{pot}}{\partial \mathbf{q}}. \tag{3.22}$$

With the torque vector $\boldsymbol{\tau} = (\tau_\mathrm{H}, \tau_\mathrm{K})^T$ and the damping matrix $\mathbf{D} = \mathrm{diag}(d_\mathrm{H}, d_\mathrm{K})$, the resulting double pendulum equation is:

$$\boldsymbol{\tau} = \mathbf{M}(\dot{\mathbf{q}}, \mathbf{q}, t)\ddot{\mathbf{q}} + \mathbf{C}(\dot{\mathbf{q}}, \mathbf{q}, t) + \mathbf{D}\dot{\mathbf{q}} + \mathbf{G}(\mathbf{q}). \tag{3.23}$$

For a more detailed derivation, see [YGZG17]. The system equation given in eq. (3.23) describes the dynamic behavior of the exoskeleton's frame. By changing the system's parameters, the same model can be used to describe the dynamics of the subject's leg. Additionally, it can be extended by other joints by additional rows in the coordinate vector $\mathbf{q}$ and torque vector $\boldsymbol{\tau}$. However, in this case the focus is on the two DoF case with additional consideration of the upper body posture φ_To as given in eqs. (3.18) and (3.19).

The combination of the human-exoskeleton system can be obtained by assuming a fixed coupling between the two double pendulums such that the joint angles of the two pendulums align. In the real system, the angles may differ because the connection between the exoskeleton and the human subject is not ideal [NJR+18], but this assumption is made to achieve a reasonably uncomplicated model, thereby following the paradigm *As simple as possible, as complex as necessary* described in Sec. 2.3.1. Hence, the complete system is a superposition of the two pendulums given by

$$\begin{aligned}\begin{bmatrix}\tau_{\mathrm{H,pat}}\\ \tau_{\mathrm{K,pat}}\end{bmatrix}+\begin{bmatrix}\tau_{\mathrm{H,exo}}\\ \tau_{\mathrm{K,exo}}\end{bmatrix} =&(\mathbf{M}_{\mathrm{exo}}(\dot{\mathbf{q}},\mathbf{q},t)+\mathbf{M}_{\mathrm{pat}}(\dot{\mathbf{q}},\mathbf{q},t))\ddot{\mathbf{q}}\\ &+\mathbf{C}_{\mathrm{exo}}(\dot{\mathbf{q}},\mathbf{q},t)+\mathbf{C}_{\mathrm{pat}}(\dot{\mathbf{q}},\mathbf{q},t)\\ &+(\mathbf{D}_{\mathrm{exo}}+\mathbf{D}_{\mathrm{pat}})\dot{\mathbf{q}}+\mathbf{G}_{\mathrm{exo}}(\mathbf{q})+\mathbf{G}_{\mathrm{pat}}(\mathbf{q}).\end{aligned} \tag{3.24}$$

3.3.2 Stance Phase Model

The stance phase differs significantly from the swing phase of the leg due to the forces between the foot and the ground. As a result, static forces have the greatest influence on the total torque in the subject's joints during the stance phase. Meanwhile, dynamic forces resulting from the forward motion of the gait play a minor role. To obtain a sufficiently accurate estimate of the hip and knee torque in the stance phase, a static model is suggested. In contrast to the dynamic model of the swing phase, the static model of the stance phase requires only an algebraic rather than a differential equation, as the GRFs are directly measurable using FSRs.
The following derivation refers to the lengths and angles given in the right model of Fig. 3.5. Note that the stance phase model uses body segment angles instead of joint angles. They describe the angular position of the thigh (T) and shank (S) in space. The force acting on the knee joint in the perpendicular direction to the straight line $\overline{\mathrm{F'K}}$ is given by:

$$F_{\mathrm{K},\perp}=(F_{\mathrm{GRF}}-g(\underbrace{m_{\mathrm{S,exo}}+m_{\mathrm{S,pat}}}_{:=m_{\mathrm{S}}^{\star}}))\sin(\varphi_{\mathrm{S}}'). \tag{3.25}$$

This results in a static torque at the knee joint of

$$\begin{aligned}\tau_{\mathrm{K}}&=l_{\overline{\mathrm{F'K}}}\cdot F_{\mathrm{K},\perp}\\ &=l_{\overline{\mathrm{F'K}}}\sin(\varphi_{\mathrm{S}}')(F_{\mathrm{GRF}}-gm_{\mathrm{S}}^{\star}).\end{aligned} \tag{3.26}$$

The angle φ_{S}' is not directly measurable from the available sensors. To obtain eq. (3.26) as a function of φ_{S}, the difference between the projection from the

knee (Point K) joint to the center of the GRFs (Point F') $l_{\overline{\mathrm{F'K}}}\sin(\varphi'_{\mathrm{S}})$ and the projection from the knee joint to the ankle joint directly (Point F) $l_{\mathrm{S}}\sin(\varphi_{\mathrm{S}})$ need to be considered first. The difference is given by the length between F and F′. That is

$$l_{\overline{\mathrm{F'K}}}\sin(\varphi'_{\mathrm{S}}) = l_{\mathrm{S}}\sin(\varphi_{\mathrm{S}}) + l_{\overline{\mathrm{FF'}}}\ . \tag{3.27}$$

The distance $l_{\overline{\mathrm{FF'}}}$ can also be obtained by comparing the GRF measurement on the forefoot with that on the heel. The relation is given by

$$l_{\overline{\mathrm{FF'}}} = l_{\mathrm{F}}\frac{F_{\mathrm{Forefoot}}}{F_{\mathrm{Forefoot}} + F_{\mathrm{Heel}}} \qquad \text{if,} \qquad F_{\mathrm{Forefoot}} + F_{\mathrm{Heel}} > 0\ , \tag{3.28}$$

where $l_{\mathrm{F}} = 0.159\,\mathrm{cm}$ is the distance between GRF sensors of the heel and the hip in the designed setup. As a result, the total knee torque can be obtained by

$$\tau_{\mathrm{K}} = \left(l_{\mathrm{S}}\sin(\varphi_{\mathrm{S}}) + l_{\mathrm{F}}\frac{F_{\mathrm{Forefoot}}}{F_{\mathrm{Forefoot}} + F_{\mathrm{Heel}}}\right)\cdot(F_{\mathrm{GRF}} - gm^{\star}_{\mathrm{S}})\ . \tag{3.29}$$

Similarly, the total torque acting on the hip joint can be derived. It can be calculated by multiplying the force that is perpendicular to the straight line $\overline{\mathrm{F'H}}$ with the length $l_{\overline{\mathrm{F'H}}}$:

$$\begin{aligned}\tau_H =& F_{\mathrm{H},\perp}\cdot l_{\overline{\mathrm{F'H}}}\\ =& l_{\overline{\mathrm{F'H}}}\sin(\varphi'_{\mathrm{T}})(F_{\mathrm{GRF}}\\ &- g(\underbrace{m_{\mathrm{T,exo}} + m_{\mathrm{T,pat}} + m_{\mathrm{S,exo}} + m_{\mathrm{S,pat}}}_{:=m^{\star}_{\mathrm{TS}}}))\ .\end{aligned} \tag{3.30}$$

Using the relation of the length difference

$$l_{\overline{\mathrm{F'H}}}\sin(\varphi'_{\mathrm{T}}) = l_{\overline{\mathrm{F'K}}}\sin(\varphi'_{\mathrm{S}}) + l_{\mathrm{T}}\sin(\varphi_{\mathrm{T}}) \tag{3.31}$$

and eq. (3.27), the total hip joint torque amounts to

$$\begin{aligned}\tau_{\mathrm{H}} = &\left(l_{\mathrm{S}}\sin(\varphi_{\mathrm{S}}) + l_{\mathrm{T}}\sin(\varphi_{\mathrm{T}}) + l_{\mathrm{F}}\frac{F_{\mathrm{Forefoot}}}{F_{\mathrm{Forefoot}} + F_{\mathrm{Heel}}}\right)\\ &\cdot(F_{\mathrm{GRF}} - gm^{\star}_{\mathrm{TS}})\ .\end{aligned} \tag{3.32}$$

The derived eqs. (3.29) and (3.32) describe the superimposed knee and hip joint torque applied by the exoskeleton and the human. Since all quantities in these equations are directly measurable by the available sensors, it is possible - in contrast to the swing phase model - to directly estimate the human joint torque (denoted by $\hat{\tau}_{\mathrm{H,pat}}$ and $\hat{\tau}_{\mathrm{K,pat}}$) by subtracting the torque provided by the exoskeleton:

$$\begin{pmatrix}\hat{\tau}_{\mathrm{H,pat}}\\ \hat{\tau}_{\mathrm{K,pat}}\end{pmatrix} = \begin{pmatrix}\tau_{\mathrm{H}} - \tau_{\mathrm{H,exo}}\\ \tau_{\mathrm{K}} - \tau_{\mathrm{K,exo}}\end{pmatrix}. \tag{3.33}$$

These equations are valid for the single as well as for the double stance phase. However, the description of the joint torque in the stance phase using the GRF measurement and an algebraic equation has some disadvantages. Firstly, the GRF sensors are not capable of measuring lateral forces leading to model inaccuracies, especially at higher gait speeds. Secondly, the coupling between the test person and the exoskeleton is not ideal. Due to the fact that the knee joint acts as a rolling-sliding joint, the rotational axes of the exoskeleton knee and the human knee may get misaligned leading to inaccuracies in the torque estimation, especially when the leg is extended. The first mentioned disadvantage can be neglected because higher gait velocities can be excluded in the considered application case of rehabilitation. However, the latter must be accepted as a model inaccuracy for the sake of simplicity.

3.3.3 Parameter Estimation

Some parameters of the swing phase model in eqs. (3.19) and (3.18) and all parameters of the stance phase model in eqs. (3.32) and (3.29) can be quantified directly. These include the masses and lengths of the exoskeleton. According to [DSS19, p. 5], the mass of the subject's thigh and shank was assumed to be 12% and 7% of body weight, respectively (see Tab. 3.3). To identify the unknown parameters, i.e., inertia, the center of gravity, and friction of the double-pendulum model for the exoskeleton and the subject, an offline least squares parameter identification method was applied as introduced in Sec. 2.3.2. For the low-pass filter, the Parks-McClellan algorithm was used with frequency boundaries between 7.6 Hz and 10.1 Hz [MP05]. Least squares identification yields the best results if the noisiest signal is chosen as the result vector $\boldsymbol{y}$. Because the derivation amplifies the noise despite the low-pass filter, the second derivative $\ddot{\varphi}_{\mathrm{H/K}}$ was selected as the output for the least squares algorithm.

Directly determining the parameters by exciting the entire system with a single-step response is

1. not possible, because an underdetermined system of equations needs to be solved,

2. likely to result in inaccurate or non-physical results for lumped parameter estimation.

Therefore, the identification problem was divided into four sub-systems which all have the properties of a single pendulum to obtain the parameters subsequently. The four steps are

a Determine the knee/shank parameters of the exoskeleton ($d_{\mathrm{K,exo}}$, $J_{\mathrm{S,exo}}$, $x_{\mathrm{S,exo}}$, $y_{\mathrm{S,exo}}$) by applying torque steps to the knee joint only and keeping the hip angle $\varphi_{\mathrm{H}} = \pi$ and torso angle $\varphi_{\mathrm{To}} = 0$ constant. In this case, the eq. (3.19) reduces to:

$$\begin{aligned}\tau_{\mathrm{K}} = &\left(J_{\mathrm{S,exo}} + m_{\mathrm{S,exo}}(x_{\mathrm{S,exo}}^2 + y_{\mathrm{S,exo}}^2)\right)\ddot{\varphi}_{\mathrm{K}} + d_{\mathrm{K,exo}}\dot{\varphi}_{\mathrm{K}} \\ &+ gm_{\mathrm{S,exo}}\left(y_{\mathrm{S,exo}}\sin(\varphi_{\mathrm{K}}) - x_{\mathrm{S,exo}}\cos(\varphi_{\mathrm{K}})\right).\end{aligned} \tag{3.34}$$

The results of the parameter fitted model are shown in Fig. 3.6 (upper left).

b Determine the knee/shank parameters of the subject's knee joint ($d_{\mathrm{K,pat}}$, $J_{\mathrm{S,pat}}$, $x_{\mathrm{S,pat}}$, $y_{\mathrm{S,pat}}$) by applying torque steps to the knee joint only and using the parameters derived in step a. The second-order differential equation is similar to eq. (3.34) but extended by the inertia term of the healthy subject or the patient and the additional knee joint friction. The results of the model are shown in Fig. 3.6 (upper right).

c Determine the hip/thigh parameters of the exoskeleton ($d_{\mathrm{H,exo}}$, $J_{\mathrm{T,exo}}$, $x_{\mathrm{T,exo}}$, $y_{\mathrm{T,exo}}$) by keeping the knee angle constant $\varphi_{\mathrm{K}} = 0$ and using the parameters derived in step a. For this case, eq. (3.18) simplifies to:

$$\begin{aligned}\tau_{\mathrm{H}} = &(J_{\mathrm{T,exo}} + J_{\mathrm{S,exo}} + m_{\mathrm{T,exo}}(x_{\mathrm{T,exo}}^2 + y_{\mathrm{T,exo}}^2) \\ &+ m_{\mathrm{S,exo}}(x_{\mathrm{S,exo}}^2 + (y_{\mathrm{S,exo}} + l_{\mathrm{T,exo}})^2))\ddot{\varphi}_{\mathrm{H}} + d_{\mathrm{H,exo}}\dot{\varphi}_{\mathrm{H,exo}} \\ &+ gm_{\mathrm{T,exo}}(-y_{\mathrm{T,exo}}\sin(\varphi_{\mathrm{H}}) + x_{\mathrm{T,exo}}\cos(\varphi_{\mathrm{H}})) \\ &- gm_{\mathrm{S,exo}}((l_{\mathrm{T,exo}} + y_{\mathrm{S,exo}})\sin(\varphi_{\mathrm{H}}) - x_{\mathrm{S,exo}}\cos(\varphi_{\mathrm{H}})).\end{aligned} \tag{3.35}$$

and the result is shown in Fig. 3.6 (lower left).

d Determine the hip/thigh parameters of the subject's hip joint ($d_{\mathrm{H,pat}}$, $J_{\mathrm{T,pat}}$, $x_{\mathrm{T,pat}}$, $y_{\mathrm{T,pat}}$) by keeping the knee angle constant $\varphi_{\mathrm{K}} = 0$ and using the parameters derived in step a, b and c. The dynamical equation is similar to eq. (3.35) but with the additional term for the subject's thigh inertia and hip friction (see Fig. 3.6, lower right).

The actuator's stiffness was varied during each identification step in Fig. 3.6 from highest to lowest to account for the different torque measurement resolutions. The *root-mean-square error* (RMSE) between measured and simulated angle in Fig. 3.6 for all four cases can be calculated to $\mathrm{RMSE_a} = 3.31°$, $\mathrm{RMSE_b} = 3.51°$, $\mathrm{RMSE_c} = 2.38°$, and $\mathrm{RMSE_d} = 2.63°$. For validation, the same experiment but with 8 N m torque steps was conducted. In this case, the RMSEs were calculated

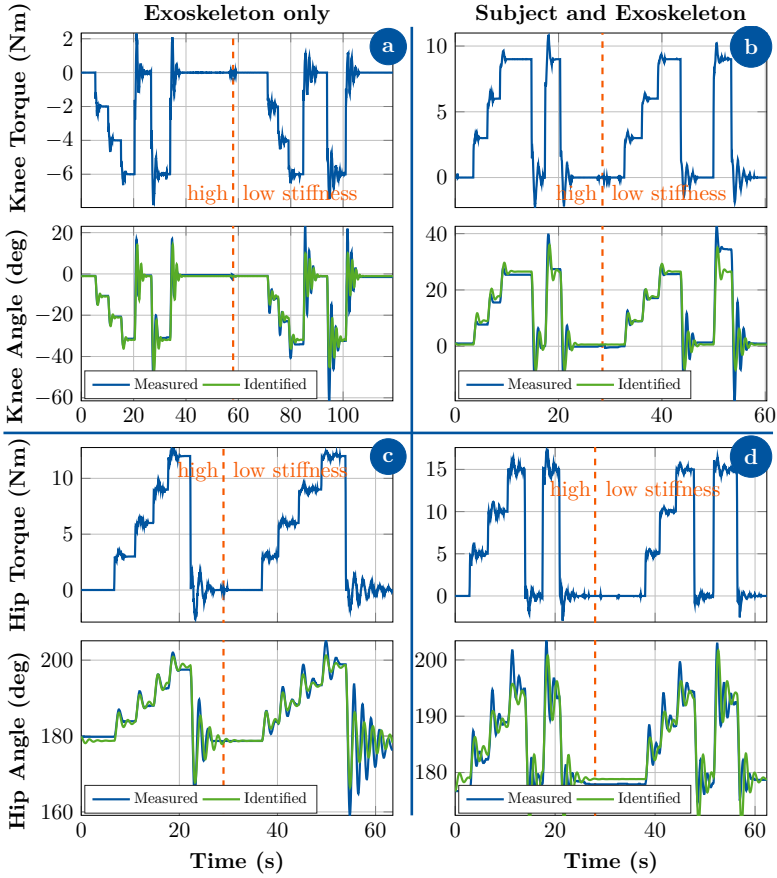

Figure 3.6: The identification process of the exoskeleton (left) and subject (right) parameters consists of four subsequently executed swing tests: Actuation of exoskeleton's knee joint (a, upper left), of the subject's knee joint with the exoskeleton (b, upper right), of the exoskeleton's hip joint (c, lower left), of the subject's hip joint with the exoskeleton (d, lower left). The system's input (upper graph) to the one DoF pendulums is the knee torque and the hip torque provided by the hip and the knee joint VSA, respectively. The measured angle (lower graph, blue) is regarded as the system's output. The simulation results with the identified parameters are shown in the lower graphs in green. (© 2022 IEEE)

to similar values given by $\mathrm{RMSE_a} = 3.45°$, $\mathrm{RMSE_b} = 3.26°$, $\mathrm{RMSE_c} = 2.45°$, and $\mathrm{RMSE_d} = 2.17°$, thus, verifying the good approximation of the model.

The identified optimal parameters, as listed in Tab. 3.3, are confined within the physically feasible range.

Table 3.3: Identified parameters of the double pendulum model. (© 2022 IEEE)

		Exoskeleton		Subject		
	Name	Parameter	Value	Parameter	Value	Unit
Knee/Shank	Inertia	$J_{\mathrm{S,exo}}$	0.0053	$J_{\mathrm{S,pat}}$	0.0604	$\mathrm{kg\,m^2}$
	Mass	$m_{\mathrm{S,exo}}$	2.5	$m_{\mathrm{S,pat}}$	4.34	kg
	CoM in x	$x_{\mathrm{S,exo}}$	0.001	$x_{\mathrm{S,pat}}$	0.005	m
	CoM in y	$y_{\mathrm{S,exo}}$	0.247	$y_{\mathrm{S,pat}}$	0.341	m
	Length	$l_{\mathrm{S,exo}}$	0.523	$l_{\mathrm{S,pat}}$	0.523	m
	Friction	$d_{\mathrm{K,exo}}$	1.176	$d_{\mathrm{K,pat}}$	1.714	$\frac{\mathrm{N\,m\,s}}{\mathrm{rad}}$
Hip/Thigh	Inertia	$J_{\mathrm{T,exo}}$	0.1604	$J_{\mathrm{T,pat}}$	0.296	$\mathrm{kg\,m^2}$
	Mass	$m_{\mathrm{T,exo}}$	4.4	$m_{\mathrm{T,pat}}$	7.44	kg
	CoM in x	$x_{\mathrm{T,exo}}$	-0.013	$x_{\mathrm{T,pat}}$	-0.012	m
	CoM in y	$y_{\mathrm{T,exo}}$	0.19	$y_{\mathrm{T,pat}}$	0.021	m
	Length	$l_{\mathrm{T,exo}}$	0.427	$l_{\mathrm{T,pat}}$	0.427	m
	Friction	$d_{\mathrm{H,exo}}$	2.805	$d_{\mathrm{H,pat}}$	4.089	$\frac{\mathrm{N\,m\,s}}{\mathrm{rad}}$

3.4 Model-based Human Movement Intention Estimation

One essential challenge in the patient-cooperative control of exoskeletons is determining the subject's movement intention. To obtain this information, the torque generated by the subject in the joints is estimated using a system theoretical approach. As described in Sec. 2.1.4, one approach to obtain this quantity is the calculation of the inverse dynamics using discrete differentiation of the joint angles. However, this comes at the cost of amplified noise or high time delays due to the second differentiation of the discrete angle encoder or its low-pass filtered signal. To avoid direct differentiation, a filter method estimating the subject's joint torque directly is proposed. Due to the nonlinearities in eqs. (3.18) and (3.19), a non-linear state estimation method, namely, the UKF (see Sec. 2.3.3) is suggested. The use of an *extended Kalman filter* (EKF) would also be possible. However, the UKF generally handles large nonlinearities better than the EKF [JU04].

3.4.1 Torque Estimation during Swing Phase

As described in Sec. 2.3.3, the UKF consists of a model-based prediction step and a measurement-based update step. Contrary to the *Kalman filter* (KF) and the EKF, the UKF uses the non-linear system model $\boldsymbol{f}(\boldsymbol{x}, \boldsymbol{u})$ to approximate a probability distribution from a given set of points instead of linearizing the system and calculating the Jacobian. This is achieved by applying the unscented transformation, which calculates the mean and covariance of nonlinearly transformed random variables. The UKF for estimating the subject's hip and knee joint was implemented in MATLAB/Simulink according to [JU04]. Here, the unscented transformation is used during the prediction and measurement steps of the KF to calculate the means and covariances. The states $\boldsymbol{x}$ of the system undergo a nonlinear state transition $\boldsymbol{f}(\boldsymbol{x}, \boldsymbol{u})$ while the mean $\bar{\boldsymbol{x}}$ and the covariance $\boldsymbol{\Sigma}_x$ of the states undergo the unscented transformation. This way, the a priori mean $\bar{\boldsymbol{x}}_k^-$ and covariance $\boldsymbol{\Sigma}_{x,k}^-$ are calculated. During the measurement step, the states undergo a second nonlinear transformation - the measurement function $\boldsymbol{h}(\boldsymbol{x}, \boldsymbol{u})$. Subsequently, the output sigma points, the a priori mean $\bar{\boldsymbol{y}}$ and auto-covariance $\boldsymbol{\Sigma}_{\bar{\boldsymbol{y}},\bar{\boldsymbol{y}}}$ and cross-covariance $\boldsymbol{\Sigma}_{\bar{\boldsymbol{x}},\bar{\boldsymbol{y}}}$ are calculated and, as a result, the Kalman-gain $\boldsymbol{K} = \boldsymbol{\Sigma}_{\bar{x},\bar{y}} \boldsymbol{\Sigma}_{\bar{y},\bar{y}}^{-1}$. With the Kalman-gain, the measurement update of the Kalman filter is performed.

One challenge in applying the UKF to the double pendulum for estimating the subject's joint torques is that the subject's joint torque is regarded as an input to the system. However, a UKF is only able to estimate internal states. Therefore, two additional states are introduced in the state equations of the double pendulum representing the angular acceleration of the joints due to the human joint torque. The inputs of these states are driven by a white noise process with zero mean w, because there is no prior information about the patient torque available. This approach aims to determine an angular acceleration caused by the known sources (exoskeleton torque) and then estimate the remaining acceleration required to achieve the measured movement of the coupled double pendulum. This remaining acceleration portion is then assigned to the acceleration produced by the subject and thus to its torque.

Fig. 3.7 visualizes the idea of the UKF for estimating the human's joint torques. The continuous state transition function of the UKF is derived from eq. (3.23). It has the joint angles $\mathbf{q} = \begin{bmatrix} \varphi_\mathrm{H} & \varphi_\mathrm{K} \end{bmatrix}^T$ and the joint velocities $\dot{\mathbf{q}} = \begin{bmatrix} \dot{\varphi}_\mathrm{H} & \dot{\varphi}_\mathrm{K} \end{bmatrix}^T$ as well as the patient torques $\boldsymbol{\tau}_\mathrm{pat} = \begin{bmatrix} \tau_\mathrm{H,pat} & \tau_\mathrm{K,pat} \end{bmatrix}^T$ as internal states and the exoskeleton torques $\boldsymbol{\tau}_\mathrm{exo} = \begin{bmatrix} \tau_\mathrm{H,exo} & \tau_\mathrm{K,exo} \end{bmatrix}^T$ and the

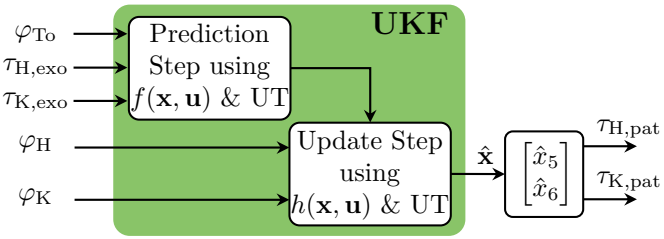

Figure 3.7: Block diagram of the Unscented Kalman Filter. (© 2022 IEEE)

torso angle φ_{To} as inputs:

$$\begin{aligned}\dot{\mathbf{x}} &= \begin{bmatrix} \dot{\varphi}_{\mathrm{H}} \\ \dot{\varphi}_{\mathrm{K}} \\ \ddot{\varphi}_{\mathrm{H}} \\ \ddot{\varphi}_{\mathrm{K}} \\ \dot{\tau}_{\mathrm{H,pat}} \\ \dot{\tau}_{\mathrm{K,pat}} \end{bmatrix} = \mathbf{f}(\mathbf{x},\mathbf{u}) + \mathbf{w} = \mathbf{f}\left(\begin{bmatrix} \varphi_{\mathrm{H}} \\ \varphi_{\mathrm{K}} \\ \dot{\varphi}_{\mathrm{H}} \\ \dot{\varphi}_{\mathrm{K}} \\ \tau_{\mathrm{H,pat}} \\ \tau_{\mathrm{K,pat}} \end{bmatrix}, \begin{bmatrix} \varphi_{\mathrm{To}} \\ \tau_{\mathrm{H,exo}} \\ \tau_{\mathrm{K,exo}} \end{bmatrix} \right) + \mathbf{w} \\ &= \begin{bmatrix} \begin{bmatrix} \dot{\varphi}_{\mathrm{H}} & \dot{\varphi}_{\mathrm{K}} \end{bmatrix}^T \\ \begin{bmatrix} ((\mathbf{M}_{\mathrm{exo}} + \mathbf{M}_{\mathrm{pat}})^{-1}(\boldsymbol{\tau}_{\mathrm{pat}} + \boldsymbol{\tau}_{\mathrm{exo}} + \mathbf{C}_{\mathrm{exo}} + ... \\ ...\mathbf{C}_{\mathrm{pat}} + (\mathbf{D}_{\mathrm{exo}} + \mathbf{D}_{\mathrm{pat}})\dot{\mathbf{q}} + \mathbf{G}_{\mathrm{exo}} + \mathbf{G}_{\mathrm{pat}})) \end{bmatrix} \\ \begin{bmatrix} 0 & 0 \end{bmatrix}^T \end{bmatrix} + \mathbf{w}. \end{aligned} \tag{3.36}$$

In the UKF, the internal model is discretized using explicit Euler integration with a sample time of $\Delta t = 1\,\mathrm{ms}$ for fast performance. The resulting discrete state transition function is:

$$\mathbf{x}(k+1) = \mathbf{f}(\mathbf{x}(k),\mathbf{u}(k)) \cdot \Delta t + \mathbf{x}(k) + \mathbf{w}(k). \tag{3.37}$$

The measurement function $\mathbf{h}$ is linear as the outputs of the system are the joint angles which are direct states of the UKF:

$$\mathbf{z}(k) = \mathbf{h}\left(\mathbf{u}(k) + \mathbf{v}(k)\right) = \begin{bmatrix} \varphi_{\mathrm{H}}(k) \\ \varphi_{\mathrm{K}}(k) \end{bmatrix} + \mathbf{v}(k). \tag{3.38}$$

The parameters $\mathbf{w}$ and $\mathbf{v}$ in eqs. (3.37) and (3.38) represent uncorrelated, zero-mean white Gaussian noise processes. The expected value of these Gaussian processes can be given by the corresponding covariance matrices $\mathbf{Q}$ and $\mathbf{R}$ and the Kronecker delta function δ_{ij} as follows:

$$E\left\{ \begin{pmatrix} \mathbf{w}_i \\ \mathbf{v}_i \end{pmatrix} \left(\mathbf{w}_j^T \mathbf{v}_j^T \right) \right\} = \begin{bmatrix} \mathbf{Q} & \mathbf{0} \\ \mathbf{0} & \mathbf{R} \end{bmatrix} \delta_{ij}. \tag{3.39}$$

The measurement covariance matrix can be derived from the resolution of the encoders for the measured joint angles. The variance of the measurement is equal to the squared mean error resulting from the sensor resolution. The resolution is 14-bit which means the maximum error is $e_{\max} = 2\pi/(2^{14}-1)/2$. The resulting errors are uniformly distributed between $-e_{\max}$ and $e_{\max}$. However, since there is an additional transmission delay due to the communication interfaces, a Gaussian distribution is assumed. For the width of the distribution density, it is assumed that 95% of all deviations are in the range of the quantization noise. Thus, the maximum error $e_{\max}$ is assumed to be two times the measurement covariance $\sigma_m^2 = (e_{\max}/2)^2$.

For the torque and state estimation, the noise covariances were identified empirically to achieve optimal performance. Optimal performance refers to a torque bandwidth large enough to track the fastest expected movement dynamics of the human hip and knee joint while keeping a high signal-to-noise ratio. In [Smi08], the maximum movement dynamics were reported to be 4 Hz and 5 Hz for the hip and knee joints, respectively. These requirements were met by the choice of the following covariances (validation see Sec. 3.4.2):

$$\begin{aligned} \mathbf{Q} &= \operatorname{diag}\left(10^{-6}, 10^{-5}, 0.011, 10^{-6}, 10^{-5}, 0.011\right)^2, \\ \mathbf{R} &= \operatorname{diag}\left(\frac{\pi}{2(2^{14}-1)}, \frac{\pi}{2(2^{14}-1)}\right)^2. \end{aligned} \tag{3.40}$$

The design parameters required for the UKF as described in [JU04] are set to $\alpha = 0.003$, $\beta = 2$ and $\kappa = 0$ as recommended for practical use in [KFI08].

3.4.2 Results and Discussion

Simulation Validation

As described in the previous section, the covariance matrix for the state transition was selected such that the required bandwidth for tracking the hip and knee movement is ensured. Although the double pendulum is a non-linear system, it could be observed that the magnitude response of the UKF varies little with the amplitude of the excitation signal. For this reason, a description of the filter using the Bode plot is reasonable. Fig. 3.8 shows the simulated magnitude and phase response for the subject's hip and knee torque as a function of the excitation frequency. Here, the excitation signal has an amplitude of 10 N m. The information for this diagram was obtained by utilizing the function *frestimate* in Matlab. From this, a cut-off frequency of 4.0 Hz and 13.7 Hz can be derived for the tracking of the hip torque and knee torque, respectively. The observation of the UKF by means of a Bode plot also allows a frequency-

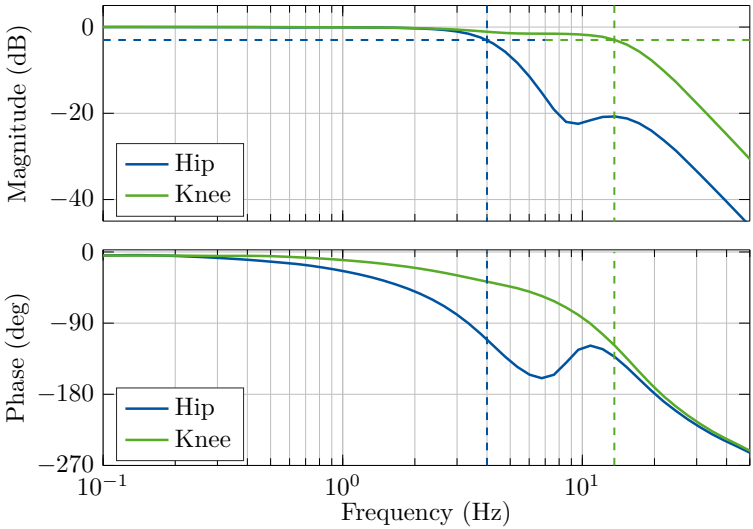

Figure 3.8: Simulated magnitude and phase response for the estimated subject's hip and knee torque given an excitation signal of the subject's hip and knee torque of 10 N m. The dotted lines represent the 3 dB cut-off frequency. (© 2022 IEEE)

dependent analysis of the coupling effects between hip and knee torque. The Bode diagrams of the coupling effects are omitted at this point for the sake of clarity. However, it could be observed that the most significant coupling from knee torque to hip torque and vice versa occurs at a frequency of 5 Hz with a coupling gain of −7.5 dB. For all other frequencies, the coupling is lower, e.g., at a frequency of 1 Hz or 23.5 Hz the coupling gain decreases to −20 dB. The fast tracking and low coupling behavior is visualized in Fig. 3.9 in the time domain. Here, 10 N m torque steps generated by the subject were simulated with the derived model from Sec. 3.3 and estimated by the UKF. Both, the tracking of the knee and hip torque have a rise time of about 137 ms. However, for hip tracking, this fast rise time can only be achieved by an overshoot of 6.5%. For the knee tracking, the overshoot is less than 1%. The faster tracking behavior of the knee torque compared to the hip torque supports the results from the frequency analysis. Because the torque is determined based on the joint angle, the higher inertia of the thigh can explain this behavior as the same induced torque results in a lower angle change for the hip than for the knee.

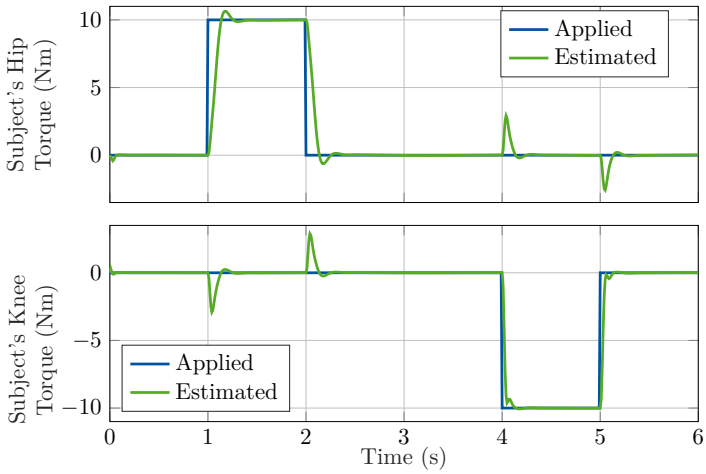

Figure 3.9: Simulation of UKF with torque steps applied by the subject. The motor torque was kept to zero.

Experimental Validation

Experimental validation for estimating the subject's active torque using the UKF is not directly possible because a measurement of the actual active subject torque is not available. For this reason, an experiment was performed in which torque steps from the two VSAs actuated the subject's hip and knee joint while the subject's leg was relaxed. Secondly, the motor torque was assumed to be the torque applied by the subject and considered a motor torque of 0 N m as the input to the UKF. The measured joint angles and torques, as well as the estimated torques, are shown in Fig. 3.10. The experiment indicates that the hip torque, in particular, is partly overestimated. This is mainly due to unintentional muscle tensing of the test subject. In addition, the estimated hip torque is noisier than the knee torque, which can be explained by the imperfect fit between the exoskeleton and the subject's torso. Despite all, the UKF shows a fast-tracking behavior of the knee and hip torque. The experiment shown in Fig. 3.10 was performed at the highest and lowest stiffness for both VSAs. The lowest stiffness slightly reduces the RMSE of the subject torque estimated with the UKF (see Tab. 3.4). On the other hand, the highest stiffness reduces

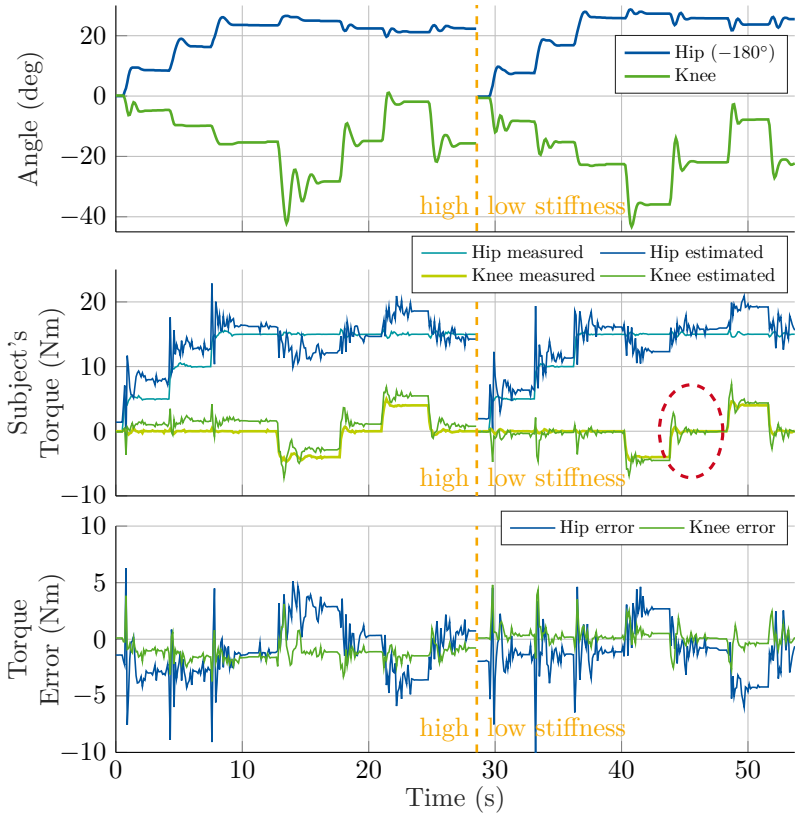

Figure 3.10: Swing trial by the test subject. Top: Measured hip and knee angle. Middle: Measured and estimated torques. Bottom: Error between measured and estimated torques. The segment outlined in red is viewed in more detail in Fig. 3.11. (© 2022 IEEE)

the maximum error that occurs during torque steps. These results suggest that the human motion intention estimation approach can be applied to other exoskeletons with compliant actuators. The only prerequisite is the accurate measurement of the interaction torque between the actuator and the human joint.

A comparison with the inverse dynamic calculation using low-pass filtered encoder signals is depicted for the knee joint for a short segment in Fig. 3.11.

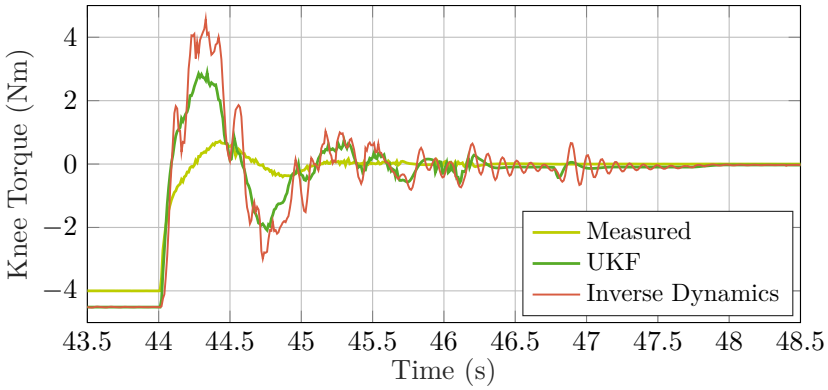

Figure 3.11: Comparison of knee torque estimated using UKF and inverse dynamics. (© 2022 IEEE)

Table 3.4: Error values of knee torque estimated using UKF and inverse dynamics. (© 2022 IEEE)

		High stiffness		Low stiffness	
Error	Joint	Inverse dynamics	UKF	Inverse dynamics	UKF
RMSE (Nm)	Hip	2.99	2.63	3.13	**2.53**
	Knee	1.57	1.41	1.24	**0.89**
Max (Nm)	Hip	17.85	**9.74**	20.72	11.45
	Knee	7.04	**4.27**	9.07	5.9

The cut-off frequencies of the low-pass filters were adjusted to achieve the same dynamic velocity as the UKF. It can be seen that both the overshoot and the noise of the estimated torque are larger for the inverse dynamics than for the UKF. This can be confirmed by the calculated error values in Tab. 3.4. In summary, the RMSE and maximum error for the hip can be reduced by 15.7% and 45.1% and for the knee by 18.1% and 36.9% using the UKF compared to inverse dynamics. A drawback of the presented methodology is that the accuracy of the UKF is highly dependent on the identified model and the subject parameters. This means that for heavier subjects, the human joint torques would be underestimated. However, this also applies to the estimation via inverse dynamics. Thus, accurate fitting is only possible by re-identifying individual subjects. However, a simple adjustment with acceptable accuracy

may be possible by adapting the mass and length parameters based on the subject's body weight and height.

3.5 Summary

In this chapter, the design of a novel exoskeleton for the lower extremities based on VSAs in hip and knee joints was presented. The serial elasticities function as a torque sensor on the output side using high-resolution angular encoders. Based on this measurement, a torque control was designed allowing the exoskeleton to follow the human gait motion with interaction torques of less than 2 N m. Using the Lagrange formalism, an accurate model for lower limb exoskeletons was developed. In particular, the accurate parameter estimation of the exoskeleton and subject parameters enabled the implementation of a UKF to estimate the subject's joint torque in the hip and knee during the swing phase. The UKF can be applied over the entire stiffness range of the VSAs and performs better than the common inverse dynamics approach. This suggests that the developed motion intention estimation approach can also be applied to other exoskeletons with serial elastic actuators or output-side torque sensors. Lastly, a static model was applied to estimate the human joint torque during the stance phase. The developed joint torque estimation opens up possibilities for the design of new patient-cooperative control methods and the high changing rates of the actuators' stiffnesses allow for compliant adaptation within one gait cycle.

4 Human-cooperative assistance control

One of the biggest challenges in rehabilitation robotics control is to command the current to the motors in such a way that the subject perceives the device as a support to its movement and not as an additional burden. This chapter therefore presents a human-cooperative control strategy that automatically supports the subject's motion while adapting the physical properties of the variable stiffness to the motion and environment. The content of this chapter has been published in the peer-reviewed journal article [BVLN23] (© 2023 IEEE).

4.1 Motivation

There are three main modes of exoskeleton-based rehabilitation training that differ on the level of patient involvement: patient-passive, patient-active, and resistance modes [CZZ+20]. The patient-passive mode imposes a fixed target trajectory, which enables movement for patients with weak or no motor function. A limitation of this approach is the suppression of voluntary movements of the user. In contrast, the patient-active mode supports patients in performing their desired movements by providing additional assistance. The resistance mode aims to strengthen the patient's muscles by counteracting their movements during a training or rehabilitation task.

The implementation of patient-active control approaches requires the detection of the timing and intensity of the patient's voluntary movement to determine the corresponding degree of assistance. In the literature, various solutions have been proposed, including position-based, force/torque, impedance-based, neural network-based, or machine learning-based control strategies [CZZ+20, WWM+14, MZD+23, VRV+22].

As described in Sec. 2.2.4, position-based and impedance-based control strategies require either a pre-recorded gait trajectory or online gait prediction. For example, Chen et al. presented a patient-cooperative control scheme based on a disturbance observer that incorporates an impedance controller supporting the user in the swing phase by providing hip and knee assistance [CZZ+20]. Furthermore, Taherifar et al. introduced an impedance-based assist-as-needed control strategy that aims at maximizing the subject's active contribution to the movement [TVG18]. Both approaches require a pre-recorded trajectory to generate user assistance.

However, pre-recorded trajectories limit the user's movement, as generic rather than personalized movement trajectories are often used. Additionally, these approaches typically support only a limited range of pre-recorded movement patterns, such as gait sequences or the *sit-to-stand* (Sit2Stand) movement, which restricts patients' freedom of movement. Li et al. overcame this problem by

proposing a cooperative control algorithm that generates a trajectory based on inverted pendulum approximation and uses virtual tunnels to achieve compliant dynamics coupling [LRZ+20].

Another way to overcome these limitations is a torque or force feedback control approach based on the patient's movement intention (see Sec. 2.2.4). This method has the advantage of supporting the user in any motion, constrained only by the mechanical limitations of the exoskeleton. However, to provide assistance in the right direction, the patient's movement intention must be determined. A new strategy on how to obtain this patient's movement intention by estimating the patient's applied torque was given in Sec. 3. Based on such a torque estimation, a torque control strategy can be implemented to assist the user. However, most torque control approaches based on the estimation of the user torque have only been implemented for upper limb exoskeletons [ZKF+20] or for isolated movements such as the Sit2Stand or the leg swing motion [LLNM20, LHP+20]. Thus, the continuous changes in the environment, as is the case during the swing and stance phases of walking, were not considered. Li et al. developed a hybrid phase torque control approach based on different dynamic models in the stance and swing phases [LDW+18]. However, the controller was only validated in a simulation environment.

This chapter aims to address this gap and presents a patient-cooperative control framework that is able to assist gait continuously in addition to other movements such as the Sit2Stand task. For this purpose, the previously presented *unscented Kalman filter* (UKF) and stance phase model will be incorporated into the patient-cooperative control framework to generate a torque reference based on the user's movement intention. The idea of the control strategy, incorporating the concept of the forward simulation presented in Sec. 2.1.4, is visualized in Fig. 4.1.

Besides the assistance control of exoskeletons, safe human-robot interaction plays a significant role in the development of lower limb exoskeletons. As described in the previous chapter, one way to provide intrinsic safety is using a compliant coupling between the actuator system and the patient [DSDB08]. In addition to intrinsic safety, compliant actuators achieve low impedance rendering and increase the stability of torque control [CF16].

Additionally, a varying serial elasticity has several advantageous properties compared to fixed elasticity. It overcomes the bandwidth limitations in the actuation resulting from fixed compliance [LPCY18] and adapts the mechanical compliance to the human's joint stiffness, e.g., by changing the coupling behavior during the gait phases [ZWCZ22]. This way, a high torque control bandwidth and stiff coupling can be provided for the stance phase, while high compliance reduces resistance during the swing phase.

Most existing exoskeletons with variable stiffness are only adjustable at

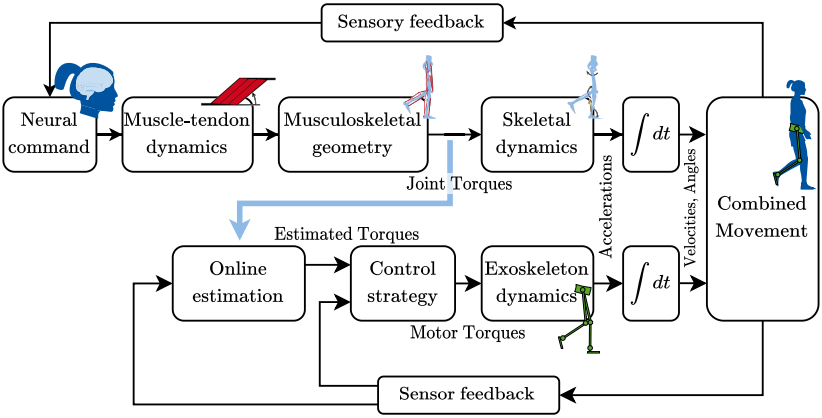

Figure 4.1: Conceptual design of the human-cooperative control strategy based on human joint torque estimation with respect to the forward simulation shown in Fig. 2.5.

very low speeds, either manually or automatically, such that the stiffness cannot be changed during one gait cycle (see Table 3.1). The VSA-EXO, introduced in [ZWCZ22], overcomes this limitation by allowing stiffness change at higher speed, however, only for one single joint with one *variable stiffness actuator* (VSA). Assisting multiple joints, e.g., hip and knee, places new demands on state estimation and control approaches due to high non-linearities.

Moreover, due to the low stiffness change rates, there are few control approaches that can both support the user and adapt physical stiffness to the gait. Existing solutions for exoskeletons mainly include a constant [GRGG+17] or a switchable stiffness trajectory between the gait phases [CSMAG15, JFWRC+18]. In prior research on other robots with independently configured VSAs, predefined trajectories for stiffness control were utilized to address the challenge of reproducing human-like dynamic motions [HHAS12, BPH+13], in addition to controlling task-space stiffness [PDAS15].

In comparison to these studies, the approach presented in this chapter utilizes human joint torque feedback to generate an adaptive stiffness trajectory for the leg swing motion, as previously proposed in [LLNM20] for an impedance-based control approach. In this thesis, a technique for stiffness generation based on the human-joint torque is combined with a switching method based on the gait phases to account for the varying stiffness requirements during different phases of the gait.

In summary, this chapter contributes a complete human-cooperative control framework that includes automated stiffness adaptation based on the user's movement intention. The main contributions of this chapter include the following:

1. A new control framework that is able to assist the user's movement without the need for a pre-recorded trajectory is presented. This is achieved through the previously described human torque estimation. This estimation is used to generate reference values for the torque controller during the swing and stance phase. The reference trajectories of the stance and swing phases are seamlessly switched through a blending approach to provide continuous gait assistance.

2. A new online adaptation of the motor's mechanical elasticity is presented to optimize the actuator characteristics according to the environment. The adaptation is based on the user torque estimation and gait phase switching.

3. Lastly, the control framework is extended with a new safety mechanism to reduce strain on the motor and the patient, when reaching the angular limits of the exoskeleton.

The control framework is evaluated on the *lower limb exoskeleton with serial elastic actuators* (L^2Exo-SE). The results are expected to aid in the design and control of future exoskeletons that utilize compliant actuators with a focus on safe physical human-robot interaction.

4.2 Cooperative Control Framework

In cooperative control, support is provided based on the subject's intention of movement. It means that the subject's muscle torque should be detected and amplified by the motor with a pre-defined or adjustable degree of support. For this purpose, the torque reference for the hip and knee joint controller should consist of two parts: The first part compensates the additional inertia and torque caused by the weight of the exoskeleton during the movement; The second part amplifies the subject's torque by a freely adjustable assistance factor k. The generation of the reference torques for the hip and knee VSA differs for the two gait phases based on the previously derived models. The two torque references are switched smoothly between the gait phases to provide assistance for the entire gait. In addition to the possibility of selecting a suitable torque reference, VSAs in general and the L^2Exo-SE, in particular, allow for adaptation of the coupling stiffness between the exoskeleton and the test person.

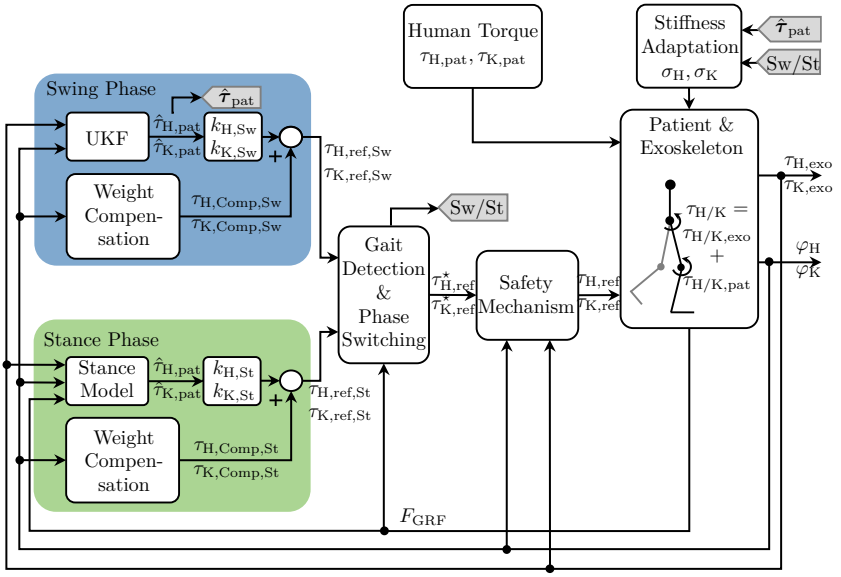

Figure 4.2: Proposed cooperative control framework for lower lower-limb exoskeletons. Assistance for hip (H) and knee (K) joints is provided linearly depending on the estimated patient's joint torque in the swing (blue box) and stance (green box) phase (see sections 4.2.1 and 4.2.2). The gait phase detection and torque reference switching are based on the GRF measurement (see Sec. 4.2.3). Subsequently, a safety mechanism ensures the user's physical safety (see Sec. 4.2.5). Lastly, the elastic coupling between the exoskeleton and the subject is adapted based on the human's torque and the gait phases (see Sec. 4.2.4). (© 2023 IEEE)

For the stiffness selection, a user torque and gait-phase-dependent approach to optimize the actuator characteristics to the varying environment is proposed. The entire control approach including the torque reference generation and the stiffness adaptation is depicted in Fig. 4.2. In the following, all individual components are explained in more detail.

4.2.1 Swing Phase Assistance

The assistance in the swing phase results from the estimated patient torque $\hat{\tau}_{H/K}$, which is amplified by a factor k. In addition, the exoskeleton's influence must be compensated by an additional torque $\tau_{H/K,Comp,Sw}$ to avoid imposing any additional resistance on the user. As a result, the total reference torque

assisting the user during the swing phase is given by:

$$\begin{pmatrix} \tau_{\mathrm{H,ref,Sw}} \\ \tau_{\mathrm{K,ref,Sw}} \end{pmatrix} = \begin{pmatrix} \hat{\tau}_{\mathrm{H,pat}} \\ \hat{\tau}_{\mathrm{K,pat}} \end{pmatrix} \cdot k + \begin{pmatrix} \tau_{\mathrm{H,Comp,Sw}} \\ \tau_{\mathrm{K,Comp,Sw}} \end{pmatrix} \tag{4.1}$$

The exoskeleton's influence $\tau_{\mathrm{H/K,Comp,Sw}}$ can be derived from the model of the swing phase given in eq. (3.24) by considering only the exoskeleton:

$$\begin{aligned} \begin{pmatrix} \tau_{\mathrm{H,Comp,Sw}} \\ \tau_{\mathrm{K,Comp,Sw}} \end{pmatrix} =& \mathbf{M}_{\mathrm{exo}}(\dot{\mathbf{q}}, \mathbf{q}, t)\ddot{\mathbf{q}} + \mathbf{C}_{\mathrm{exo}}(\dot{\mathbf{q}}, \mathbf{q}, t) \\ &+ \mathbf{D}_{\mathrm{exo}}\dot{\mathbf{q}} + \mathbf{G}_{\mathrm{exo}}(\mathbf{q}). \end{aligned} \tag{4.2}$$

The goal of this component is to compensate for the additional resistance from the exoskeleton caused by mass, inertia, and friction. As visible in eq. (4.2), the first and second derivatives of the joint angles are required to calculate the compensation torque. These can be determined by differentiating the encoder signal. However, the quantized signal of the encoder results in high noise when differentiating.
For this reason, a State Variable Filter (SVF) was used to calculate the first and second-order derivatives of the joint angles. As a first attempt, the SVF was implemented according to the methodology described by Wolfram et al. and Isermann et al. using a second-order Butterworth filter [WV02, IM11]. However, tests showed that compensation for exoskeleton inertia and friction based on the delayed angular velocity and angular acceleration signals is not beneficial. In contrast, compensating the gravitational torque that results from the mass of the exoskeleton body has provided better outcomes. For this reason, eq. (4.2) was simplified to:

$$\begin{pmatrix} \tau_{\mathrm{H,Comp,Sw}} \\ \tau_{\mathrm{K,Comp,Sw}} \end{pmatrix} = \mathbf{G}_{\mathrm{exo}}(\mathbf{q}), \tag{4.3}$$

where only the influence of gravitational torque of the exoskeleton's weight is considered.

By introducing the degree of support k and assuming a perfect torque control, the controller theoretically reduces the user's average absolute joint torque at a certain assistance value $\overline{|\tau_{k\%}|}$ compared to the torque without assistance $\overline{|\tau_{0\%}|}$ by

$$\frac{\overline{|\tau_{k\%}|}}{\overline{|\tau_{0\%}|}} = \frac{1}{1+k}. \tag{4.4}$$

4.2.2 Stance Phase Assistance

The assistance in the stance phase is analogous to the approach in the swing phase. The reference torque consists of a therapeutic assistance factor and a

weight compensation of the exoskeleton in stance phase $\tau_{\mathrm{H/K,Comp,St}}$. Similar to eq. (4.1), the reference of the stance phase is determined by:

$$\begin{pmatrix}\tau_{\mathrm{H,ref,St}}\\ \tau_{\mathrm{K,ref,St}}\end{pmatrix} = \begin{pmatrix}\hat{\tau}_{\mathrm{H,pat}}\\ \hat{\tau}_{\mathrm{K,pat}}\end{pmatrix} \cdot k + \begin{pmatrix}\tau_{\mathrm{H,Comp,St}}\\ \tau_{\mathrm{K,Comp,St}}\end{pmatrix} \ . \tag{4.5}$$

The difference is that in this case, the human torque is estimated based on the static model of the stance phase given in eqs. (3.32) and (3.29). For the same reason as in the swing phase, it is suggested that compensating the dynamics of the exoskeleton is not beneficial. In addition, the exoskeleton is not subject to high dynamics while standing on the ground during the stance phase. Due to the ground contact, it is possible to compensate the exoskeleton's own weight using $\tau_{\mathrm{H/K,Comp,St}}$. The gravitational torques acting in the knee and hip joint due to the exoskeleton's mass can be obtained by considering the lever arm and the mass of the femur frame and the torso parts of the exoskeleton. Therefore, the compensation part in the stance phase can be derived from the masses and lengths in Fig. 3.5:

$$\begin{pmatrix}\tau_{\mathrm{H,Comp,St}}\\ \tau_{\mathrm{K,Comp,St}}\end{pmatrix} = \begin{pmatrix}\sin(\varphi_{\mathrm{To}}) l_{\mathrm{To}} m_{\mathrm{To}}\\ \sin(\varphi_{\mathrm{To}}) m_{\mathrm{T}} (l_{\mathrm{T}} - y_{\mathrm{T}}) + \ldots\\ \ldots (l_{\mathrm{T}} \sin(\varphi_{\mathrm{T}}) - l_{\mathrm{To}} \sin(\varphi_{\mathrm{To}}))\end{pmatrix} \tag{4.6}$$

. All variables are directly measurable through the exoskeleton's sensors.

4.2.3 Phase Switching

The gait phases are detected by the GRF measurement F_{GRF}. If the GRFs are larger than a threshold $\underline{F}_{\mathrm{TH}} > 40\,\mathrm{N}$, the leg is assumed to be in the stance phase. However, as the two torque references for the swing and stance phases differ, a jump in the torque reference can occur during gait phase switching. To overcome this challenge, linearly crossfading between the two reference values $\tau_{\mathrm{H,ref,St}}$ and $\tau_{\mathrm{H,ref,Sw}}$ is suggested for the range between the lower threshold force and an upper threshold force equaling 10% of the subject's body weight m_{body} plus the lower threshold $\overline{F}_{\mathrm{TH}} = 0.1 m_{\mathrm{body}} g + \underline{F}_{\mathrm{TH}}$. For GRF values above or below this value, only the stance or the swing phase reference are used respectively. Thus, the following torque reference can be given:

$$\tau^{\star}_{\mathrm{H/K,ref}} = \begin{cases} \tau_{\mathrm{H/K,ref,Sw}} & \text{for } F_{\mathrm{GRF}} < \underline{F}_{\mathrm{TH}} \\ \tau_{\mathrm{H/K,ref,blend}} & \text{for } \underline{F}_{\mathrm{TH}} \leq F_{\mathrm{GRF}} \leq \overline{F}_{\mathrm{TH}} \\ \tau_{\mathrm{H/K,ref,St}} & \text{for } F_{\mathrm{GRF}} > \overline{F}_{\mathrm{TH}} \end{cases} \tag{4.7}$$

$$\text{with } \tau_{\mathrm{H/K,ref,blend}} = \frac{F_{\mathrm{GRF}} - \underline{F}_{\mathrm{TH}}}{\overline{F}_{\mathrm{TH}} - \underline{F}_{\mathrm{TH}}} (\tau_{\mathrm{H/K,ref,St}} - \tau_{\mathrm{H/K,ref,Sw}}) + \tau_{\mathrm{H,ref,Sw}}.$$

The cross-fading procedure has the advantage that no low-pass or similar filtering has to be performed, which would result in a time delay. Instead, this procedure enables a fast but smooth change between the two gait phases.

4.2.4 Stiffness Adaptation

As described in the introduction, a low-stiffness actuator provides low-impedance rendering and increases the stability of force control. On the other hand, a high-stiffness actuator yields a larger actuation bandwidth. For this reason, Liu et al. proposed to use a low stiffness for the low impedance task [LLNM20]. The low impedance task describes the task in which the human is actively moving and the actuator follows the movement to reduce the interaction torque. In addition, they used a high stiffness for the high impedance task, in which the actuator is guiding the human. In [LLNM20], the stiffness adaptation was applied during the swinging motion of the lower leg in combination with an impedance controller. For the human-cooperative assistance control, the low and high impedance tasks can be translated to low and high human torques in the presented free assistive control framework, as a low/high human joint torque results in a low/high actuator torque.
Similar to [LLNM20], the desired behavior is achieved by choosing the stiffness reference depending on the so-called **active** joint (hip/knee) torque denoted by $\tau^a_{\mathrm{H/K,pat}}$. This torque can be derived from the estimated human torque by subtracting the passive elastic torques $\tau^p_{\mathrm{H/K,pat}}$:

$$\tau^a_{\mathrm{H/K,pat}} = \tau_{\mathrm{H/K,pat}} - \tau^p_{\mathrm{H/K,pat}} \ . \tag{4.8}$$

The passive elastic torque occurs due to visco-elastic effects in the tissues surrounding the joints and can be described as a function of the hip, knee, and ankle joint [RE99]. Based on the active joint torques, the hip and knee stiffness reference for the swing phase are determined using the following linear relationship as proposed in [LLNM20]:

$$\begin{bmatrix} \sigma_{\mathrm{H,ref}} \\ \sigma_{\mathrm{K,ref}} \end{bmatrix} = \begin{bmatrix} \overline{\sigma}_{\mathrm{H}} \frac{\overline{\tau}^a_{\mathrm{H,pat}} - \mathrm{sat}(|\tau^a_{\mathrm{H,pat}}|)}{\overline{\tau}^a_{\mathrm{H,pat}} - \underline{\tau}^a_{\mathrm{H,pat}}} + \underline{\sigma}_{\mathrm{H}} \frac{\mathrm{sat}(|\tau^a_{\mathrm{H,pat}}|) - \underline{\tau}^a_{\mathrm{H,pat}}}{\overline{\tau}^a_{\mathrm{H,pat}} - \underline{\tau}^a_{\mathrm{H,pat}}} \\ \overline{\sigma}_{\mathrm{K}} \frac{\overline{\tau}^a_{\mathrm{K,pat}} - \mathrm{sat}(|\tau^a_{\mathrm{K,pat}}|)}{\overline{\tau}^a_{\mathrm{K,pat}} - \underline{\tau}^a_{\mathrm{K,pat}}} + \underline{\sigma}_{\mathrm{K}} \frac{\mathrm{sat}(|\tau^a_{\mathrm{K,pat}}|) - \underline{\tau}^a_{\mathrm{K,pat}}}{\overline{\tau}^a_{\mathrm{K,pat}} - \underline{\tau}^a_{\mathrm{K,pat}}} \end{bmatrix} . \tag{4.9}$$

Here, $\mathrm{sat}(\cdot)$ denotes the saturation function and $\overline{\tau}^a_{\mathrm{H/K,pat}}$ and $\underline{\tau}^a_{\mathrm{H/K,pat}}$ the maximum and minimum active joint torque, respectively. The idea of the stiffness adaptation with respect to the user's active torque is to provide high stiffness when the user is being guided (high impedance task) and low stiffness when the user is providing a high torque (low impedance task).
In contrast, for the stance phase, high bandwidth is required to counteract the

high gravitational forces occurring in the leg joints. For this reason, the varying stiffness approach is used during the swing phase while controlling the stiffness constantly to the highest possible value during the stance phase with

$$\begin{bmatrix} \sigma_{\mathrm{H,ref}} \\ \sigma_{\mathrm{K,ref}} \end{bmatrix} = \begin{bmatrix} \overline{\sigma}_{\mathrm{H}} \\ \overline{\sigma}_{\mathrm{K}} \end{bmatrix}. \tag{4.10}$$

4.2.5 Safety Mechanisms

As a last step, a safety mechanism was developed to take the system's electrical and mechanical restrictions into account, and, more importantly, to assist the test subject only in physiological movements, thus ensuring the user's safety.
First, maximum reference torque for the hip and knee joint was limited to 30 N m. Subsequently, the dynamics of the reference signal in the swing phase was restricted, because physiologically undesirable rapid changes in the reference torque might affect the stability of the system. The dynamic limitation is directly taken into account in the choice of the UKF weightings. The UKF ensures that a cutoff frequency of about 5 Hz is not exceeded. A limitation of the dynamics within the gait phase change and during the stance phase is not desired nor required.
To support the subject only within the physiological ranges of motion, the angular ranges for the hip and knee joints were limited, e.g., to prevent hyperextension of the leg. However, instead of an abrupt assistance loss at the motion boundaries, the usage of a spring-like transition region of the width $\Delta\varphi_{\mathrm{SR}} = 10^\circ$ is proposed. The idea of this transition region is depicted, exemplary for the knee joint, by the yellow area in Fig. 4.3. When the joint angle reaches this transition region, the subject's current movement intention is no longer reinforced but instead pushed back into the physiologically permissible *range-of-motion* (RoM) by a counter-torque that increases with the angle up to a maximum of $\tau_{\mathrm{SR}} = 15\,\mathrm{N\,m}$.
The reference torque for the transition region can be obtained by linearly crossfading between the assistance torque and the repulsion torque. The reference torque, taking into account the safety mechanism, is thus for the hip joint:

$$\tau_{\mathrm{H,ref}} = \begin{cases} \tau^{\star}_{\mathrm{H,ref}}\left(1 - \frac{\varphi_{\mathrm{H}}}{\Delta\varphi_{\mathrm{SR}}}\right) + \frac{\varphi_{\mathrm{H}}}{\Delta\varphi_{\mathrm{SR}}}\tau_{\mathrm{SR}} & \text{for } -20^\circ - \Delta\varphi_{\mathrm{SR}} \leq \varphi_{\mathrm{H}} < -20^\circ \\ \tau^{\star}_{\mathrm{H,ref}} & \text{for } -20^\circ \leq \varphi_{\mathrm{H}} < 85^\circ \\ \tau^{\star}_{\mathrm{H,ref}}\left(1 - \frac{\varphi_{\mathrm{H}}}{\Delta\varphi_{\mathrm{SR}}}\right) - \frac{\varphi_{\mathrm{H}}}{\Delta\varphi_{\mathrm{SR}}}\tau_{\mathrm{SR}} & \text{for } 85^\circ \leq \varphi_{\mathrm{H}} < 85^\circ + \Delta\varphi_{\mathrm{SR}} \end{cases} \tag{4.11}$$

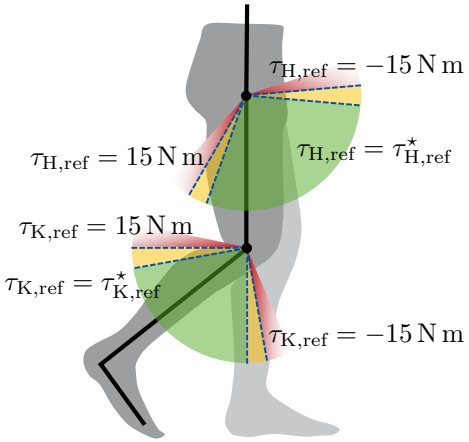

Figure 4.3: Safety mechanism for the hip and knee joint. Green: Normal operating range; Red: Counteraction torque; Yellow: Transition region (see eqs. (4.11) and (4.12)).

and for the knee joint:

$$\tau_{\mathrm{K,ref}} = \begin{cases} \tau^{\star}_{\mathrm{K,ref}}\left(1 - \frac{\varphi_{\mathrm{K}}}{\Delta\varphi_{\mathrm{SR}}}\right) + \frac{\varphi_{\mathrm{K}}}{\Delta\varphi_{\mathrm{SR}}}\tau_{\mathrm{SR}} & \text{for } -80^{\circ} - \Delta\varphi_{\mathrm{SR}} \leq \varphi_{\mathrm{K}} < -80^{\circ} \\ \tau^{\star}_{\mathrm{K,ref}} & \text{for } -80^{\circ} \leq \varphi_{\mathrm{K}} < 0^{\circ} \\ \tau^{\star}_{\mathrm{K,ref}}\left(1 - \frac{\varphi_{\mathrm{K}}}{\Delta\varphi_{\mathrm{SR}}}\right) - \frac{\varphi_{\mathrm{K}}}{\Delta\varphi_{\mathrm{SR}}}\tau_{\mathrm{SR}} & \text{for } 0^{\circ} \leq \varphi_{\mathrm{K}} < \Delta\varphi_{\mathrm{SR}}. \end{cases} \tag{4.12}$$

The final limits (red region in Fig. 4.3) are additionally secured by mechanical barriers in the exoskeleton.

4.3 Results and Discussion

All experiments were conducted by the same voluntary test person (male, 28 years, 181cm, 63kg). The experimental self-test was reported to the ethics committee at the Medical Faculty of RWTH Aachen University under the number EK353-19.

4.3.1 Simulation Results

Proof of stability of the low-level torque controller presented in Sec. 3.2.5 has already been provided by Liu et al. in [LLM18]. The stability analysis of the

upper-level overall control is challenging due to a changing, unknown environment and transitions between the swing and stance phase models. However, it can be assumed that the highest accelerations and velocities occur during the swing phase which makes this phase the most critical with regard to stability. For this reason, the frequency-dependent transfer behavior of the support control during the swing phase was investigated in a simulation.

Simulation

To analyze the transfer behavior from the subject torque (input) to the total torque (output), the dynamic user exoskeleton system described in eq. (3.24) was simulated for the knee joint only. This system was excited by a virtual, sinusoidal subject torque (amplitude 3 N m, frequency sweep from 0.1 Hz to 20 Hz). The subject torque was estimated by the UKF described in Sec. 3.3.1 and (initially) ideally amplified according to eq. (4.1) without considering the weight compensation component. Subsequently, the transmission behavior of the *mechanical-rotary variable impedance actuator* (MeRIA) including the *LQG controller with integral behavior* (LQGI) torque control at the highest and lowest stiffness was considered in the overall system. That is, the reference torque from eq. (4.1) does not directly actuate the subject/exoskeleton system but serves as a reference for the LQGI controller described in Sec. 3.2.5, which controls the interaction torque between the MeRIA and the exoskeleton.

Results

The frequency-dependent transfer behavior is depicted in terms of magnitude and phase response in Fig. 4.4 for different support factors $k \in [-40\%, 100\%]$.

It is apparent that at a subject torque frequency of up to approximately 2 Hz, an almost constant support magnitude is achieved for positive support factors (blue graphs), whereby the absolute phase shift is smaller than 23.7°. For higher frequencies, the support gain decreases until it reverses to resistance at about 4 Hz. For negative assistance factors (purple graphs), the behavior is reversed. From approximately 1 Hz, the resistance behavior decreases (negative magnitude) and becomes negative (positive magnitude, assistive behavior) at 3 Hz.

With regard to torque control and actuator dynamics (green and gray area in Fig. 4.4), a similar response was obtained. However, here the inflection point shifts to lower frequencies (1.5 Hz). Furthermore, the amplification's magnitude increases between 0.3 Hz and 0.9 Hz compared to the ideally actuated system, reaching the peak at 0.62 Hz. The maximum magnitude depends on the assistance factor. Fig. 4.4 shows that the maximum gain factor for the

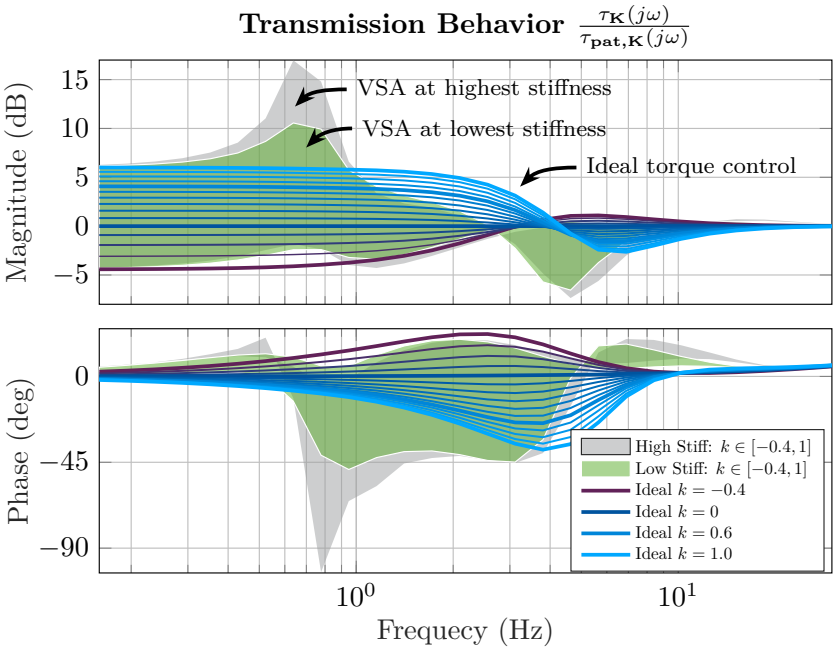

Figure 4.4: Simulation results. Transfer behavior of subject torque (input) to total torque (output) as a function of the frequency of the sinusoidal input (3Nm amplitude). The line graphs show the transmission behavior for ideal torque control at different assistance factors k without taking actuator dynamics into account. The grey and green areas visualize the change of the transmission behavior considering the MeRIA actuator at highest and lowest stiffness, respectively. (© 2023 IEEE)

MeRIA at the highest stiffness is significantly higher than for the actuator at the lowest stiffness.

Discussion

The simulation demonstrated that assuming an ideal torque application to the exoskeleton, the subject torque can be amplified through positive assistance factors k up to a frequency of 3.5 Hz, where the amplification between 2 Hz and 3.5 Hz is slightly below the requested assistance. Frequencies in the subject's torque above 4.2 Hz are slightly suppressed. This behavior is particularly

advantageous for patients undergoing rehabilitation, as it suppresses unplanned rapid movements, providing additional safety.

To set the frequency in relation to walking speed, the cadence of healthy subjects walking on level ground is considered first. Tudor-Locke et al. defined a walking cadence of 60-79 steps/min as slow, 80-99 steps/min as normal, and 100-119 steps/min as fast walking [TLCL+11]. Furthermore, they found a linear correlation between cadence and walking (r=0.97) [TLWRP02]. Linear regression results in ranges of walking speed with respect to the cadence of $0.7\,\mathrm{km\,h^{-1}}$ to $2.3\,\mathrm{km\,h^{-1}}$ for slow, $2.3\,\mathrm{km\,h^{-1}}$ to $3.9\,\mathrm{km\,h^{-1}}$ for normal and $3.9\,\mathrm{km\,h^{-1}}$ to $5.4\,\mathrm{km\,h^{-1}}$ for fast walking. Cadence can be converted to stride frequency by dividing the number of steps per second by two. *In repetitive movements, the frequencies present will be multiples (harmonics) of the fundamental frequency (stride frequency)* [Win09]. Assuming this definition, the UKF approach is able to amplify the first 5-7, 4-5, and 3-4 harmonics for slow, normal, and fast walking, respectively. Higher harmonic frequencies will be slightly suppressed or transmitted transparently.

The simulation demonstrates that the UKF used for estimating the subject torque during the swing phase is generally suitable for control in exoskeletons. However, when considering the dynamics of the torque controller and the MeRIA actuator, the assistance gain and phase shift increase at low frequencies. This suggests that high assistance factors should be chosen cautiously to avoid unpleasant or uncontrollable support for the subject. Both the increased magnitude and phase shift are significantly more pronounced in the VSA with a higher stiffness than in the VSA with a lower stiffness. This supports the approach of reducing the mechanical stiffness of the VSA during the swing phase to optimize the physical human-robot interaction.

Furthermore, the frequency up to which subject torques are supported is reduced, when the VSA dynamics are taken into account. Thus, only the first 3-4, 2-3, and 2 harmonic frequencies are amplified for slow, medium, and fast walking. Since slow gait speeds are particularly relevant for rehabilitation therapy, Sec. 4.3.5 investigates how the support of the 3-4 harmonics affects the subject's gait experimentally.

In general, the simulation results indicate that the high-level control is generally stable and assists the user's torque input. Additionally, for negative support factors, an active resistance torque counteracts the subject torque. The resistance is reduced at higher frequencies, which particularly facilitates the onset of movements. Lastly, it should be noted that – independent of the assistance factor – very high subject torques could cause the exoskeleton to reach its mechanical limits, which is why the additional safety mechanisms presented in Sec. 4.2.5 were incorporated.

4.3.2 Swing Phase Assistance

Experiment

An experiment with repetitive knee joint motions at different assistance factors k was conducted to validate the assistance control for the swing phase in the L^2Exo-SE. During this experiment, the test subject wore the exoskeleton and sat on an elevated chair to allow free movement of the lower leg (see Fig. 4.5). Subsequently, the test person moved the lower leg in a sinusoidal trajectory while the assisting factor is increased every ten periods. For a quantitative comparison of the applied torques, the test person was instructed to keep the movement identical in all scenarios. To support the subject in following a sinusoidal movement trajectory, a sine wave with constant amplitude (20°) and frequency (0.32 Hz) was visualized on a screen. During the entire experiment, the serial elasticity of the knee actuator was set to the highest value (408 $\frac{\mathrm{N\,m}}{\mathrm{rad}}$), and the safety mechanism described in Sec. 4.2.5 was deactivated to allow greater knee flexion.

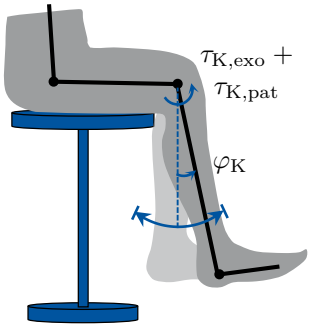

Figure 4.5: Visualization of the experimental setup. Note: The definition of the knee angle in the sitting position differs by 90° compared to the knee angle introduced in Fig. 3.5. (© 2023 IEEE)

Results

The mean knee joint angle, measured motor torque and estimated subject torque of the ten repetitions, and the standard deviation are visualized in Fig. 4.6 for seven different assistance settings. The subject moved his leg with a time period of $3.1356 \pm 0.1540\,\mathrm{s}$. The low standard deviation of the repeated knee movement (4.9% of the mean value) suggests the quantitative comparison of

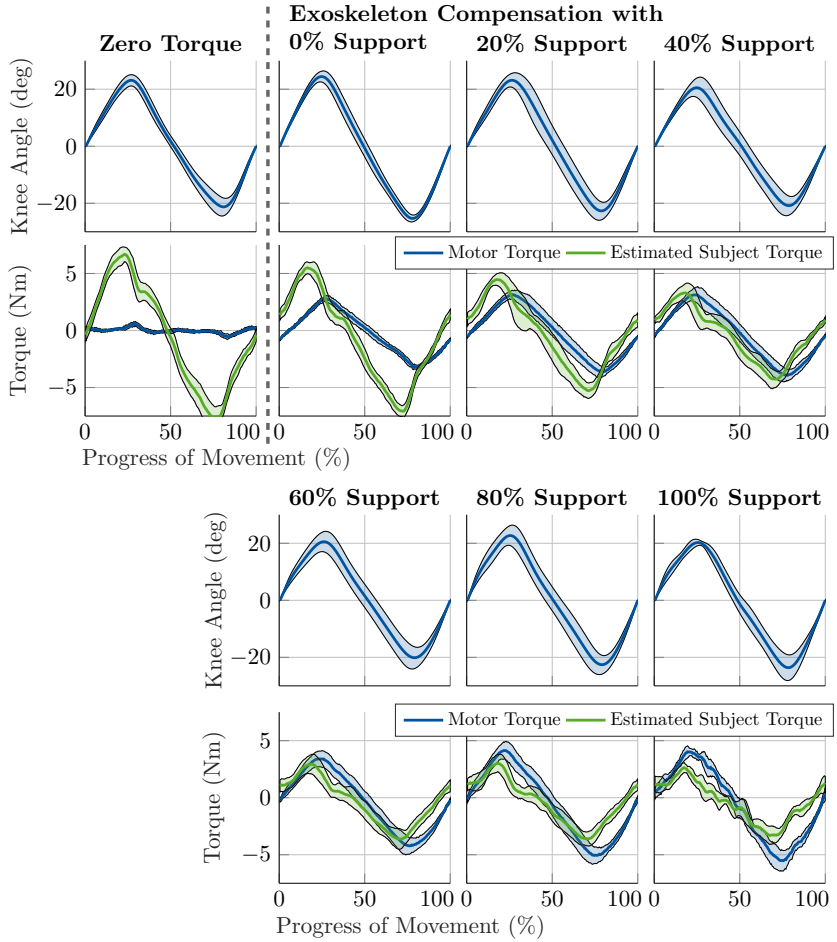

Figure 4.6: Knee Angle (top) and motor and subject torque (bottom) of periodic lower leg swing motion with different assistance factors. The trajectory followed has an amplitude of 20° and a period of 3.14 s (corresponds to 100%). Shadowed areas represent the standard deviation of the repeated movement task. (© 2023 IEEE)

the different swing movements.

The zero torque control (Fig. 4.6, 1st column) validates the compliant behavior of the torque control strategy. The interaction torque between human and motor does not exceed $0.61 \pm 0.17\,\mathrm{N\,m}$. The influence of the compensation control of the exoskeleton's weight can be observed by comparing the motor torque of the zero torque case (1st column) with the 0% assistance case (2nd column, 1st row). Here, the maximum absolute torque caused by the weight of the exoskeleton's lower leg amounts to $2.79 \pm 0.26\,\mathrm{N\,m}$. The weight compensation control reduces the subject's maximum absolute torque by $19.40 \pm 0.26\,\%$.
A further reduction of the estimated subject's torque was achieved by increasing the assistance factor k. It is noticeable that the subject's torque decreases with increasing assistance factor. The theoretically achievable reduction is given by eq. (4.4) and visualized by the grey graph in Fig. 4.7. The actual reduction of the absolute subject's torque for the tested assistance factors k is depicted by the green graph.

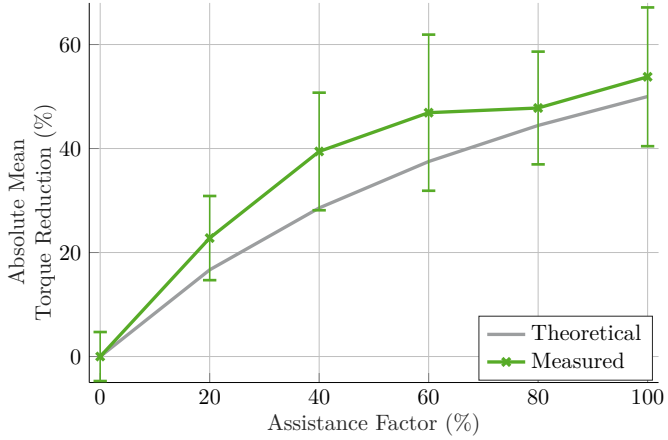

Figure 4.7: Mean reduction of the absolute subject torque for different assisting factors k compared to 0% assistance with exoskeleton compensation. (© 2023 IEEE)

Discussion

The experimental results validate the control system's capability to follow the user's movement intention, which is crucial for providing effective assistance to the user.

Importantly, the experiment indicates that the user torque required to perform a movement with the exoskeleton's assistance is significantly reduced. The results indicate that for all selected assistance values, the average user torque is reduced slightly more than theoretically expected (see Fig. 4.7). For example, for an assistance factor of $k = 60\%$, the user can perform the same movement with 46.9% (theoretical: $100\% - \frac{100}{100+40}\% = 37.5\%$) less torque compared to no assistance (only exoskeleton weight compensation). This also supports the simulation results in Sec. 4.3.1 that account for the VSA's dynamics.
The proposed control approach of the positive feedback loop requires active user input to be amplified which is simultaneously an advantage and a disadvantage. The higher the amplification factor is, the lower the user torque is required for the movement. However, when the user torque decreases, the estimation of the user torque becomes difficult due to a low signal-to-noise ratio. Hence, delays and noise in the measurements, estimation, and control action become more apparent. This effect is noticeable for an assistance factor of $k = 100\%$. Here, small oscillations are detected as visible in the bottom right graph in Fig. 4.6. These small oscillations can be sensed by the user. For optimal safety and user experience, it is suggested to limit the assistance factor to a maximum of $k = 60\%$.

4.3.3 Stance Phase Assistance and Sit-to-Stand

The *sit-to-stand* (Sit2Stand) movement is a widely studied motion for exoskeleton research and development. During this movement, high torques occur and patients with impaired mobility often find this task particularly challenging. Therefore, many publications have been dedicated to developing control systems for the Sit2Stand task. The proposed stance phase assistance control approach can directly support the user during the stand-up and sit-down movement. The stand-up movement, as an isolated and self-contained movement, provides a concise way to validate the performance of the stance phase support control.

Experiment

The test person repeated the stand-up movement from a chair while wearing the lower limb exoskeleton four times with an assistance factor of $k = 0\%$ and four times with assistance of $k = 40\%$. The measured hip and knee angles and torques are visualized as the means of the average values and standard deviations in Fig. 4.8.

Results

The maximum hip joint torque is reduced from 39.05 N m for the $k = 0\%$ to 29.34 N m for $k = 40\%$. These experimental values correspond to a 24.87 % reduction, while the theoretically calculated reduction for a 40 % assistance

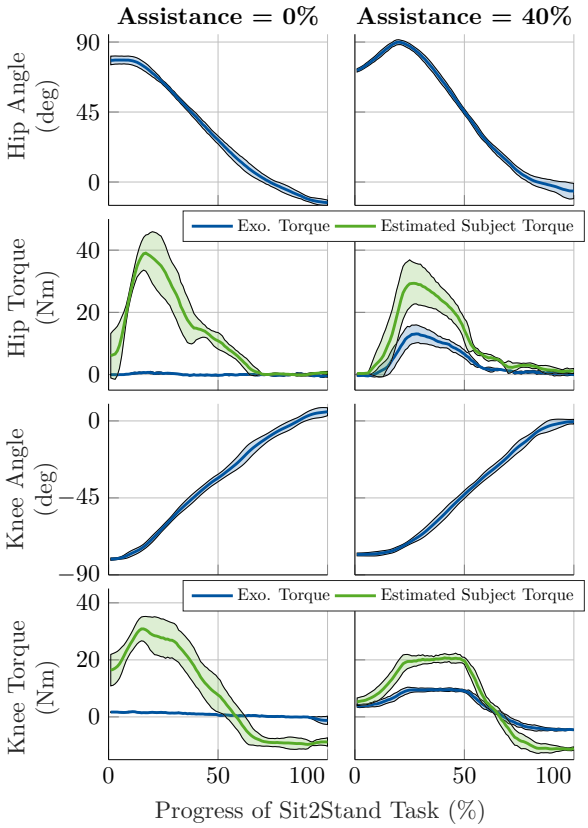

Figure 4.8: From top to bottom: Hip angle, exoskeleton's (blue) and subject's (green) hip joint torque, knee angle, and exoskeleton's (blue) and subject's (green) knee joint torque in the Sit2Stand task. The data shows the mean values and standard deviations of four repeated movements. The Sit2Stand task was performed in 4.44 ± 0.26 s for the 0% assistance case and in 4.34 ± 0.12 s for the 40% assistance case. (© 2023 IEEE)

factor is 28.57%. The reduction of the maximum knee joint torque from 30.86 N m to 20.72 N m during 40 % assistance is 32.88 %.

Discussion

The experiment indicates that the control system is capable of providing the expected level of assistance during the Sit2Stand movement. However, the subjective feeling of assistance varied among the different stand-up movements, which may be caused by the limited number of ground reaction force sensors in the sole of the exoskeleton. With only four force-sensing resistors, each measurement has a significant impact on the reference torque value. To improve the subjective experience, the number of ground reaction force sensors could be increased to provide more accurate reference torque values.
Again, it is suggested to set the upper limit of the support factor to 60 %. In this case, the purpose is to limit the maximum torque applied by the motor rather than to avoid oscillations, as a static model is used.

4.3.4 Safety Mechanism

The safety mechanism presented in Sec. 4.2.5 aims to support the user in physiologically permissible movements and to reduce the shock when the mechanical limits are reached abruptly. The latter serves to protect both the user and the mechanical system, including the motor.

Experiment

To test the effectiveness of the proposed safety mechanism, an experiment was conducted, in which the test person repeatedly pushed his lower leg with a high velocity into the mechanical limitation at $\varphi_K = -90°$. As proposed in Sec. 4.2.5, an angle-dependent, increasing torque was provided over a range of 10° before reaching the mechanical limitation to counteract the movement. The experiment was conducted both at the highest and lowest stiffness of the VSA.

Results

The results of the experiment are visualized in Fig. 4.9 by means of the average knee angle, angular velocity, and motor torque of 18 repetitions at the highest (left) and lowest (right) actuator stiffness. Each movement takes approximately 1.1 s corresponding to 100 % progress of the movement. The knee angle attains a minimum angle of −90° at which the exoskeleton's lower leg is mechanically restricted. The average maximum velocity, at which the lower leg reaches this limitation, is $-2.5\,\mathrm{rad\,s^{-1}}$ for the high and low stiffness case. The *mean absolute*

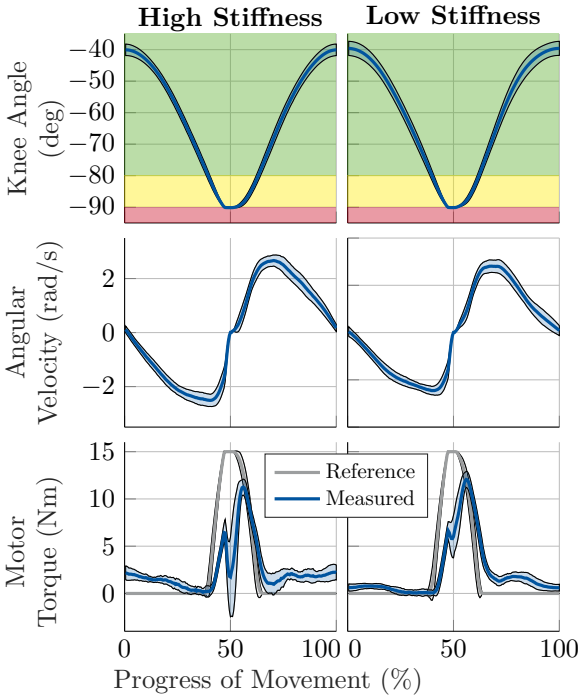

Figure 4.9: Safety mechanism experiment. Knee angle, angular velocity, and motor torque at high (left) and low (right) actuator stiffness while actively pushing the lower leg into the mechanical limitation. The mechanical limitation is set to -90°. The movement is repeated 18 times for both stiffness cases. The movement duration of each repetition is 1.09 ± 0.07 s and 1.13 ± 0.03 s for the high stiffness and low stiffness case, respectively. (© 2023 IEEE)

error (MAE) between the angular velocities for the high and low stiffness case is $0.14\,\mathrm{rad\,s^{-1}}$, which corresponds to 8.9% of the mean average signal.
After reaching a knee angle of −80° at around 40 % of the movement's progress, the reference torque increases to slow down the movement before reaching the mechanical limits. The reference torque reaches the limit of 15 N m within 93.5 ms. Due to the high speed of the lower leg, the torque control can only reach half of this value before the lower leg crashes into the limitation. Contact with the mechanical limitation leads to a fast torque drop of 4.71 N m and 0.81 N m on average for the high and the low stiffness case, respectively. Subsequently,

the torque increases again, moving the leg forward and away from the limitation.

Discussion

The motion shown in Fig. 4.9 is induced by the test person. Therefore, direct comparability of the results, especially the torque during the collision for high and low stiffness is only permitted for similar motion profiles. The low MAE of the velocity signal indicates that the two experiments are comparable.
For both cases of the experiment, the knee joint stayed within safe physiological limits as the mechanical limitations ensure that the angle of $-90°$ is not exceeded. In addition, the motor torque counteracted the movement, reducing the impact on the mechanical limits. As a result, the strain on the motor and the user's leg was reduced.
In this specific experiment, it could be observed that the sudden torque drop during impact is 82.8 % lower for the low stiffness case than for the high stiffness case. This indicates better absorption capabilities of the low-stiffness actuator in comparison to the high-stiffness actuator, which means that the low-stiffness actuator can better counteract shocks resulting from a sudden change in environment or joint stiffness. This supports the proposition from Sec. 4.2.4 to reduce the actuator stiffness during the swing phase depending on the user's torque.

4.3.5 Full Gait Assistance with Varying Stiffness

Gait consists of a sequence of swing and stance phases for each leg. The following experiment aimed to validate the overall patient-cooperative control during this sequential movement. This includes the support in the two different phases, the transition in between, and the adjustment of the physical elasticity of the VSAs. Furthermore, the active resistance of the exoskeleton was analyzed by considering negative assistance values.

Experiment

To validate the assistance behavior of the proposed control strategy during gait, the test subject walked on a treadmill at three different speeds of ($0.8\,\mathrm{km\,h^{-1}}$, $1.1\,\mathrm{km\,h^{-1}}$ and $1.4\,\mathrm{km\,h^{-1}}$). For each pace, the assistance factor k for the hip joint was varied from -40% to +60% in 20% intervals, while keeping the knee assistance at 0%. The support was increased after every 20 steps walked. Then, the knee's assistance factor was varied while leaving the hip assistance constant. Changing the support factors for each joint allows for determining the influence of the respective assistance change.

Results

The results of the gait experiment are presented in Fig. 4.10 by means of torque and power reduction. The data was obtained from the experimental results visualized in the appendix in Fig. A.2. In detail, the left graphs show the reduction of the subject's MAE for different assistance factors compared to the 0% assistance case for the hip and knee joint. On the right, the reduction of the mean absolute power, as the product of the joint torque and angular velocity, is visualized. For both – the torque and power – the reduction increases with increasing assistance factors for all gait velocities. It is apparent that there is no significant difference in the torque reduction between the three different

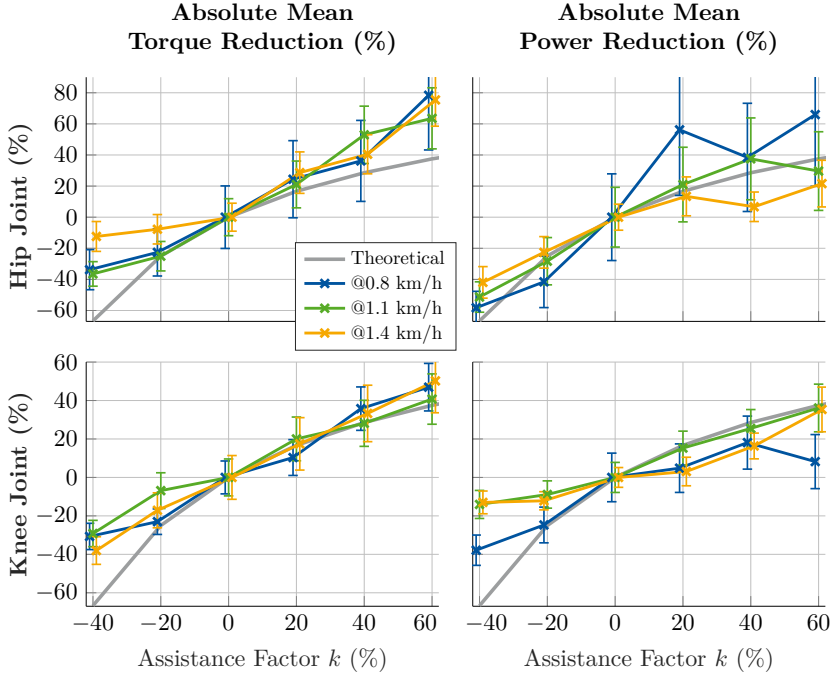

Figure 4.10: Gait experiment results. Reduction of absolute mean torque (left) and absolute mean power (right) for different assistance factors compared to 0% assistance for hip (top) and knee (bottom) joints during treadmill walking at different velocities. The grey line visualizes the theoretically calculated reduction in the dependence on the assistance factor. (© 2023 IEEE)

gait velocities. The mean torque reduction for the hip joint tends to be above the theoretically calculated support, whereas that of the knee joint matches the theoretically calculated support closely for positive support factors. The deviation from the theoretically achievable torque reduction is highest at a support factor of -40% for both joints. It is noticeable that in the hip, power reduction decreases with higher gait velocities for large k. This trend is not observed for the knee joint.

The course of the joint angles, torques, and VSA stiffnesses is shown exemplarily for one gait speed ($0.8\,\mathrm{km\,h^{-1}}$) and for three different assistance factors in Fig. 4.11. Results for more assistance factors are given in the appendix in Fig. A.2. As previously stated, the subject's active knee and hip joint torque (see eq. (4.8)) decreases with increasing assistance factor. Furthermore, it can be seen that the stiffness values of the hip and knee actuator are reduced during the swing phase based on the active subject torque - as described in Sec. 4.2.4. Here, a noticeable discrepancy between the stiffness reference and the actual set elasticity is apparent. The following discussion explains the reasons and effects in more detail.

Discussion

The experiment indicated that the proposed control concept is capable of reducing and increasing the subject's hip and knee torque and power with positive and negative assistance factors, respectively, at different gait speeds. The reduction of the subject's joint torque was within the expected range for a wide range of support factors. Only for negative assistance factors, the control provided less active resistance than required, which supports the findings of the simulation.

The predictive value of these results is limited by the relatively low gait velocity of $1.4\,\mathrm{km\,h^{-1}}$. However, for rehabilitation purposes, this velocity is expected to be sufficient. In further tests, it could be determined that the knee support functions reliably up to $3\,\mathrm{km\,h^{-1}}$, although the effectiveness of the support decreases slightly with increasing velocity as suggested by the simulation results. However, the hip support can only be used up to $2\,\mathrm{km\,h^{-1}}$, as the control was tested on an exoskeleton prototype that has not yet been optimized for weight. At a lower weight of the actuators and the frame, the exoskeleton would need less torque to compensate for its own mass, enabling faster gait speeds.

Another reason for better performance of the knee joint than the hip joint assistance is the partly elastic, non-optimal coupling of the hip motor to the user's waist. This makes the assumption of fixed coupling between the user and the exoskeleton joint only partially valid. It was already compensated for this misalignment by determining the hip angle based on two inertial measurement

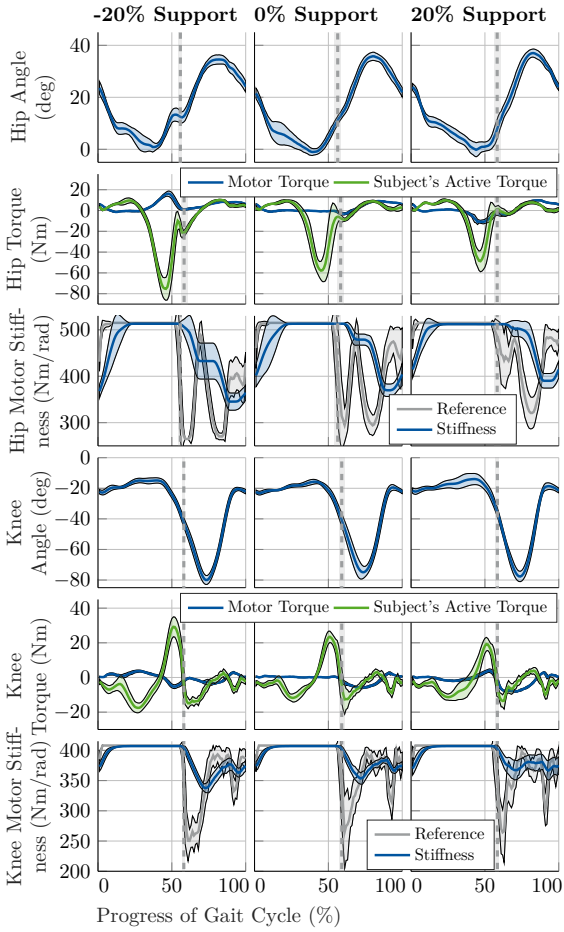

Figure 4.11: Gait experiment results. Hip and knee angle, hip and knee joint torques, and hip and knee motor stiffness for three different assistance factors. Solid lines are the average of ten steps, and the shaded areas are the standard deviation. The vertical lines present the toe-off event, therefore the transition from the stance to the swing phase. (© 2023 IEEE)

units (IMUs) attached to the user's thigh and torso. However, this does not compensate for the backlash that occurs between the hip shell and the motor

when the direction of support changes. To solve this problem in the future, a better hip fixation would need to be selected. Alternatively, the control strategy could explicitly take the backlash into account.
In all previous evaluations, the change of the torque is considered with reference to the 0% assistance case with exoskeleton compensation. The advantage of this approach is that the torque and power reduction already take into account the possible change in the user's gait due to the assistance, the so-called human motor adaptation. However, the presented evaluation does not take into account the actual effects on the generation of human torque. For this purpose, in the future, the muscle activity and metabolic cost of the subject could be measured for different assistance factors.
The evaluation of the stiffness adaptation has shown that the mechanical design of the variable stiffness cannot follow the fast torque changes of the knee and hip joints. Instead, the resulting actuator stiffness corresponds to a low-pass filtered behavior of the active subject torque during the swing phase.
Despite the non-optimal stiffness adjustment, the average stiffness during the swing phase increases with the assistance factor. This behavior supports two desired properties. First, a higher support factor also implies a higher required motor torque, which is better achieved by a stiffer actuator (high impedance task, see Sec. 4.2.4). On the other hand, with a lower support factor, a higher subject torque can be expected (low impedance task). For this case, higher elasticity is advantageous, as it ensures a higher disturbance rejection and higher safety as shown in Sec. 4.3.4.

4.4 Summary

In this chapter, a novel human-cooperative control framework was presented that is capable of assisting the user during the entire gait sequence and other movements such as Sit2Stand. The control framework utilizes a UKF and inverse kinematics to estimate the user's joint torques during the swing and stance phase, respectively. The control approach, which is generally transferable to exoskeletons with compliant actuators, was validated using the L^2Exo-SE. The assistance is applied in accordance with a freely selectable parameter. The average user's joint torque during gait could be reduced by 63.6 % - 78.4 % for the hip and 40.8 % - 50.2 % for the knee joint compared to unassisted walking. Furthermore, an automated stiffness selection for the serial elasticity of the VSA based on the human's active joint torque was presented. The stiffness adaptation increases the safety of the physical human-robot interaction during the swing phase while maintaining a high control bandwidth during the stance phase. In the future, the influence of human-cooperative control on the human

body should be investigated by *electromyography* (EMG) and metabolic cost measurements, and further tests should be performed not only on healthy subjects but also on patients with hemiplegia. In addition, the question remains of how to choose the assistance factor depending on the patient's or user's state of health or fitness.

5 Fatigue Assessment and Fatigue Control

In robotic-assisted rehabilitation therapy, the settings and assistance of the exoskeleton is based on the physiotherapist's estimation of the patient's strength. In this chapter, a new automated method based on real-time estimation and control of muscle strength and fatigue is proposed. The content of this chapter has been published in the peer-reviewed journal article [BHvP+24] (© 2024 IEEE).

5.1 Motivation

Fatigue is a common experience in our everyday activities. It poses a particularly challenging obstacle for individuals with hemiparesis whose muscle function are compromised. These patients often describe fatigue as an intense feeling of tiredness, exhaustion, and a lack of physical and mental energy, which hinders their daily tasks. Research shows that up to 72% of stroke survivors experience fatigue, and 46% consider it their most debilitating symptom [KRG12]. Furthermore, patients with incomplete *spinal cord injury* (SCI) endure increased muscle fatigue during extended periods of walking. This finding suggests that fatigue management should be considered in their rehabilitation process [DNG+20]. By acknowledging fatigue in daily life and during rehabilitation, the risk of falling can be minimized, as fatigue can affect gait parameters, increasing the likelihood of falls [PL08, DNG+20].

As described in Sec. 2.1.6, fatigue can be classified as either mental or physical, with mental fatigue being related to cognitive and perceptual aspects and physical fatigue being expressed by decreased performance of the motor system. Muscle fatigue is a type of physical fatigue that can be defined as 'any exercise-induced reduction in maximal capacity to generate force or power output' [Vøl97]. It is often characterized by a decline in *maximum voluntary contraction* (MVC), which measures the force generated by an individual at maximal effort. The reduction of strength depends on the type of contraction, with sustained maximal contraction causing an immediate onset of fatigue and a strict decline in force output, while repeated sub-maximal contractions allow for force to be maintained for a longer time until exhaustion.

Several physiological and mathematical models have been developed to describe muscle fatigue. Physiological principles usually describe fatigue for a single muscle stimulated by *functional electrical stimulation* (FES). For example, Giat et al. investigated the relationship between muscle fatigue and the intracellular pH value of a paralyzed quadriceps muscle under FES [GMLO93]. Additionally, Wexler et al. proposed a fatigue model based on the Ca^{2+} cross-bridge mechanism [WDBM97], while Riener and Quintern introduced a muscle

fitness function based on the recruitment of *Motor Units* (MUs) (see Sec. 2.1.2) that takes fatigue and recovery into consideration [RQ97].

However, movements in everyday tasks or in rehabilitation therapy are performed by the person's voluntary movement and not by external stimulation as during FES. For this reason, Liu et al. [LBY02] and Ma et al. [MBCZ08] developed mathematical models describing the fatigue and recovery behavior depending on the normalized force input, which were extended and modified by other research groups.

Liu's fatigue model, grounded in MU theory, uses differential equations to illustrate muscle activation, fatigue, and recovery [LBY02]. Xia et al. expanded this model to sub-maximal contractions and joint-level dynamic tasks, introducing the *three-compartment controller* (3CC) fatigue model [XL08]. Yet, the model's validity was mainly confirmed for isometric contractions of different joints [FLLH12] and for intermittent isometric contractions [SP16, LHFL18]. Other modifications to the 3CC model include Sonne et al.'s scaled MU fatigability [SP16] and Looft et al.'s resting recovery parameter (3CCr) representing the hyperemia effect during rest [LHFL18]. Jang et al. integrated perceived exertion and arm kinetics into the 3CC model for a continuous pointing task [JSAR17].

Ma et al., on the other hand, presented a framework for evaluating muscle fatigue in ergonomic contexts to mitigate musculoskeletal disorder risks [MBCZ08]. This model assumes fatigue increases with load, task duration, and decreasing muscle capacity. It was validated against other fatigue models [MCBZ09] and enhanced to encompass joint-level fatigue and rest intervals [MCB$^+$10]. Fayzi et al. extended the model by simultaneous recovery and fatigue for cycling applications [FWL$^+$13]. Dobrijevic at al. extended this approach to describe fatigue during walking [DIDJ17]. However, the measurement of force was performed by pulling a load cell forward that makes the subject lean forward varying slightly from the actual walking position.

Despite the underlying mathematical model, the question remains of how to accurately measure fatigue during a task. Typically, MVC and maximal power output measurements are considered the "gold-standard" [GLK00, KANP02] and "serve as the first choice of method" [Vøl97]. Other methods to assess fatigue are the measurement of force and power output, endurance time, *electromyography* (EMG), *heart rate* (HR), and subjective fatigue scales. MVC can be assessed using a load cell or dynamometer. However, it is important to discern between different contraction types. Estimating isometric contractions can be quantified due to the known and unchanging force direction. In exercises involving dynamic contractions, like walking and cycling, MVC estimation is more challenging. This is because movements are produced by a group of muscles, making the effect of the agonist and antagonist on force generation variable and unpredictable [Vøl97].

Being able to assess the behavior of muscle fatigue, the question arises of how to integrate fatigue models in control algorithms of assistive devices to minimize the effect of fatigue. As fatigue is a prominent and impairing symptom that hemiplegic patients experience during rehabilitation sessions, the integration of a fatigue model into the control strategy of exoskeletons might be beneficial. Such an integration would allow not only the tracking of fatigue progression but also aid in fatigue management. Research groups have, for example, incorporated fatigue models in the control of hybrid exoskeletons [KBA+17, BMD+20, Ali17, LMP+23] and electrically powered bikes [BLGM21].

Kirsch et al. [KADS16, KBA+17] and Boa et al. [BMD+20] applied allocation control strategies, including the modeling of muscle fatigue for hybrid exoskeletons. A hybrid exoskeleton combines muscle stimulation with FES and a powered exoskeleton. Both research groups used the fatigue model of Riener and Quintern [RQ97], describing the muscle fitness function during muscle stimulation. One strategy to overcome the effect of muscle fatigue is a switching control algorithm [KADS16]. The system switches between FES and the motor according to the development of muscle fatigue. In case muscle fatigue develops and the torque output during stimulation significantly decreases, the control switches to the electrical motor allowing recovery of the muscle.

The modeling and control of an upper-limb exoskeleton considering muscle fatigue was proposed by Ali [Ali17]. In this context, the modeling of the exoskeleton, the human, and the muscle fatigue using the model of Ma et al. [MCB+10] was performed in a virtual environment. The quasi-static fatigue model on the joint level requires the torque trajectory, which was calculated using inverse dynamics. The exoskeleton is activated as soon as the risk of fatigue occurs. Apart from that, the incorporation of a fatigue model into the control of lower limb exoskeletons without FES has not been investigated to the best of the author's knowledge.

The scientific contribution of this chapter is that

1. for the first time, a real-time quantification and control of physical fatigue during walking was made possible. To achieve this, the 3CCr fatigue model for the dynamic task of walking was adapted by considering alternating muscle activation of the lower limb muscles. An experimental study was performed to estimate individual model parameters that describe the fatigue development of four muscle groups, responsible for hip and knee movements. While performance fatigability was assessed using MVC measurements to obtain the decline in muscle strength, a subjective scale rates the perceived fatigability.

2. the developed fatigue model was integrated into the exoskeleton's control strategy to achieve a target fatigue level. The *human-in-the-loop* (HiL)

control considers the linear relation between the subjective ratings of fatigue and the MVC decline and uses a *feed-forward* (FF) controller in combination with a proportional feedback controller to ensure a predefined fatigue level throughout the training session. This study, conducted with healthy subjects as an initial proof of concept, aimed to lay the groundwork for future fatigue assessment and control in patients with hemiparesis.

5.2 Fatigue Model Development

To describe fatigue, a fatigue model from the literature was used as a starting point and adapted for the gait wearing an exoskeleton. In the following, the selection process, the basic model description, and the extension are presented.

5.2.1 Fatigue Model Selection

For the modeling of fatigue during walking in a purely mechanical powered (no FES) exoskeleton, a mathematical model based on the user's force/torque input is used rather than a physiological one. The model of Fayazi et al. [FWL$^+$13], which has also been employed by Dobrijevic at al. [DIDJ17] for walking applications, requires a 'Maximal Effort' approach for parametrization. This fact makes the model unsuitable for patients with limited walking ability.

Thus, the question arises whether to use the MU-based fatigue model introduced by Liu et al. [LBY02] or the model of Ma et al. [MBCZ08]. The MU-based fatigue model considers simultaneous fatiguing and recovery of the MUs, which represents the physiological fatigue mechanism of a muscle. While simultaneous fatigue and recovery were also considered in some modifications of the fatigue model of Ma et al. [MCBM12], it is not necessarily part of the fatigue model. For example, the translation of the fatigue model to dynamic tasks by Seth et al. did not consider recovery effects [SCB$^+$16]. Accounting for the available fatigue and recovery parameters, the MU-based 3CC and 3CCr fatigue models provide parameters for the knee joint for isometric and intermittent contractions [FLLH12, LHFL18]. In contrast, the model of Ma et al. was mainly applied for push and pull tasks, focusing on the fatigue parameters of the shoulder and elbow joint, which has limited relevance for walking with the exoskeleton. The availability of fatigue and recovery parameters of the knee joint allows the discussion of the developed fatigue model by comparing the estimated parameter with the literature. In summary, the decision to select the 3CCr model for this application was influenced both by the availability of pertinent model parameters and its successful validation for intermittent tasks, which closely resemble dynamic tasks. Lastly, this approach also allows the connection to perceived fatigue, as the relation between *ratings of perceived*

fatigue (RPF) and the torque decline modeled by the 3CCr model has been investigated by Whittaker et al. [WSP19] and applied by Jang et al. [JSAR17].

5.2.2 3CCr Fatigue Model

For the sake of completeness, the 3CCr model will be presented in this section, based on the description in [LHFL18].

The dynamic behavior of muscle fatigue is modeled using a compartment-based approach, dividing motor units into three activation states: resting (M_R), active (M_A), and fatigued (M_F). In theory, motor units develop fatigue continuously, and the force output decays over time. However, considering a group of activated motor units that develop fatigue continuously is mathematical equivalent to a mixture of activated motor units producing full tension and fatigued motor units producing zero tension [XL08]. The dynamic behavior between the states is described with the fatigue rate F, the recovery rate R, and the bi-directional, time-varying muscle activation-deactivation drive $C(t)$:

$$\frac{dM_A}{dt} = C(t) - F \cdot M_A(t), \tag{5.1}$$

$$\frac{dM_R}{dt} = -C(t) + R \cdot M_F(t), \tag{5.2}$$

$$\frac{dM_F}{dt} = F \cdot M_A(t) - R \cdot M_F(t). \tag{5.3}$$

The three compartments, M_A, M_R, and M_F, shown in Fig. 5.1, are given in percentage of the maximal force capacity (%MVC) and sum up to 100 %MVC. As M_A represents the active force-generating motor units, it is proportional to the force output. If all motor units are activated, the maximal force, denoted as MVC, is generated and the compartment M_A makes up 100 %MVC. If fatigue occurs or a lower force is required, there are also resting and fatigued motor units resulting in a lower M_A and a lower force output.

The activation-deactivation drive $C(t)$ describes the neuromuscular system controlling the size of M_A to produce the required force, which is denoted as *target load* (TL), given in %MVC. Thus, $C(t)$ is modeled as a bounded proportional controller, as described by

$$C(t) = \begin{cases} L_D(TL - M_A) & \text{if } M_A < TL \;\&\; M_R > TL - M_A \\ L_D M_R & \text{if } M_A < TL \;\&\; M_R < TL - M_A \\ L_R(TL - M_A) & \text{if } M_A \geq TL, \end{cases} \tag{5.4}$$

to generate M_A depending on the target load and the availability of M_R. The dimensionless development factor L_D and relaxation factor L_R ensure good system behavior and are set to 10, as suggested in [XL08].

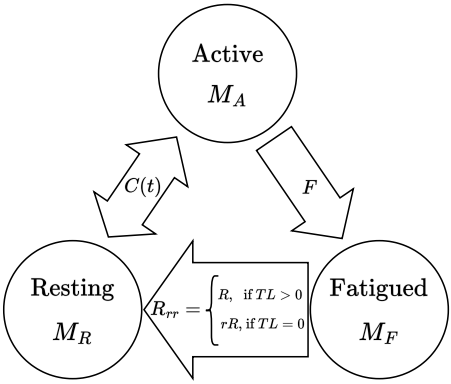

Figure 5.1: 3CCr fatigue model adapted from [LHFL18]. (© 2024 IEEE)

The rest recovery factor r, representing muscle reperfusion, and hyperemia effects, influences the recovery behavior during rest by scaling the recovery rate R. This behavior depends on the target load as follows:

$$R_{\mathrm{rr}} = \begin{cases} R, & \text{if } TL > 0 \\ r \cdot R, & \text{if } TL = 0 \end{cases} \tag{5.5}$$

The remaining muscle strength is represented by the *residual capacity* (RC) and can be expressed by:

$$RC(t) = M_A + M_R = 100\,\%\mathrm{MVC} - M_F. \tag{5.6}$$

If the muscle is not fatigued and has full capacity to generate force, the residual capacity is 100 %MVC. In contrast, an residual capacity of 0 %MVC indicates no strength reserve. Muscle fatigue, characterized by a reduction in maximal capacity to generate force, is directly described by the residual capacity. The residual capacity is influenced by both the fatigue and recovery behavior of the MUs and the associated target load.

Xia et al. described muscle fatigue on joint level and incorporated the complex force-velocity and force-length relation of a muscle [XL08]. Modeling fatigue on joint level overcomes the problem of muscle redundancies in synergistic muscle groups as multiple muscles contribute to one specific joint movement, e.g., hip extension. The target load input is generated by normalizing the task-specific torques with the maximum joint torque.

The maximum joint torque $\tau_{\max}$ is defined as the sum of passive torques τ_p produced by tendons and ligaments and active torques τ_a produced by muscle tension:

$$\tau_{\max} = \tau_p(\varphi) + \tau_a(\varphi, \dot{\varphi}) \tag{5.7}$$

The passive torque only depends on the joint angle φ, while the active torque depends on the joint angle, movement direction (sign of joint velocity $\dot{\varphi}$), and the contraction type. A positive velocity indicates concentric contraction and a negative velocity indicates eccentric contraction. Anderson et al. have mathematically described the force-velocity and force-length relation of the muscles for the lower limbs [AMN07]. As an example, the resulting *torque-velocity-angle* (TVA) surface for knee extension is illustrated in Fig. 5.2.

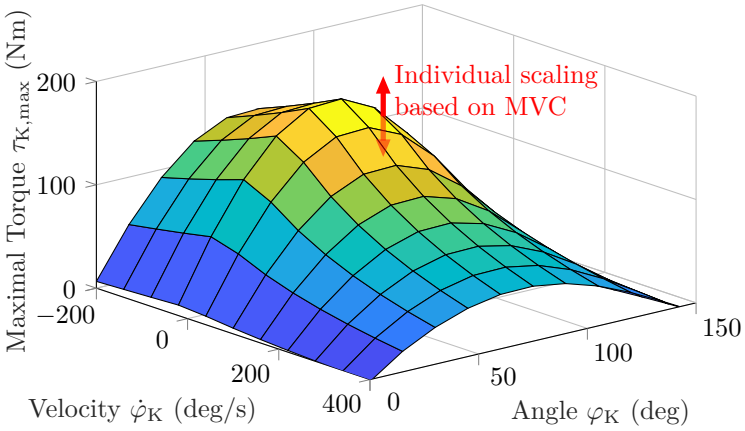

Figure 5.2: TVA surface representing the maximal torque of the knee extension depending on the joint angle and the angular velocity. Data from [AMN07]. (© 2024 IEEE)

The torque-velocity-angle relations differ not only for each joint and each joint movement [AMN07] but also for each test subject. To obtain the individual maximal torque for every test subject during the parameter estimation of the study, the torque-velocity-angle surfaces were scaled based on the individually measured MVC τ_{MVC} with the corresponding joint angles (Hip: $\varphi_H = 0°$, Knee: $\varphi_K = 90°$) and a velocity of $\dot{\varphi} = 0\,°/\text{s}$ as visualized by the red arrow in Fig. 5.2. It should be noted that the passive torque is neglected during the scaling approach. However, this approximation is permissible as it is relatively small compared to the active torque.

The individual torque-velocity-angle surface allows the calculation of the dynamic target load by normalizing the task-specific joint torque τ_{task} with the maximal torque $\tau_{\max}$ obtained by the torque-velocity-angle curve:

$$TL(t) = \frac{\tau_{\text{task}}(t)}{\tau_{\max}(\varphi_{\text{task}}, \dot{\varphi}_{\text{task}})}. \tag{5.8}$$

The joint torques $\tau_{\text{task}}(t)$ during the walking task can be obtained, e.g., by using inverse dynamics and can be mapped to the torque-velocity-angle curve by taking the angle φ_{task} and angular velocity $\dot{\varphi}_{\text{task}}$ into account. The resulting target load serves as the input to the fatigue model.

5.2.3 Muscle Activation

As described in Sec. 2.1.2, several muscle groups work together to perform certain movements during dynamic tasks. As for walking, predominantly the muscle groups responsible for the movements of the hip, knee, and ankle joints contribute to the human gait. In this work, the focus is set on the hip and knee joints because these joint torques can be assessed and actively supported by many common lower limb exoskeletons. The main muscle groups (see Fig. 2.2) contributing to the walking motion are the *gluteus maximus* (GM) (hip extension), the *iliopsoas* (IP) (hip flexion), the *quadriceps femoris* (QF) (knee extension), and the *hamstrings* (HS) (knee flexion). Muscle activation during gait is a complex sequence of alternating concentric and eccentric contractions of different muscle groups. As proposed in [SCB+16, CFLN+20], muscle activation can be determined by splitting the joint torque into positive and negative torques. In Tab. 5.1, the allocation of positive and negative joint torque and the corresponding muscle groups, neglecting co-contraction, are shown.

Table 5.1: Muscle activation during gait depending on the joint torque.

Joint	$\tau > 0$	$\tau \leq 0$
Hip joint	IP active	GM active
Knee joint	QF active	HS active

This torque-movement dependency can be described by modeling fatigue development separately for the GM, IP, QF, and HS muscle groups. During phases of activation, the muscle group develops fatigue while it recovers during inactivity and rest periods. As a consequence, the model parameters fatigue F, recovery R, and rest recovery r must be estimated for GM, IP, QF, and HS, respectively.

5.2.4 Parameter Estimation Study

The development of fatigue and recovery behavior is strongly dependent on the task, as different types of motor units are recruited based on the intensity [MHH13] (see Sec.2.1.2). Moreover, the development of fatigue and recovery is joint-dependent because active muscle groups differ in size and their composition of motor unit types [FLLH12]. Thus, the 3CCr fatigue model needs to be parameterized particularly for walking and cannot be adopted from the literature.

Experimental Setup

The experimental setup for the parameter estimation consisted of the *lower limb exoskeleton with serial elastic actuators* (L^2Exo-SE), a treadmill, and a test bench to measure the maximal torque of different joints. Moreover, physiological sensors were used to measure the metabolic cost and the HR of the test subject. The experimental setup is shown in Fig. 5.3.

All measurements were conducted using the L^2Exo-SE introduced in Sec. 3.2. The assistance factor k of the human-cooperative control strategy introduced in chapter 4 is of special interest for this chapter, as it is later the manipulative variable of the HiL control. As a reminder, this factor determines the extent of the exoskeleton's support as a percentage of the estimated human torque. For instance, an amplification factor of $k = 0.4$ implies that the exoskeleton contributes 40% of the total human's estimated torque. Moreover, to enhance the patient's comfort during walking, the exoskeleton's weight can be compensated.

MVC measurements were chosen as the assessment method for fatigue for two reasons. Firstly, MVC measurements have been described as the 'gold-standard' [GLK00, KANP02] to assess muscle fatigue. Secondly, as the MVC is generated voluntarily, it is an integration of all possible effects inducing fatigue. Thus, central limitations such as reduced motivation or imbalanced homeostasis responsible for perceived fatigability, as well as peripheral limitations such as reduced blood flow and impaired calcium kinetics resulting in performance fatigability are taken into account. The MVC test bench (Fig. 5.3, right) is used to measure the maximum isometric torque of the hip and the knee joint. It is equipped with a torque sensor (DR-2477-P, Lorenz Messtechnik GmbH, Alfdorf, Germany) with a measuring range of $\pm\,200\,\mathrm{Nm}$. A fixed chair allows the test person to sit while the torque of knee extension and knee flexion can be measured. A vertical aluminum profile provides stability to the standing person while the hip flexion and extension torque is measured. The other side of the shaft is fixed to avoid a rotation of the shaft. Thus, movements of the joints are restricted to measure the isometric MVC.

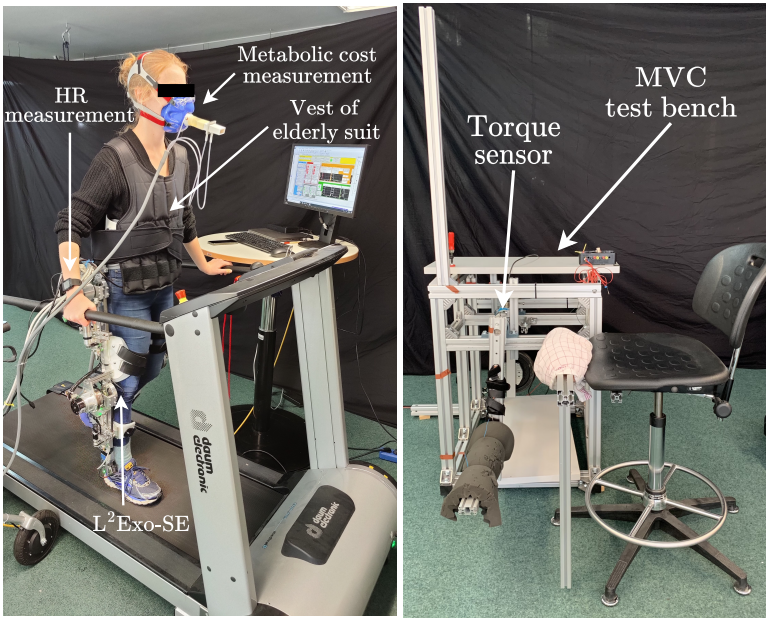

Figure 5.3: Experimental setup. Left: Test subject during a fatiguing session including the L^{2}Exo-SE, treadmill, and physiological sensors. Right: Test bench with torque sensor. (© 2024 IEEE)

Another method to assess fatigue is using subjective ratings. Although they are characterized by low validity and reliability due to the influence of many factors, they are important to estimate muscle fatigue correctly [MBCZ08]. Many authors state that *If the person tells you that he/she is loaded and effortful, then he/she is loaded and effortful whatever the behavioral and performance measures may show* [LB99]. Thus, combining subjective and objective measures reduces the conflicting problem and also relates to the taxonomy of Enoka et al. describing fatigue as a self-reported syndrome derived from perceived and performance fatigability [ED16]. The linear relation between the decline in MVC and the subjective ratings of perceived fatigue (scale from 0 to 10) shown by Whittaker et al. [WSP19] and used by Jang et al. [JSAR17] to perform the parameter estimation of the 3CC fatigue model gives an idea of how to combine both methods. For this reason, the RPF scale was included in the measurement protocol to evaluate fatigue on a subjective and objective level. The detailed

RPF scale is given in the appendix in Tab. A.1.

Lastly, the measurement of the HR and *energy expenditure* (EE) was included to evaluate the exertion of the test subjects during activity and rest. The test subject's HR was measured using the Garmin watch Forerunner 35, including the HRM-Dual chest strap (Garmin, Schaffhausen, Switzerland). The oxygen consumption ($\dot{V}O_2$) and the carbon dioxide release ($\dot{V}CO_2$) were measured using the gas analyzer GANSHORN PowerCube-Ergo (GANSHORN Medizin Electronic GmbH, Niederlauer, Germany). Oxygen consumption can be converted to EE when taking body weight into account. For example, for a 70 kg person, one liter of oxygen consumption is equal to 5 kcal, hence 1 W is equal to 0.01435 kcal or 14 mL of oxygen [JSB90].

Subjects Description

The parameters were estimated in the context of a small study, in which six healthy test subjects performed a fatigue and recovery protocol including walking in the human-cooperative lower limb exoskeleton. The test subject group consisted of three female and three male participants (28.7 ($\pm$2.7) years old). The biometric data including a self-estimated level of fitness on a scale from 0 to 10 (0 = not sportive, 10 = professional athlete) is provided in Tab. 5.2. The experimental self-test was cleared by the ethics committee of the Medical Faculty of RWTH Aachen University under the number EK264-21.

Table 5.2: Information of test subjects. (© 2024 IEEE)

Subject	Gender	Age	Height (m)	Weight (kg)	Fitness level
1	male	28	1.81	62	7-8
2	male	32	1.79	72	7
3	male	30	1.70	66	7
4	female	24	1.68	56	6
5	female	29	1.65	62	3
6	female	29	1.70	65	4

Measurement Protocol

The experimental protocol was split into two days, including one day to fit the exoskeleton and get used to walking with the exoskeleton and to the MVC measurement test bench. On the second day, the fatigue and recovery experiment was conducted. It consisted of a warm-up phase, four fatiguing sessions (each

15 min), two recovery sessions (each 15 min), and MVC measurements between the sessions. An overview of the measurement protocol is given in Fig. 5.4.

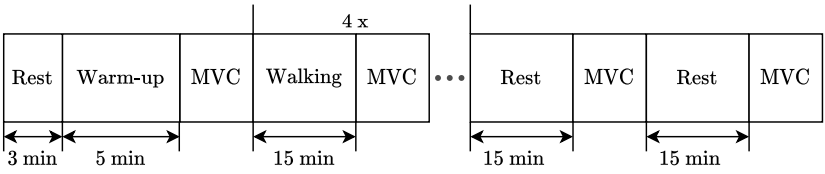

Figure 5.4: Measurement protocol for the parameter estimation. (© 2024 IEEE)

After completing the preparations, the subject was asked to perform resting measurements for 3 min to assess the resting heart rate and the resting energy expenditure while quietly standing. Ma et al. stated that a warming-up period of 3 min can increase the force capacity of one muscle group [MCBM12]. However, Samaan et al. [SWH+16] proposed a warm-up of 10 min. As a trade-off, a 5 min warm-up phase, composed of walking with zero-torque control and a speed of 1.3 km/h, was included in the beginning of the experiment. The same walking speed was maintained throughout the experiment.

Inducing fatigue is fundamental for developing a fatigue model. Although people with hemiplegia or other pathological disorders experience fatigue as a symptom during daily activities and rehabilitation, healthy people are able to maintain low-intensity tasks such as walking for several hours [MHH13]. To accelerate the process of fatigue development during the experimental protocol, the exoskeleton was used not as an assisting device but as a training device by applying negative assistance factors k for the patient-cooperative control resulting in increased resistance during walking. The exact assistance factors k were chosen heuristically (Hip stance phase: 0; Hip swing: -0.2; Knee stance: -0.1; Knee swing: -0.5) to allow resistance while maintaining the motor's control capabilities. Moreover, the weight of the exoskeleton and an additional vest of an aging simulation suit (GERT, Produkt + Projekt Wolfgang Moll, Niederstotzingen, Germany) weighing 10 kg contributed to the inducement of fatigue and simulated the muscle weakness of people with hemiplegia.

The measurements of MVC were conducted on the test bench (see Fig. 5.3). According to the developed fatigue model, each muscle group responsible for movements of the hip and knee joint has its own fatigue and recovery parameter. Thus, one MVC measurement phase consisted of four movements, measuring the maximum force during hip and knee extension and flexion. All joint movements were conducted on the same test bench during the MVC measurement phase to save time and avoid any structural modifications. Thus, the hip extension

and the hip flexion were measured while the subject was standing upright, keeping balance by holding the vertical aluminum profile depicted in Fig. 5.3. The misalignment of the hip joint and the rotational axis of the torque sensor were compensated using the lever arm principle. The MVC measurements were executed for each joint movement three times for 3 s to 5 s with a break of 5 s to 10 s. The instructor gave the command to start and stop the MVC while the test subject was verbally encouraged to exert the maximum force. In [Vøl97], Vøllestad stated that central limitations can be reduced with verbal encouragement. During the execution of the MVC measurements, the zero-torque control of the exoskeleton was enabled.

5.2.5 Parameter Estimation

The fatigue and recovery parameters can be obtained by fitting the recorded target load (model input) and MVC (measured output) with the fatigue model. Frey-Law et al. described the process of solving for the model parameters with numerical methods and investigated the use of fewer MVC assessments [FLSU21]. The fatigue model parameter for intermittent sub-maximal contractions can be determined using, e.g, the Levenberg-Marquardt algorithm, which computes the best-fit solutions for the minimal least squares difference between the measured and modeled data as introduced in Sec. 2.3.2. The different methods to reduce the number of MVC assessments, e.g., using only MVC measurements in the beginning and at the end of the fatigue development, have proven effective if later fatigue behavior is captured. For this case, the MVC assessments were chosen to be distributed equally to capture the overall fatigue development during the protocol as the later fatigue behavior cannot be guaranteed with one hour of walking. The start parameters of F, R, and r were determined heuristically based on parameters provided in [LHFL18]. The algorithm searched for minimal error until the termination criterion (convergence with 0.0001 optimality tolerance or 100 iteration steps) was reached.

5.3 Human-in-the-Loop Fatigue Control

Leveraging the existent joint and subject-specific fatigue models, the possibility of not only estimating but also controlling fatigue using the exoskeleton's assistance is proposed. To test this hypothesis, a control system for fatigue is presented, which is an extension of the patient-cooperative exoskeleton control described in chapter 4.

The proposed overall control is visualized in Fig. 5.5. The individual blocks are explained in more detail in the following sections. The control system is

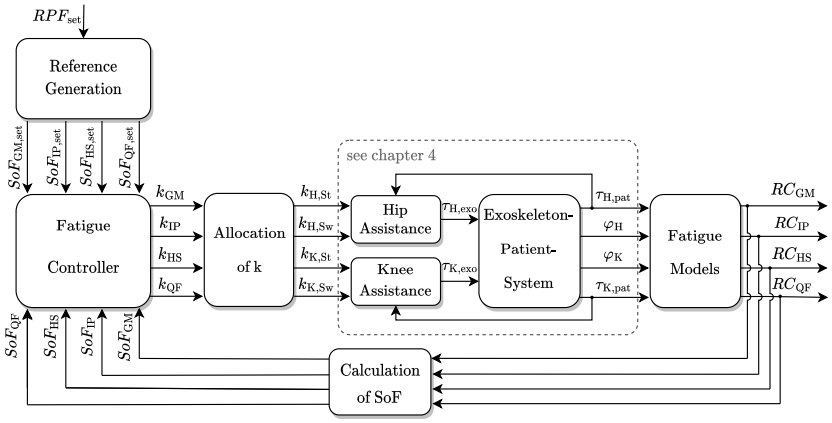

Figure 5.5: Control loop of the HiL control incorporating fatigue. (© 2024 IEEE)

designed and validated based on the fatigue model for subject 1 (parameters see Tab. A.2).

5.3.1 Reference Generation

First, it is necessary to define the reference variable which is being controlled. The residual joint strength, denoted as residual capacity, describes the development of muscle fatigue. However, every muscle has a different residual capacity threshold, at which it can theoretically maintain the force infinitely long. Moreover, Enoka et al. define fatigue as a self-reported symptom derived from an interaction of perceived and performance fatigability [ED16]. The intensity of the objective measures, such as the MVC decline, can only be rated by the perceived fatigue as, for example, one person experiences more fatigue with the same MVC decline than another person. Additionally, it is more intuitive to use the ratings of perceived fatigue to define the level of fatigue than to define the reference residual capacity for every muscle group. Due to these reasons, the *state of fatigue* (SoF) combined with the RPF is used to generate the reference RPF_{set}.

The SoF was introduced by Fayazi et al. and is defined as the decline in force capacity normalized with the threshold force capacity, at which the muscle can maintain the force for a very long time [FWL+13]. The motor unit-based fatigue model can be transformed to the SoF by:

$$SoF = \frac{100\,\%MVC - RC}{100\,\%MVC - RC_{\text{th}}}. \tag{5.9}$$

The SoF index describes fatigue with an index between 0 and 1. An SoF of 1 (100%) indicates that the individual is maximally fatigued and can only exert a force equal to the threshold residual capacity (RC_{th}). An SoF of 0 indicates that the muscle is not fatigued and has 100 % of its residual capacity. According to Liu et al., the threshold residual capacity can be determined by [LBY02]:

$$RC_{\text{th}} = \frac{R_{\text{rr}}}{F + R_{\text{rr}}} \cdot 100\,\% \ . \tag{5.10}$$

However, the dynamic task of walking is seen as an intermittent muscle activation with a different recovery factor during rest. For this reason, the rest recovery factor r was integrated into the calculation of RC_{th} by estimating the duty cycle of muscle activity and rest periods during one gait cycle. The active phase can be denoted as $\alpha = t_{\text{active}}/t_{\text{cycle}}$ while the resting phase may be expressed by $\beta = t_{\text{rest}}/t_{\text{cycle}}$. The modified calculation of RC_{th} during dynamic tasks is:

$$RC_{\text{th}} = \frac{\alpha \cdot R + \beta \cdot rR}{F + (\alpha \cdot R + \beta \cdot rR)} \cdot 100\,\% \ . \tag{5.11}$$

The variables α and β, expressing the duty cycle, were determined offline by evaluating 60 gait cycles of subject 1 and taking the average of the active and resting time intervals divided by the gait cycle time. In theory, it is also possible to update the duty cycles online. The duty cycle values and the corresponding RC_{th} for subject 1 are presented in Tab. 5.3.

Table 5.3: Averaged duty cycles during one gait cycle and the corresponding RC_{th} of subject 1. (© 2024 IEEE)

Muscle group	α	β	RC_{th} [%MVC]
GM	0.2409	0.7691	18.45
IP	0.7938	0.2062	28.56
HS	0.5822	0.4178	28.21
QF	0.4750	0.5250	20.68

The SoF represents a comparable objective measure representing the development of muscle fatigue. Additionally, the ratings of perceived fatigue can rate the objective measure with the subjective feeling of fatigue, making the reference value more intuitive. Whittaker et al. found a linear relationship between the RPF, expressed by a modified Borg CR-10 scale, and the MVC

decline [WSP19]. Thus, by linear regression between the RPF values and the SoF values calculated from the residual capacity values, it is possible to provide an RPF value as a set point (RPF_{set}) for this control strategy. The derived linear relation enables the translation of a reference RPF into a reference SoF for each *muscle group* (MG) through

$$SoF_{\mathrm{MG,set}} = m_{\mathrm{MG,set}} \cdot RPF_{\mathrm{set}} \text{ with MG} \in (\mathrm{GM, IP, HS, QF}) \tag{5.12}$$

and $m_{\mathrm{GM}} = 0.07$, $m_{\mathrm{IP}} = 0.09$, $m_{\mathrm{HS}} = 0.084$, $m_{\mathrm{QF}} = 0.093$ for subject 1.

5.3.2 Fatigue Controller

The fatigue controller aims to control the SoF by changing the assisting factors of the exoskeleton's control during stance ($k_{\mathrm{H,St}}$, $k_{\mathrm{K,St}}$) and swing phase ($k_{\mathrm{H,Sw}}$, $k_{\mathrm{K,Sw}}$) for the *hip* (H) and *knee* (K) joint. The goal is to reach a specific fatigue level throughout the training session. Theoretically, this can be accomplished by evaluating the steady-state of the system, which should approach the predefined target SoF level. Changing the amplification factors allows to control the patient's effort and, thus, the fatigue development. A control strategy based on a *feed-forward* (FF) control and a feedback proportional controller is suggested as depicted in Fig. 5.6.

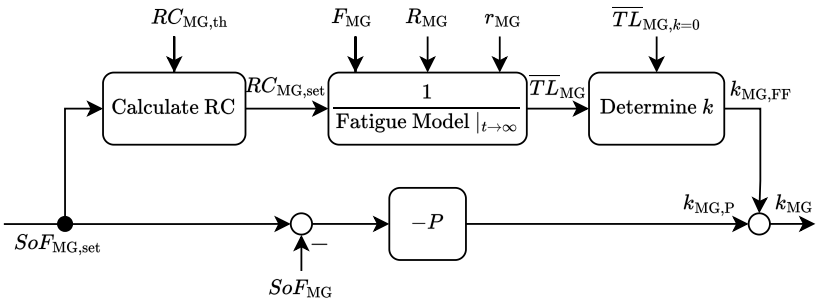

Figure 5.6: Fatigue controller for each muscle group (MG) consisting of a feed-forward (FF) term and a feedback term. (© 2024 IEEE)

The feed-forward control uses the fatigue model, to estimate an ideal amplification factor to reach the target SoF. In addition, the proportional controller compensates for disturbances and model errors. An integral behavior is not considered because the development of fatigue has a very slow dynamic behavior

and large time constants. It is important to note that this choice can lead to non-zero steady-state errors.

The feed-forward term uses the steady-state value of the inverse of the fatigue model to obtain a required averaged target load (TL_{mean}), which results in given residual capacity (RC_{set}). For this, a transfer function of the fatigue model was derived under the assumption that the required target load can always be generated. In this case, the activation-deactivation drive $C(t)$ in eq. (5.4) can be reduced to:

$$C(t) = 10 \cdot (TL - M_A) \ . \tag{5.13}$$

Furthermore, considering the fatigue model eqs. (5.1) - (5.3), (5.5), (5.6), the following transfer function can be derived:

$$G(s) = \frac{RC(s)}{TL(s)} = \frac{-10 \cdot F \cdot s}{s^3 + s^2 \cdot (10 + F + R_{\text{rr}}) + s \cdot R_{\text{rr}} \cdot (10 + F)} \ . \tag{5.14}$$

The initial condition of $RC(t = 0) = RC_0 = 1$ (fully recovered) can be incorporated by:

$$RC(s) = G(s) \cdot TL(s) + RC_0 \ . \tag{5.15}$$

The required averaged target load to achieve a given residual capacity can be obtained by calculating the steady-state of the inverse of this system using the final limit theorem. Additionally, the rest recovery factor r was included similarly as in the calculation of RC_{th} (see eq. (5.11)). Thus, the inverse fatigue model in steady-state for the dynamic task of walking is:

$$\begin{aligned} \overline{TL} =& \frac{1}{\text{Fatigue Model } |_{t\to\infty}} = \lim_{s\to 0} s \frac{1}{G(s)} \frac{RC_{\text{set}} - RC_0}{s} \\ =& \frac{-R_{\text{rr}} \cdot (10 + F)}{10 \cdot F} (RC_{\text{set}} - RC_0) \\ \xRightarrow[\alpha R + \beta r R]{R_{\text{rr}} \approx} & \overline{TL} \approx \frac{-(\alpha \cdot R + \beta \cdot rR) \cdot (10 + F)}{10 \cdot F} (RC_{\text{set}} - RC_0) \ . \end{aligned} \tag{5.16}$$

With the average target load $\overline{TL}$ for each muscle group[1], that is necessary to achieve a given residual capacity, the feed-forward amplification factor k_{FF} can be determined by

$$k_{\text{MG, FF}} = 1 - \frac{\overline{TL}_{\text{MG}}}{\overline{TL}_{\text{MG, k=0}}}, \tag{5.17}$$

where $\overline{TL}_{\text{MG, k=0}}$ is the target load during walking with an amplification factor of $k = 0$, which was obtained from experimental data for each muscle.

[1]The index for each muscle group in eq. (5.16) is neglected for readability.

The additional proportional controller requires a negative gain, as a negative error should lead to an increase in the amplification factor to increase the assistance. The corresponding feedback amplification factor $k_{\mathrm{MG},P}$ is described by:

$$k_{\mathrm{MG},P} = -P \cdot (SoF_{\mathrm{MG,set}} - SoF_{\mathrm{MG}}) \ . \tag{5.18}$$

A gain of $P = 5$ was chosen heuristically as it provided amplification in a reasonable range.

The sum of the feed-forward and feedback amplification factor results in the assistance factor $k_{\mathrm{MG}} = k_{\mathrm{MG,\ FF}} + k_{\mathrm{MG},P}$ for each muscle group.

5.3.3 Allocation of Assistance

The assisting factor for each muscle group was forwarded to the exoskeleton's assistance control depending on the gait phases. Ideally, the assistance factor is supposed to switch between the agonist and antagonist muscle depending on the sign of the joint torque as described in Tab. 5.1. However, this might lead to discomfort for the subject while walking. For that reason, the number of different assisting factors was reduced in a second approach by calculating the mean amplification factor for each joint, that is for the hip $k_{\mathrm{H}} = \frac{k_{\mathrm{GM}}+k_{\mathrm{IP}}}{2}$ and the knee $k_{\mathrm{K}} = \frac{k_{\mathrm{HS}}+k_{\mathrm{QF}}}{2}$. Note that the assisting factor might differ between the stance and swing phases due to different lower and upper boundaries resulting from hardware and control restrictions.

5.4 Results and Discussion

The results of the system identification study as well as the control validation are presented in the following.

5.4.1 Results Fatigue Model

MVC measurements

The averaged and individual MVC measurements of all subjects during the parameter identification experiments for all four considered muscle groups are visualized in Fig. 5.7. On average, the MVC for the different muscle groups decreased during the fatigue session by 17.5 (±12.5)% (GM), 14 (±12)% (IP), 17.6 (±8)% (HS), and 19.8 (±12.2)% (QF), respectively. During the last 30 min of the experiment they recovered to 5.4 (±8.3)% (GM), 5 (±9.4)% (IP), 2.5 (±5.8)% (HS), and 7.9 (±7.5)% (QF) total MVC decline. The individual MVC losses reached up to a maximum of -38.9% (subject 2, QF). However,

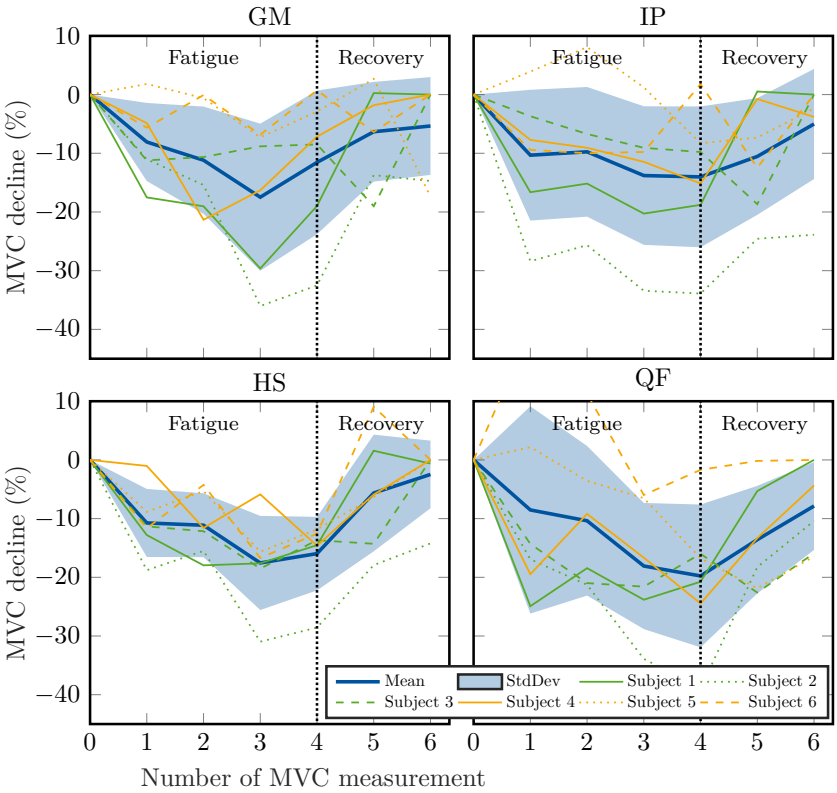

Figure 5.7: Average and individual MVC decline during the experiment for all subjects of the four different muscle groups: GM (left), IP (second left), HS (second right), and QF (right). The time between two consecutive MVC measurements was approximately 15 minutes. (© 2024 IEEE)

MVC increased of up to 22.3% (subject 6, QF) were also observed in a few cases. Possible reasons for an increase in MVC are discussed in section 5.4.3.

Perceived Fatigue

The ratings of perceived fatigue values (on a scale from 0 to 10) reported by the participants during the experiment are shown in Fig. 5.8. On average, a maximum RPF of 3 ($\pm$0.9) was achieved during the fatigue session. The

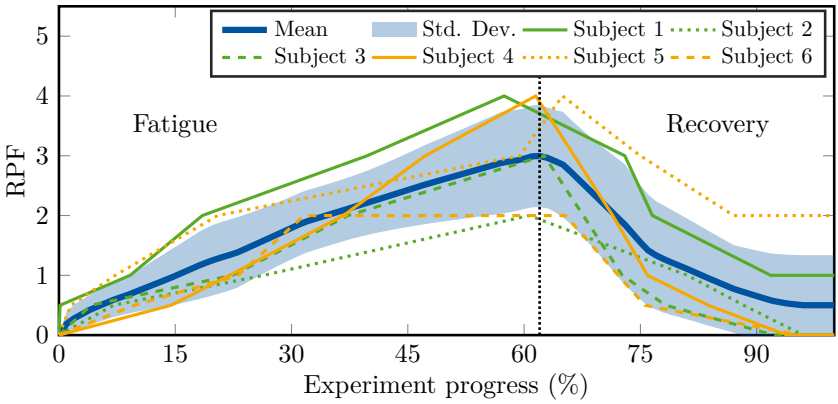

Figure 5.8: The RPF reported by the participants during the experimental procedure. Note: The x-axis displays the experimental progress (%) as the total time varied slightly between trials. (© 2024 IEEE)

maximum RPF of 4 was reported by three participants at the end of the fatigue session. During the recovery session, the average RPF decreases to 0.5 (±0.8).

Physiological Measures

The energy expenditure during the fatigue session ranged from 153 W (subject 6) to 289 W (subject 1) with an average maximum of 206 W among all subjects. On average, the EE was 3.03 (±0.49) times higher during walking than during rest. During the fatiguing session, the HR increased on average by 17.6 (±7.3)% with a minimum increase of 7.5 *beats per minutes* (bpm) for subject 2 and a maximum increase of 21 bpm for subject 1.

Identified Model

The target load of the GM muscle group of subject 1 during the experiment and the 7 MVC measurements are visualized in Fig. 5.9. Based on the target load (input), recorded by the exoskeleton, and the MVC measurements the fatigue model parameters could be identified for the GM of subject 1 and, consequently, calculate the residual capacity of the GM for the entire time of the experiment as visualized by the red curve in Fig. 5.9. The modeled residual capacity decreases during the fatigue session and fully recovers at the end of the experiment. The *mean absolute error* (MAE) between the modeled residual

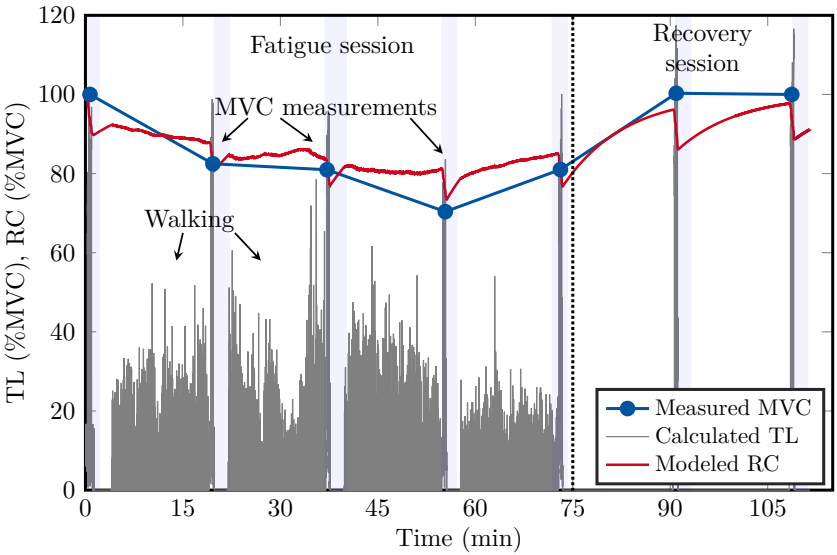

Figure 5.9: Measured MVC (blue) and calculated target load (TL, grey) for the GM muscle of subject 1 for the entire experimental procedure including fatigue and recovery session. Additionally, residual capacity (RC, red) based on the fitted fatigue model.

capacity and the measured MVC in this particular case is 4.33 %MVC.

Similarly, the fatigue model parameters could be determined for all considered muscle groups of all subjects. The mean model parameters including the standard deviation among the participants are listed in Tab. 5.4. Additionally, the table provides the average MAE between the modeled and measured residual capacity in %MVC. The individual model parameters are provided in the appendix in Tab. A.2.

5.4.2 Control Validation

The fatigue controller was validated both through simulation and experimental testing.

Table 5.4: Averaged model parameters of all participants. (© 2024 IEEE)

Muscle	F (/s)	R (/s)	r (-)	MAE (%MVC)
GM	0.00328 (±0.00238)	0.000047 (±.000036)	18.34 (±5.86)	5.61 (±2.64)
IP	0.00103 (±0.00081)	0.000174 (±0.000225)	14.89 (±6.30)	4.33 (±2.57)
HS	0.00158 (±0.00078)	0.000097 (±0.000051)	16.01 (±5.98)	3.81 (±1.45)
QF	0.00262 (±0.00201)	0.001180 (±0.002340)	7.20 (±6.41)	6.00 (±1.90)

Simulative Validation

The simulation aimed to validate the control concept under ideal conditions, considering a 2-hour time frame. During the first hour, the ratings of perceived fatigue reference value was set to $RPF_{\text{set}} = 2$, subsequently, it was increased to $RPF_{\text{set}} = 2.5$ to observe the controller's response to a reference value change. These values were chosen to ensure reasonable amplification factors and rising times for experimental validation in the next subsection.

The simulation did not consider the full dynamic model of the exoskeleton and test subject. Instead, the input for the simulation was taken from a repeating 1-minute walking sequence, which was amplified based on the selected exoskeleton's assistance factor to account for the varying target load. It should be noted that the simulated data and averaged target load value for the FF loop are only valid under the same conditions as in the parameter estimation.

Three simulations were conducted: One with amplification factors alternating between agonist and antagonist muscles, the second one using the mean assisting factor for each joint, and lastly the same simulation under the consideration of the exoskeleton's actuation limits. The simulation results for the knee joint (HS and QF) are presented in Fig. 5.10.

Using eq. (5.12), the two RPF reference values translate to $SoF_{\text{HS,set}} = 16.8\%$ and $SoF_{\text{QF,set}} = 18.6\%$ for $RPF_{\text{set}} = 2$ and to $SoF_{\text{HS,set}} = 21\%$ and $SoF_{\text{QF,set}} = 24.5\%$ for $RPF_{\text{set}} = 2.5$. To achieve these fatigue levels, the ideal assistance factor k_{HS} and k_{QF} start at -0.6 and -1, respectively, and slowly increase to almost 0 (transparent behavior) with increasing fatigue as depicted in the top graph of Fig. 5.10. With the increasing reference value, the assistance

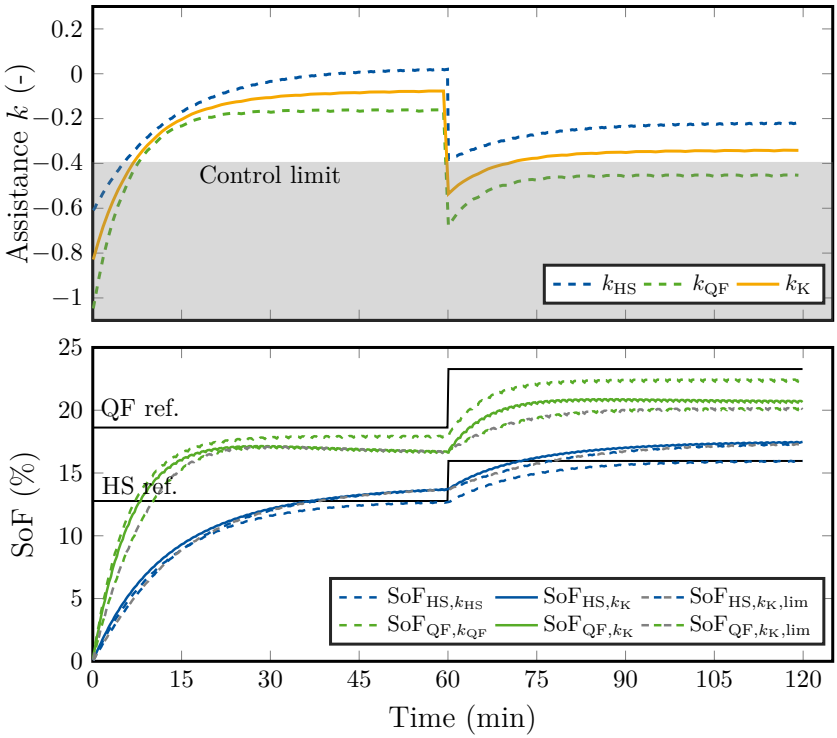

Figure 5.10: Simulation results. Top: Ideally calculated assistance factor k for HS (blue, dashed) and QF (green, dashed) and actual knee assistance factor (orange, solid) calculated as the mean value from ideal assistance factors. The gray area represents the experimental actuation limit. Bottom: SoF reference based on a RPF reference of 2 and 2.5 for HS and QF (black). Additionally visualized is the simulated SoF of the HS (blue) and the QF (green) using ideal assistance (dashed), the actual assistance (solid), and the actual assistance considering exoskeleton's actuation limits (gray, dashed). (© 2024 IEEE)

factors drop by about 0.4.

The steady-state error for the HS using the ideal assistance factors (switching between agonist and antagonist) becomes zero after approximately 40 min. For the QF, an absolute steady-state error of 1% remains at the end of the simulation. The simulation outcomes using the mean assistance factor for the knee k_K show slight differences compared to the first simulation. Specifically,

the fatigue level of the QF is 2.6% lower than the reference value, while that of the HS is 1.3% higher. This effect is increased for the QF under consideration of a minimal assistance factor of $k_{\mathrm{K}} = -0.4$. The simulation outcomes for the hip muscles are visualized in the appendix in Fig. A.3. They exhibit similar trends with the only difference that the actuation limits ($-0.25 \leq k_{\mathrm{H}} \leq 0.2$) for the hip motor cause a maximum error of up to 6%.

Experimental Validation

Fig. 5.11 shows the experimental validation procedure for the developed HiL controller. Initially, a reference value of $RPF_{\mathrm{set}} = 2$ was set for 35 min, followed by an increase to $RPF_{\mathrm{set}} = 2.5$ and 20 min of walking. As shown in Fig. 5.11, the experimental protocol included warm-up phases and MVC measurements between walking sessions, during which the fatigue controller and model were paused. This was justified because MVC measurements consist of alternating MVC and rest periods, assumed to cancel out fatigue and recovery effects, as shown in Fig. 5.9. During the experimental validation, only the averaged assisting factors (k_{H}, k_{K}) were applied.

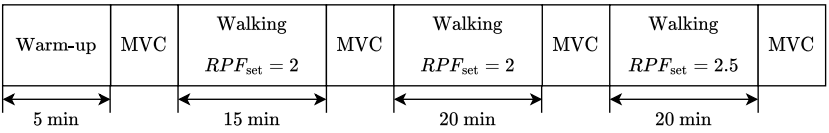

Figure 5.11: Measurement protocol for the validation of the fatigue controller. (© 2024 IEEE)

Fig. 5.12 (top graph, dashed lines) displays the ideal amplification factors for each muscle group, showing similar behavior to the simulated k-factors. However, the experimental amplification factors for the knee and hip (see appendix Fig. A.4) were larger than the ones during the simulation. Notably, during the second phase, k_{HS} was significantly larger in the experiment than in the simulation, creating a wider gap between HS and QF assistance. This was due to the larger SoF_{HS} values, leading to a more significant control error. The difference in muscle assistance also affected the averaged assistance value k_{K} applied to subject 1 during the experiment, resulting in a higher steady-state error (Fig. 5.12, bottom) compared to the simulation. A second factor attributing to the increased steady-state error was the saturation limit restricting positive support. Furthermore, it is essential to acknowledge the inconsistency noted in the last MVC measurement of Fig. 5.12. Potential explanations for this variance are discussed in the subsequent section.

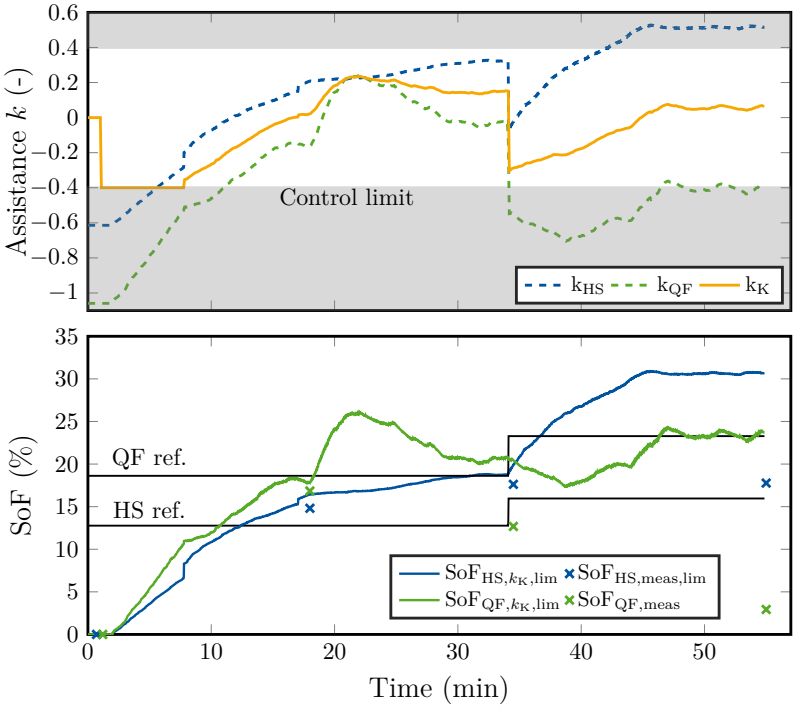

Figure 5.12: Experimental results. Top: Ideally calculated assistance factor k for HS (blue, dashed) and QF (green, dashed) and actual knee assistance factor (orange, solid) calculated as the mean value from ideal assistance factors and considering actuation limits. Bottom: Calculated SoF reference based on a RPF reference of 2 and 2.5 for HS and QF (black). Additionally visualized is the model-based determined SoF of the HS (blue) and the QF (green) during the experiment and the SoF for the HS (blue marks) and the QF (green marks) determined via MVC measurements. (© 2024 IEEE)

5.4.3 Discussion of the Fatigue Model

The occurrence of significant fatigue in all subjects during walking with the active exoskeleton resistance and the additional age suit vest is a key result of this study. The fatigue is indicated by both MVC measurements and subjective ratings of perceived fatigue and is further corroborated by increased HR and EE. The identified fatigue model parameters and further challenges and limitations

are described in the following.

Identified Model Parameters

The fatigue rates F of all muscle groups were found to range from $F = 0.001/\text{s}$ to $F = 0.0033/\text{s}$, which are approximately 10 times smaller than the knee's extension fatigue rate ($F = 0.015/\text{s}$) observed by Looft et al. [LHFL18]. The recovery rates R of the GM, IP, and HS are around $R = 0.0001/\text{s}$, and, thus, smaller than those investigated by Frew-Law et al. [FLLH12] and Looft et al. [LHFL18], which included joints like the knee, trunk, and ankle but not hip muscles.

The average recovery parameter of the QF responsible for knee extension was on average $\bar{R}_{QF} = 0.00118/\text{s}$, comparable to the literature value of $R = 0.00149/\text{s}$ [FLLH12, LHFL18]. However, this parameter might have been influenced by subject 6's unusually high recovery rate, leading to potential inaccuracies in parameter estimation. The high recovery rate of subject 6 can be explained by MVC increase after the first fatiguing session (see Fig. 5.7).

The estimated fatigue model's parameters were generally smaller compared to the literature, likely due to different muscle groups being investigated and the literature focusing on high-intensity contractions (only 14% low-intensity contractions) [LHFL18]. This highlights the need for new parameterization specific to the walking task, which is considered a low-intensity activity and may explain the lower fatigue rates observed in the conducted study.

The fatigue rates were also affected by the cycle time of muscle activation. Rashedi and Nussbaum found that more frequent and shorter rests induce less fatigue than the same force load with less frequent and longer rest periods [RN16]. The high frequent muscle activation during gait could contribute to the lower fatigue development in the model.

Furthermore, fatigue development depends on the interaction between fatigue and recovery rates, where higher fatigue rates combined with higher recovery rates or lower fatigue rates with lower recovery rates yield comparable results. The same holds for the rest recovery factor r. Looft et al. estimated the rest recovery factor of the knee joint to be $r = 15$ (knee extension) [LHFL18]. The estimated rest recovery rate in this thesis ranges from $r = 7.2$ to $r = 18.34$, making it comparable to the literature.

On average, the MAE between the modeled and measured residual capacity was approximately 5 %MVC, which aligns with findings in the literature. For comparison, Looft et al. observed estimation errors ranging from 5.7% to 9.9% torque decline, equivalent to the decline in %MVC [LHFL18]. Previous research has shown that the rest recovery factor significantly reduces the prediction error. Specifically, using the 3CC model, the prediction error for knee extensor

muscles was 21 %MVC, whereas the modified 3CCr model reduced the error to 8.6 %MVC [LHFL18]. It was possible to confirm this finding by the results of the presented study. Notably, some subjects' prediction errors of the presented study fall within a narrow range of 2 %MVC to 3 %MVC, which is relatively small compared to the literature. The higher accuracy may be attributed to the approach used in this study, where estimation errors were determined using individual model parameters for each subject, whereas the literature may rely on generalized model parameters, leading to higher prediction errors.

Experimental Challenges

This section discusses the practical challenges encountered in the experimental study, their implications on the results, and the possibility of generalizing the fatigue model for different populations.

Firstly, the posture during MVC measurements is crucial. However, defining the posture for hip extension and flexion is difficult compared to knee measurements when using the same test bench as in the presented setup (see Fig. 5.3). Bending and slight deviations occurred in the MVC test bench and exoskeleton, affecting joint angles and torque output. Despite efforts to standardize posture, variations in force output were observed among subjects. The hip MVC results showed more variability than knee flexion, possibly due to uncomfortable postures affecting maximal force exertion. The opportunity to measure the MVC of the hip muscles while lying, as in [DSBB+09], or in a more robust construction that needs to be reassembled to change between hip and knee joint, is challenging because of the exoskeleton. Additionally, the increase of MVC measurement time would result in more recovery during the MVC measurements that would counteract the fatigue development.

Another challenge was the fixation between the exoskeleton and test subjects, particularly due to anatomical differences among the test subjects. Misalignments triggered safety thresholds, causing interruptions during walking, which affected torque and fatigue estimation. Correct calibration of joint angles is essential as it directly affects the human torque estimation and, thus, the target load (model input). Additionally, the calculation of the target load is very sensitive to the measured angle due to the high gradient of the torque-velocity-angle surface at small angles (see Fig. 5.2), making the misalignment between the exoskeleton and the joints more crucial. Therefore, precise calibration of the target load and scaling of the TVA surface is essential to ensure consistent inputs and improved fatigue estimation based on identified parameters when integrating the fatigue model into the exoskeleton's HiL control.

Adapting to the exoskeleton and the MVC test bench over time, as well as warm-up effects, posed additional challenges. Warm-up can lead to an increase

of up to 15 %MVC while fatigue can decrease it. The warm-up phase of 5 minutes seemed sufficient for most subjects, but some showed increased MVC after the initial fatigue sessions (see Fig. 5.7), possibly due to adaptation or discomfort with the exoskeleton. These factors need careful consideration during experimentation.

Considering the study's generalization, the small number of healthy, young adult subjects raises questions about the model's applicability to other populations. On the one hand, influences, like motivation, homeostasis, or the psychological state, contribute to variations of individual fatigue development. On the other hand, patients with hemiplegia, incomplete SCI, and elderly individuals exhibit different fatigue development. For example, Dorneles et al. investigated the fatigue development of incomplete SCI patients after prolonged walking and came to the conclusion that they develop higher muscle fatigue than healthy control subjects [DNG+20]. Additionally, Knorr et al. found that the origin of neuromuscular fatigue is shifted to central limitations which might contribute to increased self-reported fatigue [KID+11]. For that reason, the presented experimental study alone cannot develop a generalized fatigue model, and repeating parameter estimations for various populations is recommended.

Despite these challenges, the adapted model and experimental protocol effectively assessed and modeled fatiguing and recovery behavior during exoskeleton-assisted walking.

Theoretical Limitations

The 3CCr model for walking with an exoskeleton has theoretical limitations that deviate from real fatigue development. These limitations include simplified muscle activation, neglecting co-contraction, and not considering muscle fiber composition, perceived fatigue, and physiological factors like homeostasis.

The first limitation is that the model only considers four specific muscle groups, excluding other contributing muscles like hip adductors and calf muscles. Additionally, co-contraction, common in patients with gait disorders, is not accounted for, potentially underestimating fatigue [Win09].

Secondly, muscle fiber composition, with Type I and Type II motor units, is not considered. While walking might recruit mostly Type I motor units, exoskeleton use could activate Type II motor units due to the resistive behavior, affecting fatigue. However, individualized parameters represent active motor units during exoskeleton walking, mitigating this concern.

Lastly, perceived fatigue and physiological mechanisms like homeostasis and the psychological state of the person are neglected. According to the 3CCr model, a muscle is able to maintain a force below a certain force limit infinitely long [Roh60]. During walking (a low-intensity task), the model assumes no

endurance time limit. However, in reality, after a couple of hours, homeostasis becomes unbalanced, causing increased core temperature and the need for hydration and food for energy. These effects are not considered by the fatigue model but could be integrated with a slowly decreasing gain through longer walking sessions. Additionally, the perceived fatigue has not been integrated into the fatigue model, but it was considered in the HiL control design.

5.4.4 Discussion of Controller Performance

The simulation results show that the developed HiL controller effectively controls the fatigue level with a maximal error of 1% under ideal conditions in the simulation. It is important to note that the saturation limits strongly influence the controller's performance, as they restrict the control action. The selected reference fatigue levels ($RPF_{\text{set}} = 2$ and $RPF_{\text{set}} = 2.5$) cause the amplification factors to spread over a wide range, making control of higher or lower ratings of perceived fatigue values more challenging. Using the mean of the agonist and antagonist's amplification factors results in higher steady-state errors, as the fatigue model and controller are designed to account for different dynamic behaviors for each muscle. However, tests have shown that using the mean amplification factors provides a more comfortable walking experience, while the switching k-factors lead to jerky support from the exoskeleton, potentially increasing fatigue development as the body adapts constantly to the switching amplification. Additionally, considering the high variations in the MVC measurements during the parameter identification, an error of 2.6% or 6% - taking actuation limits into account - is comparatively small. Thus, the simulation results justify the choice of the mean amplification factor used for the experimental validation.

The experimental validation demonstrated that the HiL controller effectively regulates the desired fatigue level by adjusting the exoskeleton's assistance. However, the controller's performance is significantly influenced by the saturation limits of the amplification factors and thus confirms the findings of the simulative validation. The experimental validation showed that the GM and QF muscles exhibit excellent control performance with minimal steady-state errors, while the IP and HS muscles are more constrained by the saturation limits, leading to steady-state errors of up to 15% relative to the SoF scale. Incorporating an integral component in the feedback control might help reduce the steady state error. However, tuning the integral gain is a challenge as even a slight increase in the integral gain can quickly result in amplification beyond the exoskeleton's control capacity.

The first three MVC measurements conducted during the experiment (Fig. 5.12) validate the intended fatigue in the two muscle groups. However, the last MVC

measurement of the QF muscle suggests recovery despite an increased target RPF. This discrepancy can be attributed to the higher support factor k_{K} compared to the ideal assistance k_{HS} and the considerable variance in the MVC measurements themselves (see Sec. 5.4.3).

Lastly, it is important to highlight that the controller was tested on only one individual. For future studies, it is recommended to expand the controller's validation by including more participants. Nevertheless, the results highlight the promising potential of integrating the developed fatigue model with the HiL controller in effectively controlling fatigue levels.

5.5 Summary

In this chapter, a fatigue model for walking with an exoskeleton with a corresponding HiL control mechanism for regulating fatigue levels was successfully formulated and validated. Utilizing the 3CCr fatigue model of Looft et al [LHFL18] and the torque-velocity-angle surface adaptations, the study captures intricate details of dynamic muscle activities. The experimental validation of the model parameters confirmed its predictive accuracy for MVC decline. Furthermore, the developed HiL control system, incorporating perceived fatigue and fatigue level metrics (RPF and SoF), effectively regulated the fatigue level within acceptable steady-state error ranges. However, the saturation limits of the amplification factors influenced control performance, indicating areas for further refinement. The integration of the fatigue model into the HiL control system demonstrates the potential for improved management of fatigue levels in patients using exoskeletons. This represents a promising advancement in assistive technology, paving the way for enhanced, personalized user experiences in exoskeleton applications.

6 Conclusion and Outlook

Traditional rehabilitation places significant demands on therapists and is typically limited to a therapeutic environment [Reh20]. However, for optimal results, early and intensive rehabilitation, such as home-based training, is crucial. A wide range of individuals, including the elderly, those with post-polio syndrome, multiple sclerosis, and *spinal cord injury* (SCI), particularly benefit from rehabilitative interventions in everyday life [YF17]. Given the undeniable importance of early and consistent rehabilitation, especially after a stroke with paresis as a symptom, to restore mobility [MP12], novel approaches to facilitate rehabilitation are urgently needed. Lower limb exoskeletons offer a promising solution. Yet, existing exoskeletons suffer from limitations, especially with regard to facilitating patient-initiated movements throughout the entire gait cycle, which is critical for rehabilitation [Bin88, MP12]. Furthermore, the integration of safety features, notably compliant actuators with varying serial elasticity, is often restricted to isolated motion sequences.

To address these challenges, the first central contribution of this dissertation is the development of a unilateral exoskeleton equipped with *variable stiffness actuators* (VSAs) to support both the knee and the hip. The VSAs enable a real-time modification of coupling properties to adapt to different gait phases and environmental demands. Secondly, a new system identification process is introduced to not only assess the device's dynamic behavior but also derive the individual's lower limb model dynamics. The detailed knowledge of the subject's leg movements is employed to develop a real-time motion intention estimation using an *unscented Kalman filter* (UKF), ensuring accuracy and reliability. Furthermore, a novel patient-cooperative control strategy is formulated that provides either assistance or resistance throughout the gait cycle and during transitional movements such as *sit-to-stand* (Sit2Stand), depending on the patient's movement needs. Additionally, an automatic adjustment of the actuator compliance based on the gait phases and the subject's movement is proposed, increasing safety during the swing phase and stability during the stance phase. The final contribution of this thesis is the development of a muscle fatigue model, parameterized from healthy subject data, that provides insight into fatigue during exoskeleton-assisted walking. This model not only enables the assessment of fatigue but also the automatic selection of the exoskeleton's assistance factor to manage fatigue.

To summarize the overall findings of this thesis and to give an outlook for further improvements and research, the research questions introduced in Chapter 1 are recapitulated in the following:

1. *What are the necessary actuator specifications for an exoskeleton to accommodate dynamic adjustments of serial elasticity throughout various*

phases of a gait cycle?
The *lower limb exoskeleton with serial elastic actuators* (L^2Exo-SE) features two VSAs, specifically the *mechanical-rotary variable impedance actuator* (MeRIA), for hip and knee assistance. The hip acutator's stiffness values range from $265\,\mathrm{N\,m\,rad^{-1}}$ to $515\,\mathrm{N\,m\,rad^{-1}}$, while the knee actuator's values vary between $196\,\mathrm{N\,m\,rad^{-1}}$ and $408\,\mathrm{N\,m\,rad^{-1}}$, respectively. By integrating high-resolution encoders at both ends of the elastic component, the elasticities can serve as torque sensors even under changing stiffness values, thereby enabling force feedback control methods on the L^2Exo-SE.
It is crucial to consider the time required for adjusting the stiffness. For instance, the time for the knee actuator to change from its highest to lowest stiffness is approximately 1.75 seconds. Unfortunately, this duration prevents the actuator from reaching its full potential within a single gait cycle. A solution for this limitation is provided by using a faster motor changing the stiffness as it is incorporated into the hip actuator. This hardware change reduces the stiffness adjustment time to 0.8 seconds, outclassing most current actuator models and ensuring comprehensive stiffness modifications within a single gait cycle.
However, the scope of this work primarily focuses on slow gait velocities, which are suitable for rehabilitation applications. When considering other potential applications, there is a necessity for even faster changing velocities, which would likely require exploring alternative mechanical mechanisms or exploiting the capabilities of pneumatic artificial muscles.

2. *How viable is the real-time estimation of the torque produced by the user in exoskeletons equipped with variable serial elasticities?*
The developed subject torque estimation for the swing phase based on the UKF is fast, reliable, and functions over the entire stiffness range of the MeRIA. Thus, the approach is transferable to other *serial elastic actuators* (SEAs) and VSAs. Simulations demonstrated that subject torques can be reliably estimated up to rates of change of 13.7 Hz and 4 Hz for the knee and hip, respectively. These values exceed the cut-off frequencies of the two joints and are thus considered sufficiently fast. Experiments showed that the UKF based approach is more robust than the conventional inverse dynamics approach.
The reduced performance of the hip joint compared to the knee joint results primarily from the high backlash from the attachment of the exoskeleton with the torso of the test person. The mechanical interface between robot and human is generally considered to be a major challenge in rehabilitation robotics, which is once again confirmed here. One example to address

this problem with regard to the subject torque estimation would be to consider the backlash in the UKF model.

3. *To what extent can the torque estimation strategy be used to formulate individualized assistance control in exoskeletons?*
   The developed patient torque estimation for the swing phase in combination with the static model for the detection of the subject torque in the stance phase is suitable for the use in an assistance control, which includes the entire gait cycle as well as other movements like standing up and sitting down. The transition between the two phase-dependent torque estimates is realized through a fading algorithm based on the *ground reaction forces* (GRFs). Using the developed assistance control strategy, the average user's joint torque during gait is reduced by 63.6 % - 78.4 % for the hip and 40.8 % - 50.2 % for the knee joint compared to unassisted walking. Due to the individual model parameters dependent on the subject anatomy, a system identification or at least an adjustment of the mass values is necessary.
   For the future, it is therefore proposed to perform an online parameter identification, which allows a faster adaptation of the system to the subject. Additionally, the influence of the human-cooperative control on the human body should be investigated by *electromyography* (EMG) and metabolic cost measurements, and further tests should be performed not only on healthy subjects but also on patients with hemiplegia.

4. *How effective is the modulation of serial stiffness in an exoskeleton for enhancing user safety?*
   The presented stiffness adaptation provides high/low stiffness for the high/low impedance task, i.e. high/low human joint torques during the assistance control, in the swing phase. For the stance phase, a high stiffness is provided. Thus, the stiffness adaptation increases the safety of the physical human-robot interaction during the swing phase while maintaining a high control bandwidth during the stance phase. Experiments have shown that applying the lowest stiffness in the knee can reduce the sudden shocks resulting from a collision with a mechanical barrier by 82.8%. Additionally, a virtual stiffness was introduced at the end of the exoskeleton's operating ranges gently pushing the user back into more physiological ranges, which also slows down the user before crushing into the mechanical limitations and thus lowering the strain on the hardware as well as on the human body.

5. *Can muscle fatigue be diagnosed during the use of exoskeletons?*
   Yes, the developed exoskeleton in combination with the serial elastic ele-

ments allowed an online torque estimation of the subject. The estimation of the torque applied by the subject is essential for the assessment of muscle fatigue. In conventional fatigue estimations, this parameter is not available and has to be determined by muscle activity measurements using *electromyography* (EMG). Exoskeletons for the lower extremities are therefore predestined for fatigue estimation during walking. Using the modified 3CCr model and a subject study with healthy subjects this statement could be confirmed. The model parameters were experimentally verified, demonstrating accurate prediction of maximum voluntary contraction (MVC) decline with an average mean absolute error of 4.9%MVC. Up to now, the models have only been parameterized and tested with healthy subjects. In impaired subjects, higher fatigue rates are to be expected, which is why further studies should be conducted with more participants and, above all, patients. In addition, the protocol used in this work for parameter determination is impractical for everyday use in rehabilitation therapy and should therefore be simplified or extended by an online parameter estimation.

6. *Is it feasible to manage the user's muscle fatigue levels by adjusting the level of exoskeleton support?*
   In this thesis, a human-in-the-loop (HiL) controller is proposed to manage muscle fatigue by automatically adjusting the exoskeleton's assistance based on the current state of fatigue and a given reference ratings of perceived fatigue (RPF). The presented control approach effectively regulates fatigue levels within a 0 to 6%MVC steady-state error range during simulations. Experimental validation confirmed this performance, however, with partly higher steady-state errors mainly due to the restrictions of the exoskeleton's assistance.
   Higher assistance values could for example be reached by seamlessly switching from the presented human-cooperative control to impedance or even position-based control concepts if required. It should be emphasized that the control validation was conducted with one healthy subject only. In the future, studies with more subjects and impaired patients should be considered.

In summary, this dissertation presents new approaches to the design and control of lower limb exoskeletons, opening paths for enhanced, adaptable, and patient-focused rehabilitation technology. Prioritizing the exoskeleton's user as the central part of the control system holds the potential to enhance patient mobility and independence in future rehabilitation devices.

Lastly, the validation of the human joint torque estimation and cooperative control strategy in studies with healthy participants suggest a promising foun-

dation for enhancing other assistive devices, such as exoskeletons for industrial applications or upper limb exoskeletons. Applying the estimation and control methods to these devices could help improve worker endurance in production settings and reduce fatigue. This extended applicability highlights the versatility and potential of these control strategies, advancing exoskeleton technology for both clinical and industrial applications.

A Appendix

Ground Reaction Forces

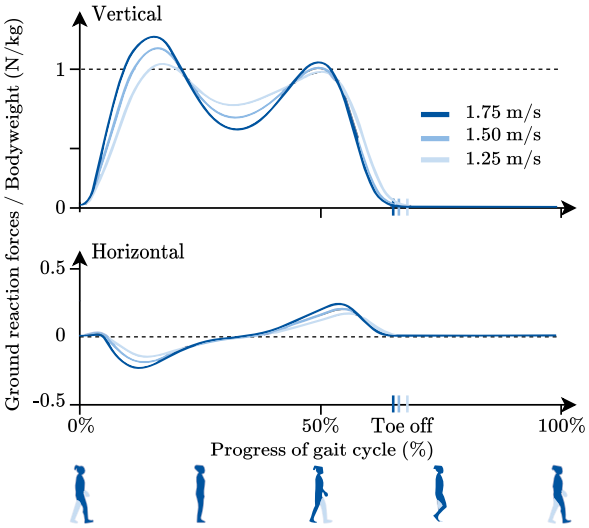

Figure A.1: ground reaction force (GRF) during one gait cycle for three different gait velocities. Data from [AHS+13], Fig. redrawn from [UD21].

Assistance Control and Varying Stiffness

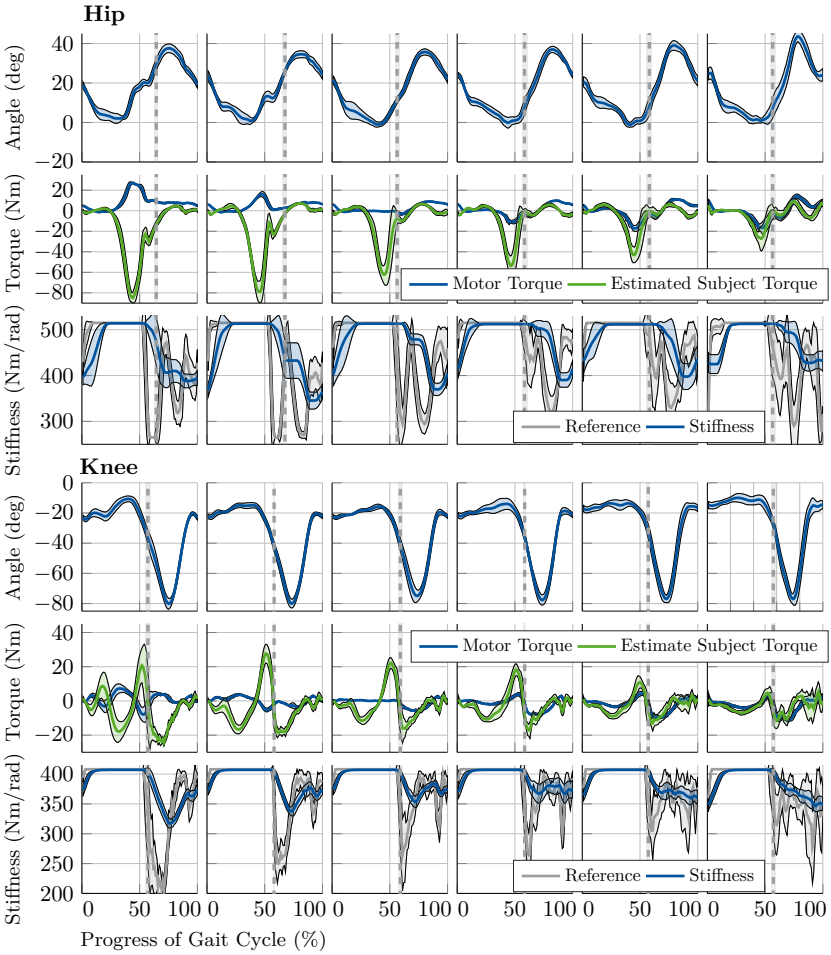

Figure A.2: Gait experiment results. Hip and knee angle, hip and knee joint torques, and hip and knee motor stiffness for six different assistance factors averaged over 10 steps (solid lines) and including standard deviation (SD) (shaded area). The vertical lines present the toe-off event.

Ratings of Perceived Fatigue (RPF)

Table A.1: ratings of perceived fatigue (RPF) scale (adapted from [WSP19]).

Recovery process	RPF	Fatigue process
Completely Rested	0	No fatigue at all
	0.5	Very light fatigue
	1	Light fatigue
	2	Fairly fatigued
	3	Moderately fatigued
	4	Fatigued
50 % Rested	5	Very fatigued
	6	
	7	Nearly exhausted
	8	
	9	
Completely Fatigued	10	Absolutely exhausted

Fatigue Model Parameters

Table A.2: Identified fatigue model parameters for all subjects.

Muscle	Subject	F (/s)	R (/s)	r (-)	MAE (%MVC)
gluteus maximus	1	0.006019	0.000075	23.56	4.33
	2	0.005059	0.000024	15.00	10.46
	3	0.002212	0.000018	27.80	4.69
	4	0.005000	0.000101	15.00	6.46
	5	0.000500	0.000010	15.00	4.86
	6	0.000889	0.000052	13.68	2.84
	Mean	0.003280	0.000047	18.34	5.61
	SD	0.002375	0.000036	5.86	2.64
iliopsoas	1	0.002019	0.000130	26.23	2.09
	2	0.002000	0.000100	15.00	9.05
	3	0.000506	0.000034	9.98	2.94
	4	0.000562	0.000161	15.00	2.63
	5	0.000105	0.000001	14.99	3.99
	6	0.000969	0.000616	8.14	5.27
	Mean	0.001027	0.000174	14.89	4.33
	SD	0.000809	0.000225	6.30	2.57
hamstrings	1	0.002031	0.000086	20.93	2.07
	2	0.002390	0.000022	15.00	3.96
	3	0.001649	0.000120	6.42	2.81
	4	0.000780	0.000137	15.00	2.99
	5	0.000491	0.000157	15.00	5.53
	6	0.002170	0.000061	23.73	5.49
	Mean	0.001585	0.000097	16.01	3.81
	SD	0.000780	0.000051	5.98	1.45
quadriceps femoris	1	0.005837	0.000514	4.73	4.94
	2	0.002500	0.000100	15.00	9.53
	3	0.003337	0.000296	1.00	5.09
	4	0.003000	0.000118	15.00	6.37
	5	0.001000	0.000115	1.00	4.14
	6	0.000075	0.005949	6.44	5.94
	Mean	0.002620	0.001180	7.20	6.00
	SD	0.002010	0.00234	6.41	1.90

Control Validation of Hip

Simulation results (Fig. A.3) and experimental results (Fig. A.4) of the fatigue control validation. The figures supplement the results shown in Sec. 5.4.2.

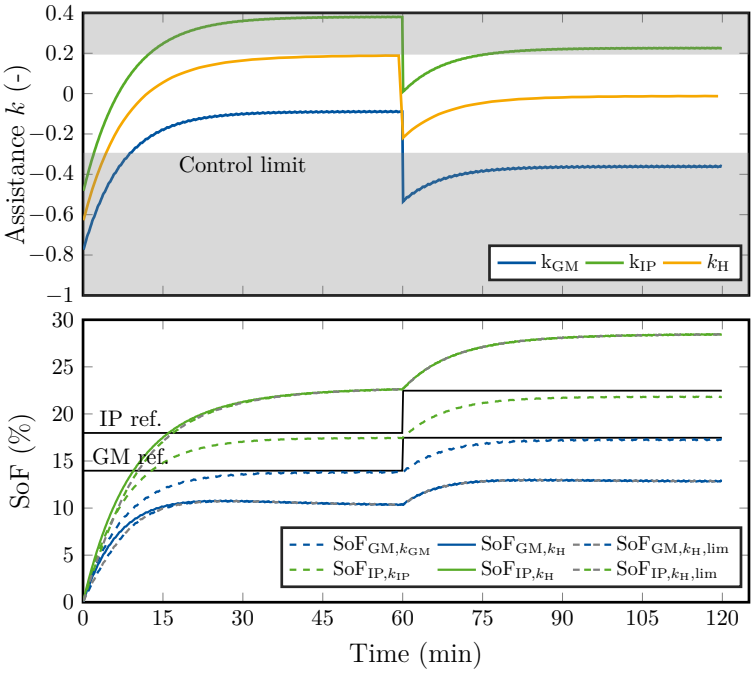

Figure A.3: Simulation results. Top: Ideally calculated assistance factor k for gluteus maximus (GM) (blue, dashed) and iliopsoas (IP) (green, dashed) and actual knee assistance factor (orange, solid) calculated as mean value from ideal assistance factors. Gray area represents the experimental actuation limit. Bottom: state of fatigue (SoF) reference based on a RPF reference of 2 and 2.5 for GM and IP (black). Additionally, simulated SoF of GM (blue) and IP (green) using ideal assistance (dashed), actual assistance (solid), and actual assistance considering exoskeleton's actuation limits (gray, dashed). (© 2024 IEEE)

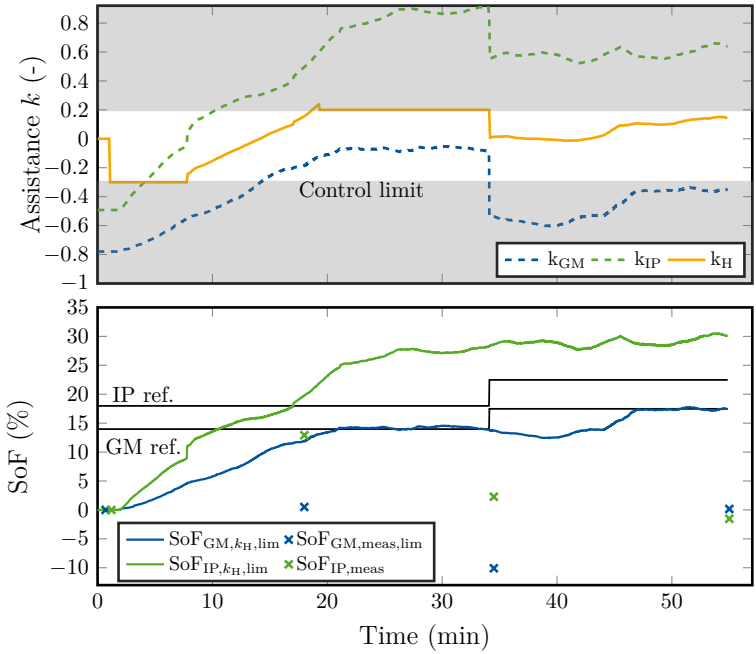

Figure A.4: Experimental results. Top: Ideally calculated assistance factor k for GM (blue, dashed) and IP (green, dashed) and actual knee assistance factor (orange, solid) calculated as the mean value from ideal assistance factors and considering actuation limits. Bottom: Calculated SoF reference based on a RPF reference of 2 and 2.5 for GM and IP (black). Additionally, model-based determined SoF of GM (blue) and IP (green) during the experiment and SoF for GM (blue marks) and IP (green marks) determined via maximum voluntary contraction (MVC) measurements.

B Publications and Achievements

Peer-reviewed Journal Articles Related to the Thesis

1. B. Penzlin, A. Leipnitz, **L. Bergmann**, Y. Li, L. Ji, S. Leonhardt, and C. Ngo: "Conceptual design, modeling and control of a rigid parallel serial-elastic actuator". *at-Automatisierungstechnik*, 68(6):410-422, 2020.

2. L. Liu, Z. Hong, B. Penzlin, B.J.E. Misgeld, C. Ngo, **L. Bergmann**, and S. Leonhardt: "Low impedance-guaranteed gain-scheduled GESO for torque-controlled VSA with application of exoskeleton-assisted sit-to-stand". *IEEE/ASME Transactions on Mechatronics*, 26(4):2080-2091, 2020.

3. **L. Bergmann**, S. Leonhardt, D. Greven, and B.J.E. Misgeld: "Optimal assistive control of a pedal-electric drive unit". *Control Engineering Practice*, 110:104765, 2021.

4. B. Penzlin, **L. Bergmann**, Y. Li, L. Ji, S. Leonhardt, and C. Ngo: "Design and first operation of an active lower limb exoskeleton with parallel elastic actuation". *Actuators*, 10(4):75, 2021.

5. **L. Bergmann**, O. Lück, D. Voss, P. Buschermöhle, L. Liu, S. Leonhardt, and C. Ngo: "Lower limb exoskeleton with compliant actuators: design, modeling, and human torque estimation". *IEEE/ASME Transactions on Mechatronics*, 28(2):758-769., 2022.

6. **L. Bergmann**, L. Hansmann, S. Leonhardt, and C. Ngo: "Hardware development and control of a motorized rollator as an extension for exoskeletons". *at-Automatisierungstechnik*, 70(11):1017-1027, 2022.

7. L. Liu, S. Leonhardt, **L. Bergmann**, B.J.E. Misgeld: "Composite performance of variable stiffness actuator for exoskeleton administrated via impedance control and disturbance observer". *Mechanism and Machine Theory*, 179:105096, 2023.

8. **L. Bergmann**, D. Voss, S. Leonhardt, and C. Ngo: "Lower-Limb Exoskeleton with Compliant Actuators: Human Cooperative Control". *IEEE Transactions on Medical Robotics and Bionics*, 5(3):717-729, 2023.

9. C. Lyu, P.T. Morim, B. Penzlin, F. Röhren, **L. Bergmann**, P. von Platen, C. Bollheimer, S. Leonhardt, and C. Ngo: "Closed-Loop FES Control of a Hybrid Exoskeleton during Sit-to-Stand Exercises: Concept and First Evaluation". *Actuators*, 12(8):316, 2023.

10. G. Koginov, **L. Bergmann**[1], M. Xiloyannis, N. Rohner, C. Ngo, J.E. Duarte, S. Leonhardt, R. Riener: "Human-in-the-loop personalization of a bi-articular wearable robot's assistance for downhill walking". *IEEE Transactions on Medical Robotics and Bionics*, 6(1):328-339, 2023.

11. **L. Bergmann**, L. Hansmann, P. von Platen, S. Leonhardt, and C. Ngo: "Fatigue assessment and control with lower-limb exoskeletons". *Transactions on Human-Machine Systems*, Early access under DOI: 10.1109/THMS.2024.3503473.

Peer-reviewed Journal Articles Not Related to the Thesis

1. S. Lehmann, S. Leonhardt, C. Ngo, **L. Bergmann**, I. Ayed, S. Schrading, and K. Tenbrock: "Global and regional lung function in cystic fibrosis measured by electrical impedance tomography". *Pediatric pulmonology*, 51(11):1191-1199, 2016.

2. S. Lehmann, S. Leonhardt, C. Ngo, **L. Bergmann**, S. Schrading, K. Heimann, N. Wagner, and K. Tenbrock: "Electrical impedance tomography as possible guidance for individual positioning of patients with multiple lung injury". *Pediatric pulmonology*, 12(1):68-75, 2018.

3. D. Rüschen, F. Prochazka, R. Amacher, **L. Bergmann**, S. Leonhardt, and M. Walter: "Minimizing left ventricular stroke work with iterative learning flow profile control of rotary blood pumps". *Biomedical Signal Processing and Control*, 31:444-451, 2017.

4. **L. Bergmann**, D. Rüschen, R. Amacher, O. Nelles, S. Leonhardt, and M. Walter: "Arbeitspunktabhängige Durchflussregelung einer rotatorischen Blutpumpe: Gain Scheduling Flow Control of a Rotary Blood Pump". *Forschung im Ingenieurwesen*, 82(1):21-31, 2018.

Conference Proceedings

1. **L. Bergmann**, D. Rüschen, O. Nelles, S. Leonhardt, and M. Walter: "Gain Scheduling Flow Control of a Rotary Blood Pump". *VDI Mechatroniktagung*. Dresden, Germany, Mar 09 – 10, 2017.

[1] Shared first authorship

2. **L. Bergmann**, L. Liu, C. Ngo, B.J.E. Misgeld, and S. Leonhardt: "Zero-torque control of an exoskeleton joint actuator using a disturbance observer". *German Russian Conference*. Saint Petersburg, Russia, Jul 03 – 07, 2019. Published in *AIP Conference Proceedings*, 2140(1):20004, 2019.

3. **L. Bergmann**, L. Liu, B. Penzlin, S. Leonhardt, and C. Ngo: "Preliminary test of a zero-torque controlled exoskeleton on a treadmill". *AUTOMED - Automatisierung in der Medizintechnik*. Lübeck, Germany, Mar 02 – 03, 2020. Published in *Proceedings on Automation in Medical Engineering*, 1(1):021, 2020.

4. **L. Bergmann**, L. Liu, N. Pham, B. Misgeld, S. Leonhardt, and C. Ngo: "Implementation of LPV $\mathcal{H}_\infty$ loop-shaping control for a variable stiffness actuator". *IFAC World Congress*. Berlin, Virtual Event, Germany, Jul 11 – 17, 2020. Published in *IFAC-PapersOnLine*, 53(2):10129-10134, 2020.

5. B.J.E. Misgeld, **L. Bergmann**, B. Szilasi, S. Leonhardt, and D. Greven: "Virtual torque sensor for electrical bicycles". *IFAC World Congress*. Berlin, Virtual Event, Germany, Jul 11 – 17, 2020. Published in *IFAC-PapersOnLine*, 53(2):8903-8908, 2020.

6. **L. Bergmann**, C. Moazzami, S. Leonhardt, and C. Ngo: "Workflow for 3D modeling of compliant actuators for active exoskeletons". *AUTOMED - Automatisierung in der Medizintechnik*. Basel (virtual), Switzerland, Jun 08 – 09, 2021.

7. **L. Bergmann**, G. Koginov, S. Leonhardt, R. Riener, M. Xiloyannis: "Human-in-the-Loop optimization of hip and knee assistance for downhill walking with the Myosuit". *International Consortium on Rehabilitation Robotics (ICORR)*. Virtual Event, Sep 23 – 25, 2021.

8. **L. Bergmann**, M. Özcan, P. Zunzer: "Hardware Design, Modeling and Wheelie Control of a Motorized Walker". *International Student Conference on Electrical Engineering (POSTER)*. Prague, Czech Republic, May 12 – 13, 2022. Published in *Proceedings of the international student scientific conference POSTER*, 20:134-137, 2022.

9. **L. Bergmann**, V.D. Phan, S. Leonhardt, and C. Ngo: "Gait stability assessment within a patient-cooperative lower limb exoskeleton". *AUTOMED - Automatisierung in der Medizintechnik*. Gießen, Germany, Mar 30 – 31, 2023. Published in *Proceedings on Automation in Medical Engineering*, 2(1):715, 2023.

Patents

1. M.B.J. Misgeld, D. Greven and **L. Bergmann**: *Electric Bicycle*. European Patent, EP3782895B1, Jun 6, 2022.

Awards

- 2016 *ITK Engineering Student Award* 2016, Rülzheim, Germany
- 2019 *Springorum Denkmünze* for the completion of the master's degree with honors, Aachen, Germany
- 2022 3rd place at the International Student Conference on Electrical Engineering POSTER 2022 in the category Informatics and Cybernetics, Prague, Czech Republic

Supervised Student Theses

1. J. Gebler: *Model Predictive Torque Control of a Variable Stiffness Actuator for Lower-Limb Exoskeletons.* Bachelor's thesis, 2019.

2. C. Holländer: *Pattern Recognition of EMG-Signals for Classification of Gait Phases.* Bachelor's thesis, 2020.

3. V. Phan: *Non-linear State Estimation of a Variable Stiffness Actuator.* Bachelor's thesis, 2020.

4. O. Lück: *Modeling and Control of an Exoskeleton for Cooperative Gait Support.* Master's thesis, 2020.

5. H. Petzoldt: *Conception and Implementation of an Attractor-Repulsor Assistant in the Domain of Cooperative Vehicle Guidance for Partially and Highly Automated Vehicles.* Bachelor's thesis at IAW RWTH Aachen University, 2020.

6. D. Voss: *Gait Phase Based Control of a Unilateral Lower Limb Exoskeleton.* Master's thesis, 2021.

7. C. Moazzami: *Multi-domain Modeling of a Variable Stiffness Actuator for Active Exoskeletons.* Bachelor's thesis, 2021.

8. P. Buschermöhle: *Model-predictive Assistive Control of a Unilateral Exoskeleton for Lower Limbs.* Master's thesis, 2021.

9. M. Gutheil: *Assistive Control of a Unilateral Exoskeleton Based on Mirroring of Gait Trajectories.* Master's thesis, 2021.

10. P. Händel: *Torque and Impedance Control of Stiff Actuation Systems for Rehabilitation Robotics.* Master's thesis, 2022.

11. V. Phan: *Modeling and Development of Gait Stabilization within a Patient-cooperative Exoskeleton Control Framework.* Master's thesis, 2022.

12. Y. Chen: *Development of an adaptive trajectory command and contact force control for a robotically guided ultrasound system.* Master's thesis at mediTEC RWTH Aachen University, 2022.

13. L. Hansmann: *Development of a Fatigue Model for Human-in-the-Loop Control with Exoskeletons.* Master's thesis, 2022.

Curriculum Vitae

31.10.2024	Doctoral Examination for Dr.-Ing.
2024	R&D Engineer ANYbotics AG, Switzerland
2019–2024	Research Associate and Doctoral Candidate Chair for Medical Information Technology (MedIT) RWTH Aachen University, Germany
2021	Research Stay Sensory-Motor Systems Lab ETH Zurich, Switzerland
2015–2019	Master's Degree in Electrical Engineering majoring in Systems Engineering and Automation RWTH Aachen University, Germany
2016-2017	Semester Abroad KTH Stockholm, Sweden
2015–2019	Bachelor's Degree in Electrical Engineering majoring in Information and Communications Technology RWTH Aachen University, Germany
2004-2012	General Certificate of Education (Abitur) Ursulaschule Osnabrück, Germany
26.04.1994	born in Mettingen, Germany

C Disclosure Statement

In the process of composing and refining this thesis, I have employed the assistance of generative artificial intelligence models, specifically *ChatGPT-3.5*, *ChatGPT-4* developed by OpenAI and *DeepL Write* developed by DeepL SE, for the purpose of modifying certain sentences and paragraphs to enhance clarity, coherence, and linguistic structure. However, it is important to clarify that the content, research, analysis, and conclusions of this thesis are solely the result of my original work, thoughts, and contributions.

Bibliography

[AHS+13] E. M. Arnold, S. R. Hamner, A. Seth, M. Millard, and S. L. Delp: "How muscle fiber lengths and velocities affect muscle force generation as humans walk and run at different speeds". *Journal of Experimental Biology*, 216(11):2150–2160, 2013.

[Ali17] S. K. Ali: *Modeling and Control of De-weighting Upper-Limb Exoskeleton*. dissertation, University of Sheffield, 2017.

[AMN07] D. E. Anderson, M. L. Madigan, and M. A. Nussbaum: "Maximum voluntary joint torque as a function of joint angle and angular velocity: model development and application to the lower limb". *Journal of biomechanics*, 40(14):3105–3113, 2007.

[AOCPG07] G. Aguirre-Ollinger, J. Colgate, M. A. Peshkin, and A. Goswami: "Active Impedance Control of a Lower Limb Assistive Exoskeleton". *2007 IEEE 10th International Conference on Rehabilitation Robotics*, 188–195, 2007.

[Bab19] S. Babasaheb Karvekar: *Smartphone-based Human Fatigue Detection in an Industrial Environment Using Gait Analysis*. Rochester Institute of Technology, 2019.

[BDR+13] M. Bortole, A. Del Ama, E. Rocon, J. C. Moreno, F. Brunetti, and J. L. Pons: "A robotic exoskeleton for overground gait rehabilitation". *Proceedings - IEEE International Conference on Robotics and Automation*, 3356–3361, 2013.

[BHLN22] L. Bergmann, L. Hansmann, S. Leonhardt, and C. Ngo: "Hardware Development and Control of a Motorized Rollator as an Extension for Exoskeletons". *At-Automatisierungstechnik*, 70(10), 2022.

[BHvP+24] L. Bergmann, L. Hansmann, P. von Platen, S. Leonhardt, and C. Ngo: "Fatigue assessment and control with lower-limb exoskeletons". *IEEE Transactions on Human Machine Systems*, 2024. Early access DOI: 10.1109/THMS.2024.3503473.

[Bin88] G. P. Bingham: "Task-specific devices and the perceptual bottleneck". *Human Movement Science*, 7(2-4):225–264, 1988.

[BLGM21] L. Bergmann, S. Leonhardt, D. Greven, and B. J. Misgeld: "Optimal assistive control of a pedal-electric drive unit". *Control Engineering Practice*, 110:104765, 2021.

[BLV+22] L. Bergmann, O. Lück, D. Voss, P. Buschermöhle, L. Liu, S. Leonhardt, and C. Ngo: "Lower-Limb Exoskeleton with Compliant Actuators: Design, Modeling and Human Torque Estimation". *IEEE/ASME Transactions on Mechatronics*, 1–12, 2022.

[BMA15] A. Bonnefoy-Mazure and S. Armand: "Normal gait". *Orthopedic Management of Children with Cerebral Palsy: A Comprehensive Approach*, 199–214. Nova Science Publishers, Inc., 2015.

[BMD+20] X. Bao, V. Molazadeh, A. Dodson, B. E. Dicianno, and N. Sharma: "Using person-specific muscle fatigue characteristics to optimally allocate control in a hybrid exoskeleton—preliminary results". *IEEE transactions on medical robotics and bionics*, 2(2):226–235, 2020.

[BPH+13] D. J. Braun, F. Petit, F. Huber, S. Haddadin, P. Van Der Smagt, A. Albu-Schaffer, and S. Vijayakumar: "Robots driven by compliant actuators: Optimal control under actuation constraints". *IEEE Transactions on Robotics*, 29(5):1085–1101, 2013.

[BSA+17] Baltej Singh Rupal, Sajid Rafique, Ashish Singla, Ekta Singla, Magnus Isaksson, and Gurvinder Singh Virk: "Lower-limb exoskeletons: Research trends and regulatory guidelines in medical and non-medical applications". *International Journal of Advanced Robotic Systems*, 14(6):1729881417743554, 2017.

[BVLN23] L. Bergmann, D. Voss, S. Leonhardt, and C. Ngo: "Lower-Limb Exoskeleton with Compliant Actuators: Human Cooperative Control". *IEEE Transactions on Medical Robotics and Bionics*, 70(11):1017–1027, 2023.

[BVZ+15] M. Bortole, A. Venkatakrishnan, F. Zhu, J. C. Moreno, G. E. Francisco, J. L. Pons, and J. L. Contreras-Vidal: "The H2 robotic exoskeleton for gait rehabilitation after stroke: Early findings from a clinical study Wearable robotics in clinical testing". *Journal of NeuroEngineering and Rehabilitation*, 12(1):1–14, 2015.

[CF16] A. Calanca and P. Fiorini: "On the role of compliance in force control". *Advances in Intelligent Systems and Computing*, vol. 302, 1243–1255, 2016.

[CFLN+20] N. Cheema, L. A. Frey-Law, K. Naderi, J. Lehtinen, P. Slusallek, and P. Hämäläinen: "Predicting mid-air interaction movements

and fatigue using deep reinforcement learning". *Proceedings of the 2020 CHI Conference on Human Factors in Computing Systems*, 1–13, 2020.

[CMTO09] M. Cifrek, V. Medved, S. Tonković, and S. Ostojić: "Surface EMG based muscle fatigue evaluation in biomechanics". *Clinical biomechanics*, 24(4):327–340, 2009.

[CSMAG15] M. Cestari, D. Sanz-Merodio, J. C. Arevalo, and E. Garcia: "An adjustable compliant joint for lower-limb exoskeletons". *IEEE/ASME Transactions on Mechatronics*, 20(2):889–898, 2015.

[CZZ+20] C. Chen, S. Zhang, X. Zhu, J. Shen, and Z. Xu: "Disturbance Observer-Based Patient-Cooperative Control of a Lower Extremity Rehabilitation Exoskeleton". *International Journal of Precision Engineering and Manufacturing*, 21(5):957–968, 2020.

[DBJ+13] P. DeSaix, G. J. Betts, E. Johnson, J. E. Johnson, K. Oksana, D. H. Kruse, B. Poe, J. A. Wise, and K. A. Young: "Anatomy & Physiology (OpenStax)", 2013.

[DIDJ17] S. Dobrijevic, V. Ilic, S. Djuric, and S. Jaric: "Force-velocity relationship of leg muscles assessed with motorized treadmill tests: Two-velocity method". *Gait & posture*, 56:60–64, 2017.

[DMS17] C. Dohle, F. Müller, and K. Stephan: "Technical Developments for Rehabilitation of Mobility". *Neurology International Open*, 1(3):E211–E216, 2017.

[DNG+20] J. R. Dorneles, F. R. Neto, C. W. Gonçalves, R. R. G. Costa, and R. L. Carregaro: "Does prolonged walking cause greater muscle fatigability in individuals with incomplete spinal cord injury compared with matched-controls?" *Gait & Posture*, 78:65–71, 2020.

[DSBB+09] B. Danneskiold-Samsøe, E. M. Bartels, P. M. Bülow, H. Lund, A. Stockmarr, C. C. Holm, I. Wätjen, M. Appleyard, and H. Bliddal: "Isokinetic and isometric muscle strength in a healthy population with special reference to age and gender". *Acta physiologica*, 197:1–68, 2009.

[DSDB08] A. De Santis, B. Siciliano, A. De Luca, and A. Bicchi: "An atlas of physical human-robot interaction". *Mechanism and Machine Theory*, 43(3):253–270, 2008.

[DSS19] H. Dittrich, M. Schimmack, and C.-H. Siemsen: *Orthopädische Biomechanik: Einführung in die Endoprothetik der Gelenke der unteren Extremitäten*. Springer-Verlag, 2019.

[DZB+05] P. W. Duncan, R. Zorowitz, B. Bates, J. Y. Choi, J. J. Glasberg, G. D. Graham, R. C. Katz, K. Lamberty, and D. Reker: "Management of Adult Stroke Rehabilitation Care: a clinical practice guideline." *Stroke; a journal of cerebral circulation*, 36(9):100–143, 2005.

[ED08] R. M. Enoka and J. Duchateau: "Muscle fatigue: what, why and how it influences muscle function". *The Journal of physiology*, 586(1):11–23, 2008.

[ED16] R. M. Enoka and J. Duchateau: "Translating fatigue to human performance". *Medicine and science in sports and exercise*, 48(11):2228, 2016.

[ETPS12] A. Esquenazi, M. Talaty, A. Packel, and M. Saulino: "The ReWalk Powered Exoskeleton to Restore Ambulatory Function to Individuals with Thoracic-Level Motor-Complete Spinal Cord Injury". *American Journal of Physical Medicine & Rehabilitation*, 91(11):911–921, 2012.

[FLLH12] L. A. Frey-Law, J. M. Looft, and J. Heitsman: "A three-compartment muscle fatigue model accurately predicts joint-specific maximum endurance times for sustained isometric tasks". *Journal of biomechanics*, 45(10):1803–1808, 2012.

[FLSU21] L. A. Frey-Law, M. Schaffer, and F. K. Urban: "Muscle fatigue modelling: Solving for fatigue and recovery parameter values using fewer maximum effort assessments". *International Journal of Industrial Ergonomics*, 82:103104, 2021.

[FWL+13] S. A. Fayazi, N. Wan, S. Lucich, A. Vahidi, and G. Mocko: "Optimal pacing in a cycling time-trial considering cyclist's fatigue dynamics". *Proceedings of the American Control Conference*, 2013.

[GLG93] L. N. Gitlin, R. Levine, and C. Geiger: "Adaptive device use by older adults with mixed disabilities". *Archives of Physical Medicine and Rehabilitation*, 74(2):149–152, 1993.

[GLK00] B. Gerdle, B. Larsson, and S. Karlsson: "Criterion validation of surface EMG variables as fatigue indicators using peak torque: a study of repetitive maximum isokinetic knee extensions". *Journal of Electromyography and Kinesiology*, 10(4):225–232, 2000.

[GMLO93] Y. Giat, J. Mizrahi, M. Levy, and Others: "A musculotendon model of the fatigue profiles of paralyzed quadriceps muscle under FES". *IEEE transactions on biomedical engineering*, 40(7):664–674, 1993.

[GRGG+17] V. Grosu, C. Rodriguez-Guerrero, S. Grosu, B. Vanderborght, and D. Lefeber: "Design of Smart Modular Variable Stiffness Actuators for Robotic-Assistive Devices". *IEEE/ASME Transactions on Mechatronics*, 22(4):1777–1785, 2017.

[GSK06] J. Ghan, R. Steger, and H. Kazerooni: "Control and system identification for the Berkeley lower extremity exoskeleton (BLEEX)". *Advanced Robotics*, 20(9):989–1014, 2006.

[GZG18] Z. Y. Gu, J. Zhang, and L. Gui: *Force Control Theory and Method of Human Load Carrying Exoskeleton Suit*. Springer Verlag, Wiesbaden, 1st ed., 2018.

[Hay04] S. Haykin: *Kalman filtering and neural networks*, vol. 47. John Wiley & Sons, 2004.

[HHAS12] S. Haddadin, F. Huber, and A. Albu-Schäffer: "Optimal control for exploiting the natural dynamics of Variable Stiffness robots". *Proceedings - IEEE International Conference on Robotics and Automation*, 3347–3354, 2012.

[HJ15] B. Hwang and D. Jeon: "A method to accurately estimate the muscular torques of human wearing exoskeletons by Torque sensors". *Sensors (Switzerland)*, 15(4):8337–8357, 2015.

[HK07] H. He and K. Kiguchi: "A study on EMG-based control of exoskeleton robots for human lower-limb motion assist". *2007 6th International special topic conference on information technology applications in biomedicine*, 292–295. IEEE, 2007.

[HKS05] T. Hayashi, H. Kawamoto, and Y. Sankai: "Control Method of Robot Suit HAL working as Operator's Muscle using Biological and Dynamical Information". *2005 IEEE/RSJ International Conference on Intelligent Robots and Systems*, 2005.

[HMAK16] W. Huo, S. Mohammed, Y. Amirat, and K. Kong: "Active Impedance Control of a lower limb exoskeleton to assist sit-to-stand movement". *Proceedings - IEEE International Conference on Robotics and Automation*, 2016-June:3530–3536, 2016.

[HMT+21] M. Hamaya, T. Matsubara, T. Teramae, T. Noda, and J. Morimoto: "Design of physical user–robot interactions for model identification of soft actuators on exoskeleton robots". *International Journal of Robotics Research*, 40(1):397–410, 2021.

[HNP+09] J. Hidler, D. Nichols, M. Pelliccio, K. Brady, D. D. Campbell, J. H. Kahn, and T. G. Hornby: "Multicenter Randomized Clinical Trial Evaluating the Effectiveness of the Lokomat in Subacute Stroke". *Neurorehabilitation and neural repair*, 23(1):5–13, 2009.

[Hog84] N. Hogan: "IMPEDANCE CONTROL: AN APPROACH TO MANIPULATION". *1984 American Control Conference*, 304–313, 1984.

[HSJ+20] K. S. Hyun, L. B. Suk, L. H. Jin, K. E. Joo, L. J. Ah, Y. S. Phil, K. T. Young, P. H. Ram, K. H. Ki, K. H. Young, J. J. Hwan, and O. S. Wook: "Energy Efficiency and Patient Satisfaction of Gait With Knee-Ankle-Foot Orthosis and Robot (ReWalk)-Assisted Gait in Patients With Spinal Cord Injury". *Annals of rehabilitation medicine*, 44(2):191–141, 2020.

[HSMW13] S. Hesse, N. Schattat, J. Mehrholz, and C. Werner: "Evidence of end-effector based gait machines in gait rehabilitation after CNS lesion". *NeuroRehabilitation*, 33(1):77–84, 2013.

[HUO00] S. Hesse, D. Uhlenbrock, and Others: "A mechanized gait trainer for restoration of gait". *Journal of rehabilitation research and development*, 37(6):701–708, 2000.

[IM11] R. Isermann and M. Münchhof: *Identification of Dynamic Systems*. Heidelberg: Springer, vol. 85 ed., 2011.

[IS15] J. C. P. Ibarra and A. A. G. Siqueira: "Impedance Control of Rehabilitation Robots for Lower Limbs. Review". *SBR-LARS Robotics Symposium and Robocontrol*, 235–240, 2015.

[IW14] S. Irgenfried and H. Wörn: "Motion control and fall prevention for an activewalker mobility aid". *New Advances in Mechanisms,*

Transmissions and Applications: Proceedings of the Second Conference MeTrApp 2013, vol. 17, 157–164. Springer, 2014.

[Jaf14] A. Jafari: "Coupling between the Output Force and Stiffness in Different Variable Stiffness Actuators". *Actuators*, 3(3):270, 2014.

[JBG+14] K. Junius, B. Brackx, V. Grosu, H. Cuypers, J. Geeroms, M. Moltedo, B. Vanderborght, and D. Lefeber: "Mechatronic Design of a Sit-to-Stance Exoskeleton". *Proceedings of the 5th IEEE RAS/EMBS International Conference on Biomedical Robotics and Biomechatronics. São Paulo*, 945–950. IEEE, 2014.

[JCK+03] S. Jezernik, G. Colombo, T. Keller, H. Frueh, and M. Morari: "Robotic Orthosis Lokomat: A Rehabilitation and Research Tool". *Neuromodulation: Technology at the neural interface*, 6(2):108–115, 2003.

[JFWRC+18] R. Jimenez-Fabian, M. Weckx, D. Rodriguez-Cianca, D. Lefeber, and B. Vanderborght: "Online Reconfiguration of a Variable-Stiffness Actuator". *IEEE/ASME Transactions on Mechatronics*, 23(4):1866–1876, 2018.

[JNR+19] C. O. Johnson, M. Nguyen, G. A. Roth, E. Nichols, T. Alam, and Others: "Global, regional, and national burden of stroke, 1990–2016: a systematic analysis for the Global Burden of Disease Study 2016". *The Lancet Neurology*, 18(5):439–458, 2019.

[JSAR17] S. Jang, W. Stuerzlinger, S. Ambike, and K. Ramani: "Modeling cumulative arm fatigue in mid-air interaction based on perceived exertion and kinetics of arm motion". *Proceedings of the 2017 CHI Conference on Human Factors in Computing Systems*, 3328–3339, 2017.

[JSB90] M. Jetté, K. Sidney, and G. Blümchen: "Metabolic equivalents ({METS}) in exercise testing, exercise prescription, and evaluation of functional capacity". *Clin Cardiol*, 13(8):555–565, 1990.

[JU97] S. J. Julier and J. K. Uhlmann: "New extension of the Kalman filter to nonlinear systems". *Signal Processing, Sensor Fusion, and Target Recognition VI*, vol. 3068, 182–193, 1997.

[JU04] S. J. Julier and J. K. Uhlmann: "Unscented filtering and nonlinear estimation". *Proceedings of the IEEE*, 401–422, 2004.

[KADS16] N. Kirsch, N. Alibeji, B. E. Dicianno, and N. Sharma: "Switching control of functional electrical stimulation and motor assist for muscle fatigue compensation". *2016 American Control Conference (ACC)*, 4865–4870. IEEE, 2016.

[Kal60] R. E. Kalman: "A new approach to linear filtering and prediction problems". *Journal of basic Engineering*, 82(1):35–45, 1960.

[KANP02] S. Kumar, T. Amell, Y. Narayan, and N. Prasad: "Indices of muscle fatigue". *Proceedings of the Human Factors and Ergonomics Society Annual Meeting*, 46(13):1095–1099, 2002.

[KBA+17] N. A. Kirsch, X. Bao, N. A. Alibeji, B. E. Dicianno, and N. Sharma: "Model-based dynamic control allocation in a hybrid neuroprosthesis". *IEEE Transactions on Neural Systems and Rehabilitation Engineering*, 26(1):224–232, 2017.

[KFI08] R. Kandepu, B. Foss, and L. Imsland: "Applying the unscented Kalman filter for nonlinear state estimation". *Journal of Process Control*, 18(7-8):753–768, 2008.

[KH12] K. Kiguchi and Y. Hayashi: "An EMG-based control for an upper-limb power-assist exoskeleton robot". *IEEE Transactions on Systems, Man, and Cybernetics, Part B (Cybernetics)*, 42(4):1064–1071, 2012.

[KID+11] S. Knorr, T. D. Ivanova, T. J. Doherty, J. A. Campbell, and S. J. Garland: "The origins of neuromuscular fatigue post-stroke". *Experimental Brain Research*, 214(2):303, 2011.

[KML15] N.-S. Kwak, K.-R. Müller, and S.-W. Lee: "A lower limb exoskeleton control system based on steady state visual evoked potentials". *Journal of Neural Engineering*, 12(5):56009, 2015.

[KRG12] S. Knorr, C. L. Rice, and S. J. Garland: "Perspective on neuromuscular factors in poststroke fatigue". *Disability and Rehabilitation*, 34(26):2291–2299, 2012.

[Kru03] L. B. Krupp: *Fatigue*. Butterworth-Heinemann, 2003.

[LB99] G. Li and P. Buckle: "Current techniques for assessing physical exposure to work-related musculoskeletal risks, with emphasis on posture-based methods". *Ergonomics*, 42(5):674–695, 1999.

[LBY02] J. Z. Liu, R. W. Brown, and G. H. Yue: "A dynamical model of muscle activation, fatigue, and recovery". *Biophysical journal*, 82(5):2344–2359, 2002.

[LCD+01] E. S. Lawrence, C. Coshall, R. Dundas, J. Stewart, A. G. Rudd, R. Howard, and C. D. A. Wolfe: "Estimates of the prevalence of acute stroke impairments and disability in a multiethnic population". *Stroke*, 32(6):1279–1284, 2001.

[LDW+18] Z. Li, W. Dong, L. Wang, C. Chen, J. Wang, and Z. Du: "Lower Limb Exoskeleton Hybrid Phase Control Based on Fuzzy Gain Sliding Mode Controller". *2018 2nd International Conference on Robotics and Automation Sciences, ICRAS 2018*, 184–190, 2018.

[LDZ+18] M. Li, J. Deng, F. Zha, S. Qiu, X. Wang, and F. Chen: "Towards online estimation of human joint muscular torque with a lower limb exoskeleton robot". *Applied Sciences (Switzerland)*, 8(9):1610, 2018.

[LFR20] H. Lee, P. W. Ferguson, and J. Rosen: "Chapter 11 - Lower Limb Exoskeleton Systems—Overview". J. Rosen and P. W. Ferguson (eds.), *Wearable Robotics: Systems and Applications*, chap. 11, 207–229. Academic Press, 2020.

[LHA+17] Z. Li, B. Huang, A. Ajoudani, C. Yang, C.-Y. Su, and A. Bicchi: "Asymmetric bimanual control of dual-arm exoskeletons for human-cooperative manipulations". *IEEE Transactions on Robotics*, 34(1):264–271, 2017.

[LHFL18] J. M. Looft, N. Herkert, and L. Frey-Law: "Modification of a three-compartment muscle fatigue model to predict peak torque decline during intermittent tasks". *Journal of biomechanics*, 77:16–25, 2018.

[LHP+20] L. Liu, Z. Hong, B. Penzlin, B. Misgeld, C. Ngo, L. Bergmann, and S. Leonhardt: "Low Impedance-Guaranteed Gain-Scheduled GESO for Torque-Controlled VSA, with Application of Exoskeleton-Assisted Sit-to-Stand". *IEEE/ASME Transactions on Mechatronics*, 4435(c):1–1, 2020.

[LKLM15] L. Liu, M. Kramer, S. Leonhardt, and B. J. E. Misgeld: "Design and Modeling of a Mechanical Rotational Impedance Actuator". *VDI Mechatronik 2015*, 331–336, 2015.

[LLM16] L. Liu, S. Leonhardt, and B. J. Misgeld: "Design and control of a mechanical rotary variable impedance actuator". *Mechatronics*, 39:226–236, 2016.

[LLM18] L. Liu, S. Leonhardt, and B. J. Misgeld: "Experimental validation of a torque-controlled variable stiffness actuator tuned by gain scheduling". *IEEE/ASME Transactions on Mechatronics*, 23(5):2109–2120, 2018.

[LLNM20] L. Liu, S. Leonhardt, C. Ngo, and B. J. Misgeld: "Impedance-Controlled Variable Stiffness Actuator for Lower Limb Robot Applications". *IEEE Transactions on Automation Science and Engineering*, 17(2):991–1004, 2020.

[LMP+23] C. Lyu, P. T. Morim, B. Penzlin, F. Röhren, L. Bergmann, P. von Platen, C. Bollheimer, S. Leonhardt, and C. Ngo: "Closed-Loop FES Control of a Hybrid Exoskeleton during Sit-to-Stand Exercises: Concept and First Evaluation". *Actuators*, 12(8):316, 2023.

[LPCY18] X. Li, Y. Pan, G. Chen, and H. Yu: "Continuous Tracking Control for a Compliant Actuator with Two-Stage Stiffness". *IEEE Transactions on Automation Science and Engineering*, 15(1):57–66, 2018.

[LRZ+20] Z. Li, Z. Ren, K. Zhao, C. Deng, and Y. Feng: "Human-Cooperative Control Design of a Walking Exoskeleton for Body Weight Support". *IEEE Transactions on Industrial Informatics*, 16(5):2985–2996, 2020.

[Mar14] D. Marks: "Functional Ambulation Categories (FAC)–Die Gehfähigkeit beurteilen". *ergopraxis*, 7(05):34–35, 2014.

[MBCZ08] L. Ma, F. Bennis, D. Chablat, and W. Zhang: "Framework for dynamic evaluation of muscle fatigue in manual handling work". *2008 IEEE International Conference on Industrial Technology*, 1–6. IEEE, 2008.

[MCB+10] L. Ma, D. Chablat, F. Bennis, W. Zhang, and F. Guillaume: "A new muscle fatigue and recovery model and its ergonomics application in human simulation". *Virtual and Physical Prototyping*, 5(3):123–137, 2010.

[MCBM12] R. Ma, D. Chablat, F. Bennis, and L. Ma: "Human muscle fatigue model in dynamic motions". *Latest Advances in Robot Kinematics*, 349–356. Springer, 2012.

[MCBZ09] L. Ma, D. Chablat, F. Bennis, and W. Zhang: "A new simple dynamic muscle fatigue model and its validation". *International Journal of Industrial Ergonomics*, 39(1):211–220, 2009.

[MHH13] E. N. Marieb, K. Hoehn, and M. Hutchinson: *Human anatomy & physiology*. Pearson Education/Benjamin Cummings, 9th ed., 2013.

[MKQ+07] A. Mayr, M. Kofler, E. Quirbach, H. Matzak, K. Fröhlich, and L. Saltuari: "Prospective, Blinded, Randomized Crossover Study of Gait Rehabilitation in Stroke Patients Using the Lokomat Gait Orthosis". *Neurorehabilitation and neural repair*, 21(4):307–314, 2007.

[Mos67] R. S. Mosher: "Handyman to Hardiman". *SAE Technical Papers*, 76(1):588–597, 1967.

[MP05] J. H. McClellan and T. W. Parks: "A personal history of the Parks-McClellan algorithm". *IEEE Signal Processing Magazine*, 22(2):82–86, 2005.

[MP12] J. Mehrholz and M. Pohl: "Electromechanical-assisted gait training after stroke: a systematic review comparing end-effector and exoskeleton devices". *Journal of rehabilitation medicine*, 44(3):193–199, 2012.

[MZD+23] G. Masengo, X. Zhang, R. Dong, A. B. Alhassan, K. Hamza, and E. Mudaheranwa: "Lower limb exoskeleton robot and its cooperative control: A review, trends, and challenges for future research". *Frontiers in Neurorobotics*, 16(12 January):913748, 2023.

[Nel08] G. Nelles: *Rehabilitation von sensomotorischen Störungen. S2k-Leitlinie*. Deutsche Gesellschaft für Allgemeinmedizin und Familienmedizin e.V., 2008.

[NEL20] O. NELLES: *NONLINEAR SYSTEM IDENTIFICATION: From Classical Approaches to Neural Networks, Fuzzy Systems, and Gaussian Processes*. SPRINGER NATURE, 2020.

[NGY21] Y. Ni, Y. Gao, and J. Yao: "Introduction to musculoskeletal system". *Biomechanical modelling and simulation on musculoskeletal system*, 1–34. Springer, 2021.

[NJR+18] M. B. Naf, K. Junius, M. Rossini, C. Rodriguez-Guerrero, B. Vanderborght, and D. Lefeber: "Misalignment Compensation for Full Human-Exoskeleton Kinematic Compatibility: State of the Art and Evaluation". *Applied Mechanics Reviews*, 70(5):1–19, 2018.

[PBL+21] B. Penzlin, L. Bergmann, Y. Li, L. Ji, S. Leonhardt, and C. Ngo: "Design and first operation of an active lower limb exoskeleton with parallel elastic actuation". *Actuators*, 10(4):75, 2021.

[PDAS15] F. Petit, A. Dietrich, and A. Albu-Schäffer: "Generalizing torque control concepts". *IEEE Robotics and Automation Magazine*, 22(4):37–51, 2015.

[PL08] P. Parijat and T. E. Lockhart: "Effects of quadriceps fatigue on the biomechanics of gait and slip propensity". *Gait & posture*, 28(4):568–573, 2008.

[PLB+21] B. Penzlin, C. Lyu, L. Bergmann, C.-F. Benner, Y. Li, L. Ji, M. Lüken, S. Leonhardt, and C. Ngo: "Interactive gait control of an active lower limb exoskeleton using insole FSR for detection of patient's movement intention". *Biomedical Engineering / Biomedizinische Technik*, 66(s1):161–162, 2021.

[Pon08] J. L. Pons: *Wearable Robots: Biomechatronic Exoskeletons*. John Wiley and Sons, 1st ed., 2008.

[QGCC21] S. Qiu, W. Guo, D. Caldwell, and F. Chen: "Exoskeleton Online Learning and Estimation of Human Walking Intention Based on Dynamical Movement Primitives". *IEEE Transactions on Cognitive and Developmental Systems*, 13(1):67–79, 2021.

[RE99] R. Riener and T. Edrich: "Identification of passive elastic joint moments in the lower extremities". *Journal of Biomechanics*, 32(5):539–544, 1999.

[Reh20] RehaStim: *End-Effector Gait Trainers - Advantages and Versatility in Therapy*. Tech. rep., Reha-Stim Medtec AG, 2020.

[Rie16] R. Riener: *Technology of the robotic gait orthosis Lokomat*, 395—-407. Springer, 2016.

[RN16] E. Rashedi and M. A. Nussbaum: "Cycle time influences the development of muscle fatigue at low to moderate levels of intermittent muscle contraction". *Journal of Electromyography and Kinesiology*, 28:37–45, 2016.

[Roh60] W. Rohmert: "Determination of the recovery pause for static work of man". *Internationale Zeitschrift Fur Angewandte Physiologie, Einschliesslich Arbeitsphysiologie*, 18:123–164, 1960.

[RQ97] R. Riener and J. Quintern: "A physiologically based model of muscle activation verified by electrical stimulation". *Bioelectrochemistry and bioenergetics*, 43(2):257–264, 1997.

[SCB+16] D. Seth, D. Chablat, F. Bennis, S. Sakka, M. Jubeau, and A. Nordez: "New dynamic muscle fatigue model to limit musculoskeletal disorder". S. Richir (ed.), *Proceedings of the 2016 Virtual Reality International Conference*, 1–8. ACM, 2016.

[SDG+17] K. Schmidt, J. E. Duarte, M. Grimmer, A. Sancho-Puchades, H. Wei, C. S. Easthope, and R. Riener: "The myosuit: Bi-articular anti-gravity exosuit that reduces hip extensor activity in sitting transfers". *Frontiers in neurorobotics*, 11:57, 2017.

[SLC19] M. Saadatzi, D. C. Long, and O. Celik: "Comparison of Human-Robot Interaction Torque Estimation Methods in a Wrist Rehabilitation Exoskeleton". *Journal of Intelligent and Robotic Systems: Theory and Applications*, 94(3-4), 2019.

[Smi08] J. D. Smith: "Effects of prosthesis inertia on the mechanics and energetics of amputee locomotion". *The Pennsylvania State University*, 2008.

[SP16] M. W. Sonne and J. R. Potvin: "A modified version of the three-compartment model to predict fatigue during submaximal tasks with complex force-time histories". *Ergonomics*, 59(1):85–98, 2016.

[SVGVT+19] M. C. Sanchez-Villamañan, J. Gonzalez-Vargas, D. Torricelli, J. C. Moreno, and J. L. Pons: "Compliant lower limb exoskeletons: a comprehensive review on mechanical design principles". *Journal of Neuroengineering and Rehabilitation*, 16(1):1–16, 2019.

[SWB+07] H. Schmidt, C. Werner, R. Bernhardt, S. Hesse, and J. Krüger: "Gait rehabilitation machines based on programmable footplates". *Journal of neuroengineering and rehabilitation*, 4(1):1–7, 2007.

[SWH+16] M. A. Samaan, J. T. Weinhandl, S. A. Hans, S. Y. Bawab, and S. I. Ringleb: "Predictive neuromuscular fatigue of the lower extremity utilizing computer modeling". *Journal of Biomechanical Engineering*, 138(1):11008, 2016.

[TA20] C. Thalman and P. Artemiadis: "A review of soft wearable robots that provide active assistance: Trends, common actuation methods, fabrication, and applications". *Wearable Technologies*, 1:3, 2020.

[TBV+22] M. Tiboni, A. Borboni, F. Vérité, C. Bregoli, and C. Amici: "Sensors and actuation technologies in exoskeletons: A review". *Sensors*, 22(3):884, 2022.

[TEB13] M. Talaty, A. Esquenazi, and J. E. Briceño: "Differentiating Ability in Users of the ReWalk\texttrademark˜Powered Exoskeleton". *2013 IEEE 13th International Conference on Rehabilitation Robotics (ICORR)*, 1–5, 2013.

[TLCL+11] C. Tudor-Locke, S. M. Camhi, C. Leonardi, W. D. Johnson, P. T. Katzmarzyk, C. P. Earnest, and T. S. Church: "Patterns of adult stepping cadence in the 2005-2006 NHANES". *Preventive Medicine*, 53(3):178–181, 2011.

[TLWRP02] C. Tudor-Locke, J. E. Williams, J. P. Reis, and D. Pluto: "Utility of pedometers for assessing physical activity: Convergent validity". *Sports Medicine*, 32(12):795–808, 2002.

[TM01] A. Tilli and M. Montanari: "A Low-Noise Estimator of Angular Speed and Acceleration from Shaft Encoder Measurements". *Automatika (Zagreb)*, 42(3), 2001.

[TVG18] A. Taherifar, G. Vossoughi, and A. S. Ghafari: "Assistive-compliant control of wearable robots for partially disabled individuals". *Control Engineering Practice*, 74(February):177–190, 2018.

[UD21] T. K. Uchida and S. L. Delp: *Biomechanics of movement: the science of sports, robotics, and rehabilitation.* Mit Press, 2021.

[Uhl94] J. K. Uhlmann: *Simultaneous map building and localization for real time applications.* Tech. rep., Technical report, University of Oxford, 1994. Transfer thesis, 1994.

[Van84] G. N. Vanderplaats: *Numerical optimization techniques for engineering design: with applications.* New York : McGraw-Hil, 1984.

[VASB+13] B. Vanderborght, A. Albu-Schaeffer, A. Bicchi, E. Burdet, D. G. Caldwell, R. Carloni, M. Catalano, O. Eiberger, W. Friedl, G. Ganesh, M. Garabini, M. Grebenstein, G. Grioli, S. Haddadin, H. Hoppner, A. Jafari, M. Laffranchi, D. Lefeber, F. Petit, S. Stramigioli, N. Tsagarakis, M. V. Damme, R. V. Ham, L. C. Visser, and S. Wolf: "Variable impedance actuators: A review". *Robotics and Autonomous Systems*, 61(12):1601–1614, 2013.

[VKH+07] J. F. Veneman, R. Kruidhof, E. E. Hekman, R. Ekkelenkamp, E. H. Van Asseldonk, and H. Van Der Kooij: "Design and evaluation of the LOPES exoskeleton robot for interactive gait rehabilitation". *IEEE Transactions on Neural Systems and Rehabilitation Engineering*, 15(3), 2007.

[Vøl97] N. K. Vøllestad: "Measurement of human muscle fatigue". *Journal of neuroscience methods*, 74(2):219–227, 1997.

[VRV+22] V. S. Varma, R. Y. Rao, P. R. Vundavilli, M. K. Pandit, and P. R. Budarapu: "A Machine Learning-Based Approach for the Design of Lower Limb Exoskeleton". *International Journal of Computational Methods*, 19(8):1–22, 2022.

[WDBM97] A. S. Wexler, J. Ding, and S. A. Binder-Macleod: "A mathematical model that predicts skeletal muscle force". *IEEE transactions on biomedical engineering*, 44(5):337–348, 1997.

[Win09] D. A. Winter: *Biomechanics and Motor Control of Human Movement: Fourth Edition.* John Wiley & Sons, 2009.

[WQW+17] J.-J. Wan, Z. Qin, P.-Y. Wang, Y. Sun, and X. Liu: "Muscle fatigue: general understanding and treatment". *Experimental & molecular medicine*, 49(10):e384, 2017.

[WSP19] R. L. Whittaker, M. W. Sonne, and J. R. Potvin: "Ratings of perceived fatigue predict fatigue induced declines in muscle

strength during tasks with different distributions of effort and recovery". *Journal of Electromyography and Kinesiology*, 47:88–95, 2019.

[WV00] E. A. Wan and R. Van Der Merwe: "The unscented Kalman filter for nonlinear estimation". *Adaptive Systems for Signal Processing, Communications, and Control Symposium 2000. AS-SPCC. The IEEE 2000*, 153–158. Ieee, 2000.

[WV02] A. Wolfram and M. Vogt: "Zeitdiskrete Filteralgorithmen zur Erzeugung zeitlicher Ableitungen (Discrete-Time Filter Algorithms for the Computation of Time-Derivatives)". *at - Automatisierungstechnik*, 50(7):346–353, 2002.

[WWM+14] S. Wang, L. Wang, C. Meijneke, E. Van Asseldonk, T. Hoellinger, G. Cheron, Y. Ivanenko, V. La Scaleia, F. Sylos-Labini, M. Molinari, F. Tamburella, I. Pisotta, F. Thorsteinsson, M. Ilzkovitz, J. Gancet, Y. Nevatia, R. Hauffe, F. Zanow, and H. Van Der Kooij: "Design and Control of the MINDWALKER Exoskeleton". *IEEE Transactions on Neural Systems and Rehabilitation Engineering*, 23(2):277–286, 2014.

[XAG+21] M. Xiloyannis, R. Alicea, A.-M. Georgarakis, F. L. Haufe, P. Wolf, L. Masia, and R. Riener: "Soft Robotic Suits: State of the Art, Core Technologies, and Open Challenges". *IEEE Transactions on Robotics*, 1–20, 2021.

[XL08] T. Xia and L. A. F. Law: "A theoretical approach for modeling peripheral muscle fatigue and recovery". *Journal of biomechanics*, 41(14):3046–3052, 2008.

[XQ13] K. Xu and D. Qiu: "Experimental design verification of a compliant shoulder exoskeleton". *2013 IEEE International Conference on Robotics and Automation*, 3894–3901. IEEE, 2013.

[YF17] A. J. Young and D. P. Ferris: "State of the art and future directions for lower limb robotic exoskeletons". *IEEE Transactions on Neural Systems and Rehabilitation Engineering*, 25(2):171–182, 2017.

[YGZG17] Z. Yang, W. Gu, J. Zhang, and L. Gui: *Force Control Theory and Method of Human Load Carrying Exoskeleton Suit*. Springer, 2017.

[ZKF+20] Y. Zimmermann, E. B. Kucuktabak, F. Farshidian, R. Riener, and M. Hutter: "Towards dynamic transparency: Robust interaction force tracking using multi-sensory control on an arm exoskeleton". *IEEE International Conference on Intelligent Robots and Systems*, 7417–7424, 2020.

[ZWCZ22] Y. Zhu, Q. Wu, B. Chen, and Z. Zhao: "Design and Voluntary Control of Variable Stiffness Exoskeleton Based on sEMG Driven Model". *IEEE Robotics and Automation Letters*, 7(2):5787–5794, 2022.

[ZWZ+12] G. Zeilig, H. Weingarden, M. Zwecker, I. Dudkiewicz, A. Bloch, and A. Esquenazi: "Safety and tolerance of the ReWalk exoskeleton suit for ambulation by people with complete spinal cord injury: A pilot study". *The journal of spinal cord medicine*, 35(2):96–101, 2012.

[ZZL+16] C. Zhang, X. Zang, Z. Leng, H. Yu, and Y. Z. Jie Zhao: "Human machine force interaction design and control for the HIT load-carrying exoskeleton". *Rehabilitation and Assistive Robotics*, 8(4):1687814016645068, 2016.